

LAMINAR AND TURBULENT BOUNDARY LAYER  
SEPARATION CONTROL OF  
MAKO SHARK SKIN

by

FARHANA AFROZ

AMY W. LANG, COMMITTEE CHAIR

MUHAMMAD ALI ROB SHARIF

JAMES P. HUBNER

MARK E. BARKEY

PHILIP J. MOTTA

A DISSERTATION

Submitted in partial fulfillment of the requirements  
for the degree of Doctor of Philosophy  
in the Department of Aerospace Engineering and Mechanics  
in the Graduate School of  
The University of Alabama

TUSCALOOSA, ALABAMA

2014



## ABSTRACT

The Shortfin Mako shark (*Isurus oxyrinchus*) is one of the fastest swimmers in nature. They have an incredible turning agility and are estimated to achieve speeds as high as ten body lengths per second. Shark skin is known to contain flexible denticles or scales, capable of being actuated by the flow whereby a unique boundary layer control (BLC) method could reduce drag. It is hypothesized that shark scales bristle when the flow is reversed, and this bristling may serve to control flow separation by (1) inhibiting the localized flow reversal near the wall and (2) inducing mixing within the boundary layer by cavities formed between the scales that increases the momentum of the flow near the wall. To test this hypothesis, samples of Mako shark skin have been studied under various amounts of adverse pressure gradient (APG). These samples were collected from the flank region of a Shortfin Mako shark where the scales have the greatest potential for separation control due to the highest bristling angles. An easy technique for inducing boundary layer separation has been developed where an APG can be generated and varied using a rotating cylinder. Both the experimental and numerical studies showed that the amount of APG can be varied as a function of cylinder rotation speed or cylinder gap height for a wide range of Reynolds numbers. This method of generating an APG is used effectively for inducing both laminar and turbulent boundary layer separation over a flat plate. Laminar and turbulent boundary layer separation studies conducted over a smooth plate have been compared with the same setup repeated over shark skin. The time-averaged DPIV results showed that shark scale bristling controlled both laminar and turbulent boundary layer separation to a measurable extent. It shows that the shark scales cause an early transition to turbulence and reduce the degree of laminar separation. For turbulent separation, reverse flow near the wall and inside the boundary layer is hypothesized to bristle the shark scales thereby preventing the reverse flow from reaching higher magnitudes that leads to global flow separation.

## DEDICATION

This dissertation is dedicated to my loving parents, my beloved husband, Mohammad Asadul Hoque and my only son, Ruwaifi Hoque.

## LIST OF ABBREVIATIONS AND SYMBOLS

$a$	Cylinder radius, m
APG	Adverse Pressure Gradient
$C_D$	Drag coefficient
$C_f = \frac{\tau_w}{\frac{1}{2}\rho U^2}$	Skin friction
$\overline{C_f}$	Mean skin friction
$C'_p$	Canonical pressure
$\overline{C_p}$	Mean pressure coefficient
$\widehat{C_p}$	Pressure gradient along wall which is non-dimensionalized by multiplying with cylinder diameter
$\underline{C_p}$	Pressure gradient along shark body non-dimensionalized by multiplying with shark body width
$C_L$	Lift coefficient
$D$	Diameter of cylinder, m
$G$	Gap between the cylinder bottom and the flat plate, m
$h$	LSB height, mm
$H = h/D$	Dimensionless separation bubble height
LSB	Laminar Separation Bubble
$L = l/D$	Dimensionless separation bubble length
$l = X_R - X_S$	LSB Length, mm
$L$	X location of initial measurement window from leading edge of plate, mm

$L_T$	X location of turbulent tripped position, mm
$R = X_R/D$	Dimensionless distance of the reattachment point from the inlet
$Re_D$	Reynolds number based on cylinder diameter
$Re_x$	Reynolds number base on distance from leading edge
$S = s/D$	Dimensionless distance of the separation point from the inlet
$t$	Non-dimensional flow time
$T$	Transition point
$U_e$	x-velocity along the flat plate, m/s
$U$	Free stream velocity, m/s
$u$	x-velocity
$v$	y-velocity
$VR = \frac{\Omega D}{2U}$	Velocity Ratio
$X_C$	x-distance from inlet boundary to cylinder center, m
$X_O$	x-distance from cylinder center to outlet boundary, m
$X_R$	Reattachment point, mm
$X_S$	Separation point, mm
$Y_F$	Gap between cylinder and top boundary, m

$\gamma$	Separation Angle
$\delta$	Boundary Layer Thickness
$\lambda$	Laminar flow parameter
$\theta$	Momentum thickness
$\chi$	Backflow Coefficient, %
$\rho$	Density, kg/m <sup>3</sup>
$\mu$	Dynamic viscosity, kg/ms
$\nu$	Kinematic Viscosity
$\Omega$	Angular velocity of cylinder rotation
$\vec{\omega} = \frac{\partial v}{\partial x} - \frac{\partial u}{\partial y}$	Vorticity, 1/s
$\tau_w = \mu \left. \frac{\partial u}{\partial y} \right _0$	Wall shear stress
$\delta_T = \frac{0.382x}{Re_x^{1/5}}$	Turbulent Boundary Layer Thickness

## ACKNOWLEDGEMENTS

All praise goes to the ALMIGHTY who has given me the opportunity and strength to finally achieve this milestone after overcoming all the hurdles and challenges that I had faced during the last four years. On this glorious occasion, I would like to take the opportunity to thank everyone who has directly or indirectly helped me completing this dissertation research.

I am most indebted to Dr. Amy Lang, the chairman of this dissertation committee, for guiding me throughout my graduate studies and sharing her expertise in every aspects of this research. I would also like to thank all of my committee members, Dr. Muhammad Ali Rob Sharif, Mark E.Barkey James P. Hubner, Philip J. Motta. I am very thankful for the assistance and support of my lab mates: Emily Jones, Michael Bradshaw, Jennifer Wheelus. I would like to acknowledge the helping aid from the engineering machine shop for constructing the experimental setup. I would also like to thank the Department of Aerospace Engineering and Mechanics Department for providing me the opportunity to pursue my PhD degree. I greatly appreciate the financial support of National Science Foundation and Alabama EPSCoR fellowship program.

This research would not have been possible without the support of my friends in Tuscaloosa. Specially, I would like to acknowledge the support of my dearest parents, Dr. Md. Abdur Rahman Howlader and Mrs. Ummey Habiba, who did not hesitate to travel more than twelve thousand miles to accompany me during the crucial stages of my graduate studies and whenever I needed their support. I am also grateful to my husband and my two younger brothers for the endless mental support and inspiration. Last but not the least, I was always encouraged seeing the smiling face of my 3 year old son.

## CONTENTS

ABSTRACT.....	ii
DEDICATION .....	iii
LIST OF ABBREVIATIONS AND SYMBOLS.....	iv
ACKNOWLEDGEMENTS.....	vii
LIST OF TABLES.....	xii
LIST OF FIGURES.....	xiii
CHAPTER ONE: INTRODUCTION.....	1
CHAPTER TWO: USING A ROTATING CYLINDER TO INDUCE A LAMINAR SEPARATION BUBBLE OVER A FLAT PLATE.....	4
2.1 Introduction .....	5
2.2 Inviscid Theoretical Model .....	10
2.3 Experimental Procedure.....	13
2.3.1 Description of Experimental Setup.....	13
2.3.2 Data Acquisition and Analysis Technique.....	15
2.3.3 Uncertainty Analysis and Error Calculation .....	16
2.4 Results and Discussion .....	17
2.4.1 Laminar Base Flow.....	17
2.4.2 Vorticity Field in Flat Plate Boundary Layer.....	19
2.4.3 Structure of the Laminar Separation Bubble.....	21
2.4.4 Mean and R.M.S Velocity Profiles: Separation and Reattachment Points.....	23

2.4.5 Laminar Separation Bubble.....	26
2.4.5.1 Variation of Bubble Size with Change of Velocity Ratio.....	26
2.4.5.2 Variation of Bubble Size with Change of Cylinder Position.....	26
2.5 Conclusions.....	29
References.....	30
CHAPTER THREE: NUMERICAL STUDY OF GENERATING ADVERSE PRESSURE GRADIENT OVER A FLAT PLATE USING A ROTATING CYLINDER.....	34
3.1 Introduction.....	36
3.2 Problem Description.....	42
3.3 Numerical Procedure.....	44
3.3.1. Governing equations.....	44
3.3.2. Boundary Conditions.....	45
3.3.3. Computational Details.....	45
3.3.4. Numerical Model Validation.....	48
3.4 Results and Discussions.....	49
3.4.1. Time-averaged Flow Feature.....	52
3.4.1.1. Effect of Cylinder Rotational Speed on Adverse Pressure Gradient.....	53
3.4.1.2. Effect of Cylinder Wall Gap on Adverse Pressure Gradient.....	55
3.4.2. Comparison of Separation Bubble for High Re with Experimental Results....	60
3.4.3. Vortex Dynamics and Wake Evolution.....	61
3.4.4. The lift and Drag Coefficients.....	65
3.5 Conclusions.....	66
References.....	67

CHAPTER FOUR: EXPERIMENTAL STUDY OF TURBULENT BOUNDARY LAYER SEPARATION OVER A FLAT PLATE INDUCED BY A ROTATING CYLINDER.....	70
4.1 Introduction.....	71
4.2 Theoretical Inviscid Model of Turbulent Separation .....	75
4.3 Experimental Setup and Procedure .....	78
4.3.1 Description of Experimental Setup.....	78
4.3.2 Data Acquisition and Analysis Technique.....	80
4.4 Results and Discussion .....	81
4.4.1 Turbulent Base Flow.....	81
4.4.2 Vorticity Field in Flat Plate Boundary Layer.....	82
4.4.3 Using cylinder rotation speed and location for generating various amount of APG.....	85
4.4.4 Instantaneous TBL separation.....	91
4.4.5 Turbulent Intensities and Reynolds Stress.....	92
4.4.6 Time-averaged Velocity profiles.....	95
4.4.7 Skin Friction Coefficient.....	96
4.5 Conclusions .....	96
References .....	97
CHAPTER FIVE: EXPERIMENTAL STUDY OF LAMINAR AND TURBULENT BOUNDARY LAYER SEPARATION CONTROL OF SHARK SKIN .....	100
5.1 Introduction.....	101
5.2 Experimental Procedure.....	106
5.2.1 Experimental setup.....	106
5.2.2 Data Acquisition and Analysis Technique.....	108

5.3 Results and Discussion.....	110
5.3.1 Base Flow.....	111
5.3.2 Pressure Gradient along Shark Body .....	113
5.3.3 Laminar Separation Control.....	114
5.3.3.1 Time-averaged Velocity Field.....	114
5.3.3.2 Time-averaged Vorticity Field.....	117
5.3.3.3 Reynolds Stress.....	118
5.3.3.4 Instantaneous Velocity Field.....	119
5.3.4 Turbulent Separation Control.....	125
5.3.3.1 Contour of Backflow Coefficient.....	125
5.3.3.2 Time-averaged Vorticity Field.....	127
5.3.3.3 Time-averaged Velocity Field.....	129
5.3.3.4 Instantaneous Velocity Field.....	130
5.3.3.5 Time-averaged Reynolds Stress Profiles.....	132
5.4 Summary.....	133
5.5 Ecological Ramifications of Separation Control.....	133
5.6 Conclusions.....	136
References .....	137
 CHAPTER SIX: CONCLUSION.....	 142
References .....	143

## LIST OF TABLES

2.1	Laminar Separation Bubble Characteristics for Different Velocity Ratio at $Re_x = 1.3 \times 10^5$ and $G/D = 0.75$ .....	23
2.2	Laminar Separation Bubble Characteristics for Different $G/D$ at $Re_x = 1.3 \times 10^5$ and $VR = 1.208$ .....	23
2.3	Comparison of experimental separation point with predicted value.....	23
4.1	Comparison of experimentally measured separation point with predicted values.....	85
5.1	Comparison of LSB over flat plate and shark skin under different amount of APG.....	110
5.2	Comparison of Turbulent Separation over flat plate and shark skin under different amount of APG.....	120

## LIST OF FIGURES

2.1	(a) Counter-rotating cylinder pair for reverse doublet like configuration (b) theoretical streamlines for counter-rotating cylinder (c) Schematic diagram of experimental set-up for generating APG using a rotating cylinder and location of measurement window.....	9
2.2	Theoretical gradient of pressure coefficient for reverse-doublet like cylinder rotation along the wall for (a) different Velocity Ratio, VR at $\frac{G}{D} = 0.75$ , (b) at different $\frac{G}{D}$ for a fixed VR = 1.208.....	11
2.3	Thwaites method of predicting Laminar Separation point (a) for different VR, (b) for different G/D.....	13
2.4	Flat plate model and cylinder in water tunnel.....	14
2.5	(a) Velocity Contour for laminar base flow, and (b) Comparison of experimental laminar stream wise mean velocity profile for U = 0.132 m/s.....	17
2.6	Instantaneous Streak flow visualization for different Velocity Ratio (VR).....	18
2.7	Time-averaged vorticity Contours varying Velocity Ratio for a fixed cylinder location G/D = 0.75 at Reynolds Number, $Re_x = 1.3 \times 10^5$ .....	20
2.8	Structure of LSB for Reynolds Number, $Re_x = 1.3 \times 10^5$ due to APG generated for VR = 1.208, G/D = 0.75.....	21
2.9	PIV measurements of LSB for VR = 1.208, G/D = 0.75 and Reynolds Number, $Re_x = 1.3 \times 10^5$ , (a) Streamlines for mean flow, (b) Normalized Reynolds Stress distribution( $-\frac{\overline{u'v'}}{U^2}$ ).....	22
2.10	(a) Mean Dividing Streamline, (b) Mean velocity profile at separated, transition and reattachment region for VR = 1.208 G/D = 0.75 and Reynolds Number, $Re_x = 1.3 \times 10^5$ .....	23
2.11	Time-averaged Velocity field variation of Velocity Ratio for a fixed cylinder location G/D = 0.75 at Reynolds Number, $Re_x = 1.3 \times 10^5$ .....	27

2.12	Time-averaged velocity Contours with variation of cylinder location for fixed $VR = 1.208$ at Reynolds Number, $Re_x = 1.3 \times 10^5$ .....	28
3.1	(a) Schematic diagram of flow configuration, (b) Sample mesh, and (c) zoomed view of mesh around the cylinder.....	43
3.2	Grid and time step independence study $Re = 1000$ , $G/D = 0.5$ , $VR = 0.5$ .....	44
3.3	Comparison of the time evolution of the lift and drag coefficients between the present computation and that in for flow past a rotating circular cylinder without any wall in the vicinity at $Re = 200$ and $VR = 0.5$ and $1.0$ .....	45
3.4	Instantaneous streamlines around the rotating cylinder at different times for $Re=200$ ; present study (left), semianalytical method (center), and experimental flow visualization (right).....	47
3.5	Instantaneous streamlines around the rotating cylinder at different times for $Re=1,000$ and $VR = 0.5$ ; present study (left) and semianalytical method (right).....	49
3.6	Comparison of velocity profiles, along the horizontal line through the center of the cylinder, with the semi analytical results of Badr and Dennis for $VR = 0.5$ .....	50
3.7	Time-averaged stream wise velocity contours along with few selected streamlines for different cylinder speed ( $VR$ ) at $Re = 1,000$ and $G/D = 0.75$ .....	51
3.8	Time-averaged stream wise velocity contours along with few selected streamlines for different cylinder speed ( $G/D$ ) at $Re = 200$ and $G/D = 0.25$ .....	53
3.9	(a) Distribution of the mean pressure coefficient ( $C_p$ ) along the wall and (b) distribution of the mean skin friction coefficient ( $C_f$ ) on the wall for different cylinder speed for $Re = 1,000$ and $G/D = 0.75$ .....	54
3.10	(a) Distribution of the mean pressure coefficient ( $C_p$ ) along the wall and (b) distribution of the mean skin friction coefficient ( $C_f$ ) on the wall for different cylinder speed for $Re = 200$ and $G/D = 0.25$ .....	55
3.11	Time-averaged stream wise velocity contours along with few selected streamlines for different cylinder gap ( $G/D$ ) at $Re = 1000$ , $VR = 0.5$ .....	56
3.12	Time-averaged stream wise velocity contours along with few selected streamlines for different cylinder gap ( $G/D$ ) at $Re = 200$ , $VR = 0.25$ .....	57

3.13	(a) Profiles of mean pressure coefficient on the wall ( $C_p$ ), (b) Profiles of mean coefficient of friction( $C_f$ ) for different cylinder gap ( $G/D$ ) at $Re = 1000$ , $VR = 0.5$ .....	58
3.14	(a) Profiles of mean pressure coefficient on the wall ( $C_p$ ), (b) Profiles of mean coefficient of friction( $C_f$ ) for different cylinder gap ( $G/D$ ) at $Re = 200$ , $VR = 0.25$ .....	58
3.15	Separation Bubble properties as function of (a) Cylinder rotation speed ( $VR$ ), (b) Gap Ratio, $G/D$ for $Re = 200$ .....	59
3.16	Separation Bubble properties as function of (a) Cylinder rotation speed ( $VR$ ), (b) Gap Ratio, $G/D$ for $Re = 1,000$ .....	60
3.17	Time-averaged (a) mean streamline $C_f$ along wall (b). stream wise velocity contours along with few selected streamlines for different cylinder gap ( $G/D$ ) at $Re = 6,700$ , $G = 0.75$ , $VR = 0.8$ .....	61
3.18	Vorticity contours around the rotating cylinder near a flat wall during one cycle of vortex shedding for $Re = 200$ , $G/D = 0.75$ and $VR = 1$ .....	62
3.19	Vorticity contours around the rotating cylinder near a flat wall during one cycle of vortex shedding for $Re = 1,000$ , $G/D = 0.5$ and $VR = 0.5$ .....	63
3.20	Time history of lift and drag coefficient for $Re = 1,000$ and $G/D = 0.75$ .....	64
3.21	Elimination of vortex shedding indicated by steady (time independent) variation of drag and lift coefficients for various combinations of $Re$ , $G/D$ , and $VR$ . .....	65
4.1	Using rotative cylinder to generate APG to induce separate turbulent boundary layer over flat plate .....	74
4.2	Theoretical pressure coefficient gradient for reverse-doublet like cylinder rotation along the wall for (a) different Velocity Ratio, $VR$ at $\frac{G}{D} = 0.75$ , (b) at different $\frac{G}{D}$ for a fixed $VR = 2.13$ .....	76
4.3	Stratford's criteria for predicting turbulent separation point for (a) different Velocity Ratio, $VR$ at $\frac{G}{D} = 0.75$ , (b) at different $\frac{G}{D}$ for a fixed $VR = 2.13$ .....	77
4.4	Experimental Setup in water tunnel (a) Different Components of Experimental setup (b) scematic diagram of arrangment of components .....	79

4.5	Experimental and theoretical turbulent velocity profile without any pressure gradient for $Re_x = 2.5 \times 10^5$ .....	82
4.6	Streak flow visualization for different VR .....	83
4.7	Time-averaged Vorticity Contour for different VR .....	84
4.8	Backflow Coefficient contour for Different VR .....	86
4.9	Time-averaged velocity contour for different VR for a fixed gap ratio ( $G/D = 0.75$ ) .....	87
4.10	TBL separation for VR = 2.13 and $G/D = 0.5$ (a) Backflow coefficient contour (b) Mean velocity field .....	90
4.11	Instantaneous TBL separation and corresponding vorticity contour for VR = 2.66 at an interval of 0.2s.....	91
4.12	Contours of turbulence intensities (a) longitudinal component ( $\frac{(u'^2)^{\frac{1}{2}}}{U}$ ), (b) wall normal component ( $\frac{(v'^2)^{\frac{1}{2}}}{U}$ ), (c) Reynolds shear stress ( $-\frac{(u'v')^{\frac{1}{2}}}{U^2}$ ) .....	93
4.13	Time-resolved velocity profiles for various VR(a) $u/U$ profile, (b) Reynolds shear stress ( $-\frac{(u'v')^{\frac{1}{2}}}{U^2}$ ) .....	94
4.14	Skin friction coefficient ( $C_f$ ) profile near wall for different VR, (a) VR = 2.13, (b) VR = 2.66 (c) mean velocity distribution .....	95
5.1	Outline of measured scale bristling angles at various locations on the Mako Shark .....	103
5.2	(a) SEM of non-bristled Mako scales. (b) SEM of bristled Mako scales and the formation of cavities between the scales .....	104
5.3	Use of a rotating cylinder to induce flow separation over a flat plate and shark skin at downstream position of cylinder. ....	107
5.4	Flat plate with affixed shark skin samples, frozen .....	108

5.5	Theretical gradient of pressure coefficient for cylinder gap height, $G/D = 0.75$ and different cylinder rotation speeds (VR), (a) $Re_x \approx 1.3 \times 10^5$ ,(b) $Re_x \approx 2.5 \times 10^5$ and, (c) $Re_x \approx 3 \times 10^5$ .....	111
5.6	Experimental and theoretical velocity profile, (a) laminar flow ( $Re_x \approx 1.3 \times 10^5$ ), (b) turbulent flow ( $Re_x \approx 2.5 \times 10^5$ ) .....	112
5.7	(a) Numerical model of shark body, (b) pressure gradient along shark body, (c) pressure gradient along the flank region of shark body .....	114
5.8	Time-averaged velocity contour for laminar flow separation at $Re_x \approx 1.3 \times 10^5$ and at different amount of APG (a) VR =1.208. (b) VR = 1.409 .....	115
5.9	Comparison of separation point, transition point and LSB size between flat plate and shark skin at $Re_x \approx 1.3 \times 10^5$ and at different amount of APG (a) VR = 1.208, (b) VR = 1.409 .....	116
5.10	Time-averaged vorticity under same amount of APG, $Re_x \approx 1.3 \times 10^5$ at VR = 1.409 .....	117
5.11	Time-averaged normalized Reynolds Stress ( $-\frac{\overline{uv}}{U^2}$ ) field for laminar flow at $Re_x \approx 1.3 \times 10^5$ and at different amount of APG, (a) VR = 1.208, (b) VR = 1.409 .....	118
5.12	Instantaneous velocity history flat plate Vs shark skin for VR = 1.208 at $y = 2$ mm and at different X-positions (a) $x = 45$ mm, (b) $x = 70$ mm .....	119
5.13	Instantaneous Flow Field for laminar flow under same amount of APG at VR = 1.409 at upstream location of separation .....	120
5.14	Instantaneous Flow Field for laminar flow under same amount of APG at VR = 1.409 inside the separation region .....	121
5.15	Instantaneous velocity history flat plate Vs shark skin for VR = 1.409 at $y = 2$ mm and at different X-positions (a) $x = 45$ mm, (b) $x = 70$ mm .....	123
5.16	Contour of backflow coefficient of laminar flow under at $Re_x \approx 1.3 \times 10^5$ and at different amount of APG, (a), VR = 1.209, (b) VR = 1.409 .....	124
5.17	Contour of backflow coefficient of turbulent flow under at different amount of APG, (a) $Re_x \approx 2.5 \times 10^5$ , VR = 2.13, (b) $Re_x \approx 2.5 \times 10^5$ , VR = 2.66, and (c) $Re_x \approx 3.0 \times 10^5$ , VR = 3.10 .....	125

5.18	Contour of backflow coefficient of turbulent flow under at $Re_x \approx 3.0 \times 10^5$ and at $VR = 2.65$ , (a) smooth plate, (b) shark skin .....	126
5.19	Time-averaged vorticity field under at different amount of APG, (a) $Re_x \approx 2.5 \times 10^5$ , $VR = 2.13$ , (b) $Re_x \approx 2.5 \times 10^5$ , $VR = 2.66$ .....	128
5.20	Time-averaged velocity ( $u/U$ ) contour for turbulent flow separation at different amount of APG (a) $Re_x \approx 2.5 \times 10^5$ , $VR = 2.13$ , (b) $Re_x \approx 2.5 \times 10^5$ , $VR = 2.66$ , and (c) $Re_x \approx 3.0 \times 10^5$ , $VR = 3.10$ .....	129
5.21	Figure 5.20: Instantaneous velocity history inside the turbulent separation region flat plate Vs shark skin for $y = 2$ mm and $x = 45$ mm, (a) $Re_x \approx 2.5 \times 10^5$ , $VR = 2.13$ (b) $Re_x \approx 2.5 \times 10^5$ , $VR = 2.66$ (c) $Re_x \approx 3.0 \times 10^5$ , $VR = 3.10$ .....	131
5.22	Figure 5.21: Time-averaged Reynolds stress profile under at different amount of APG, (a) $Re_x \approx 2.5 \times 10^5$ , $VR = 2.13$ , (b) $Re_x \approx 2.5 \times 10^5$ , $VR = 2.66$ , and (c) $Re_x \approx 3.0 \times 10^5$ , $VR = 3.10$ .....	132

# CHAPTER ONE

## INTRODUCTION

Boundary layer separation occurs on a surface when the flow experiences an adverse pressure gradient, whereby a portion of the boundary layer closest to the wall reverses in response to the lower pressure felt upstream. Such separation results in a considerable limitation to the operating characteristics of airfoils, propellers, and turbines. Delay in the onset of separation can delay the onset of stall of an airfoil, decrease pressure drag, improve the performance of a propeller, and increase the fuel efficiency of vehicles and aircraft. Because of the practical importance of drag reduction, research should be undertaken that involves both understanding the separated flow as well as reducing or delaying boundary layer separation.

Drag reduction inspired by nature has special interest in the field of fluid mechanics. The Shortfin Mako (*Isurus oxyrinchus*) is one of the fastest swimming marine creatures. It is known to have highly flexible scales on certain parts of its body where high adverse pressure gradients are expected to occur due to its body shape. It is hypothesized by Lang [1] that shark scales bristle when encountering a reversing flow and thereby disrupt the process leading to flow separation. The present study focuses on testing shark skin under various amounts of APG to explore the mechanism of controlling flow separation. For this purpose, a reliable system is needed to generate various strengths of APG that induce laminar and turbulent flow separation.

Unfortunately, insufficient research has been conducted to develop a system which can generate different magnitudes of APG. To study the physics of boundary layer separation, more research needs to be performed for developing simple systems which will allow imposing a wide variation of APG. One widely used system of imposing an APG over a plane surface involves a convex wall above a flat plate; as a result flow separation occurs due to area change inducing flow

deceleration above the surface [2-4]. The magnitude of the APG is varied by varying the top wall contour. In this method, after a short region of favorable pressure gradient in the area contraction, an adverse pressure gradient induces the separation bubble. But this technique requires an additional arrangement, such as wall suction, to prevent boundary layer separation over high curvature walls, thus higher APG. Suction/blowing is another means of generating APG over a flat plate, but there are several difficulties associated with the development of such a system [5, 6]. This type of APG generation system consists of a duct work that encloses the path of the extracted air flow and an in-line duct fan that drives the flow. But the suction and blowing panels in the ceiling of the test section act as a large cavity, which create massive separation entering the system. Additional arrangements are needed to reduce this cavity-like flow and to mitigate external noise in the system due to the suction/blowing fan. Section 2.1 includes further discussion about generating APG using suction-blowing method.

This work involved the design and construction of an innovative and easy technique to generate various magnitudes of APG using a rotating cylinder and is presented in chapters two, three and four. In chapter two, an experimental study of inducing laminar separation bubble over flat plate using a rotating cylinder is presented. A theoretical inviscid model for different combinations of rotation speed and cylinder location is also discussed to quantify the amount of theoretical APG along the flat plate. This theoretical model is also used to predict the separation point and then compared with the experimentally measured separation point.

Then in chapter three, the pressure gradient along the flat plate is numerically obtained for different combinations of rotation speed and cylinder gap height. This numerical study also addresses the mechanism of laminar boundary layer separation over a flat plate. The corresponding wake dynamics was investigated for a wide range of Reynolds numbers.

An experimental study of turbulent separation under various magnitudes of APG is presented in chapter four. The rotating cylinder system is used for inducing turbulent separation over a flat plate. The study reveals the impact of rotation speed and cylinder gap ratio on the nature and extent of the separation region. The theoretical model is also used to predict the various strengths of APG along the flat wall and to theoretically calculate the separation point.

Using the same rotating cylinder technique, shark skin samples with the most flexible scales collected from the flank region, were tested under various amounts of APG. In chapter five, these shark skin results are compared with the smooth flat plate data under the same operating conditions to explore the flow separation control mechanism of shark skin.

## CHAPTER TWO

### USING A ROTATING CYLINDER TO INDUCE A LAMINAR SEPARATION BUBBLE OVER A FLAT PLATE\*

Farhana Afroz, Amy Lang, Emily Jones

Department of Aerospace Engineering and Mechanics, University of Alabama

#### Abstract

An easy technique for inducing a laminar separation bubble (LSB) over a flat plate was investigated, whereby an adverse pressure gradient (APG) was generated and varied by the presence of a rotating cylinder. A theoretical model to predict the pressure variation induced on the plate consists of an inviscid flow over a reverse doublet-like configuration of two counter rotating cylinders. This model quantified the pressure distribution with changes of cylinder speed and location. The dimensionless cylinder rotation rate (VR) and gap to diameter ratio  $\frac{G}{D}$  were chosen as the two main ways of varying the strength of the APG, which affects the nature and extent of the LSB. An experimental parametric study, using time-resolved digital particle image velocimetry (TR-DPIV), was then conducted in a water tunnel. Results showed good agreement with the theoretical prediction of the point of flow separation, and the variation in height (h), length (l), and the separation point (S) of the LSB was documented due to the variation in the APG.

Keywords: Rotating Cylinder, Adverse Pressure Gradient, Laminar Separation Bubble, Particle Image Velocimetry.

\**European Journal of Mechanics-B/Fluids (Under Review)*

## 2.1 Introduction

When a laminar boundary layer is subject to an adverse pressure gradient, the boundary layer separates from the surface, the detached flow transitions, and the separated shear layer re-attaches to form a laminar separation bubble (LSB). There are only a few established techniques that are used to generate an adverse pressure gradient (APG) to induce the formation of a laminar separation bubble (LSB) over a flat wall. One common method is to impose an APG over a plane surface by changing the contour of the top wall [1, 2]. A pressure-induced laminar separation bubble can also be formed by positioning a displacement body in the test section above the flat plate [3, 4]. The amount of APG is then controlled by varying the angle of the displacement body. In this method, after a short region of the favorable pressure gradient, an adverse pressure gradient induces the separation bubble. Both these techniques require an additional arrangement, such as wall suction, to prevent boundary layer separation over the displacement body itself for high curvatures and thus high APG. Also, any variation in the strength of the pressure gradient typically requires a change in geometry.

Apart from these two methods, numerical studies [5-9] have used suction/blowing as a means of generating an adverse pressure gradient over a flat plate. In one study [5], steady and local uniform blowing was imposed in a cross flow through a thin slot. As the local blowing amplitude was increased, the boundary layer flow over the flat plate started to separate at a critical blowing rate. The simulation results also showed that the time-averaged separation bubble length increased approximately linearly with the local blowing amplitude. However, no suction mechanism was incorporated in this study. Another study [6] utilized suction mechanism along with blowing, where a flat plate with an elliptical nose was placed in a channel, subject to the uniform incoming free stream at the channel inlet. An adverse pressure gradient was induced at the top of the flat plate, due to the steady blowing and suction through the upper wall of

channel leading to the separation of the laminar boundary layer on the plate [6]. A numerical investigation [7] presented that the suction-blowing velocity profile along the top boundary created a strong adverse-to-favorable pressure gradient, while a separated turbulent boundary layer resulted at the bottom wall. The upper boundary layer in this technique needs to be far away from the separation bubble, so that the turbulence intensities, as well as the vorticity, are sufficiently small near the upper boundary. Using suction/blowing to induce flow separation was studied experimentally [8, 9]. However, these studies addressed several difficulties associated with the development of the system. To allow for the net mass flow conservation, the additional system requires a site at which the extracted airflow can be reinserted into the wind tunnel. Thus, this separation system consists of a duct that encloses the path of the extracted airflow, in the form of an in-line duct fan that drives the flow. However, the suction and blowing panels in the ceiling of the test section act as a large cavity, which creates a massive separation when entering the system. A honeycomb flow straightener may help with uniform flows entering and exiting the ducting and should reduce the cavity-like flow oscillations. Moreover, if the fan within the separation system is in close proximity to the test section and does not cover the cross-sectional area within the duct, this could lead to major three-dimensional variations at the suction and blowing boundaries. External noise can be also introduced into the tunnel because of the in-line duct fan, even though this can be mitigated by placing acoustic foam in the lower section of the duct.

The structure of the LSB was first documented by Jones [10] and was continued by Gault [11]. However, the most noteworthy study in terms of understanding bubble structure was performed by Gaster [4], since this was the first study that systematically explored the stability characteristics associated with the transition taking place in a separation bubble. The bubble constitutes, at the same time, laminar separation, transition to turbulence and aspects of both the attached as well as free shear layer. Besides understanding the structure and dynamics of a

separation bubble, recent studies have focused more on minimizing flow separation. However, inadequate research has been conducted with regard to developing techniques that are less complex and which can induce a wide variation of conditions for inducing flow separation on a flat surface.

Several numerical and experimental investigations have been conducted to study the change in flow structure when a stationary or rotating cylinder is placed in the vicinity of a plane wall. For instance, a strong suppression of vortex shedding was found to occur when a cylinder was placed near a stationary plane wall at a gap to diameter ratio ( $G/D$ ) of 0.3 [12]. It was also found that the lift force experienced by the cylinder was directed away from the wall, although the Strouhal number ( $St$ ) did not exhibit much variance when the cylinder moved closer to  $G/D=0.3$ . A visualization study around a non-rotating circular cylinder placed near a flat wall was also conducted for various Reynolds numbers, based on the diameter of the cylinder being between 1200 and 4960 [13]. In this experimental study, particle image velocimetry and hot-film anemometry techniques were employed to observe the effect created by changing the gap between the cylinder and the wall (the  $G/D$  varied from 0 to 2). The flow was categorized into four distinct regions, with a delineation between regions of around  $G/D = 0.5$ . Below this value, the boundary layer flow on the wall separates, due to the presence of the cylinder, and the vortex shedding rate is also affected, while for  $G/D > 0.5$  (values used for this study fall into this category), the vortex shedding is regular and any flow separation induced on the wall is minimal. Other experimental and numerical studies also documented that a variation in the gap ratio affected the force experienced by the cylinder, as well as the frequency of the vortex shedding [14-17]. The interaction of a vortex wake with a boundary layer flow has also been studied, and showed that strong vortex interaction near the wall initiated regions of flow separation [18, 19].

Previous research has also documented the flow associated with a rotating circular cylinder located above a plane wall in a free stream flow. The wake behind the cylinder and the

flow along the wall depends mainly on four parameters: the boundary layer thickness on the flat wall, the rotation rate of the cylinder, the Reynolds number, and the gap ratio ( $G/D$ ). An interesting phenomenon reported in a numerical study of two-dimensional flow showed that, for moderate Reynolds numbers ( $20 < Re_D < 750$ ), a reverse rotation aiding the flow in the gap between the wall and the cylinder of the cylinder can completely suppress vortex shedding [20]. Cheng and Luo [21] simulated a two-dimensional incompressible flow around a rotating circular cylinder near a plane wall at  $Re_D = 200$ . The effects of the cylinder rotation rate and the cylinder gap to diameter ratio on the hydrodynamic forces and the frequency of vortex shedding from the cylinder were quantified. Two critical limiting values of gap were identified, namely a lower limiting value and an upper limiting value, both of which depended on the cylinder rotation rate. The flow was steady below the lower limiting gap value, and the gap flow was either completely suppressed or was extremely weak. In addition, the separation of the boundary layer occurred both upstream and downstream of the cylinder, and there was no vortex shedding in the wake, in that the wake flow was stable. The higher the value of the cylinder rotation speed, the higher the lower limiting gap value at which vortex shedding was suppressed. There was no boundary layer separation on the plane wall for the gaps that were larger than the upper limiting value, either upstream or downstream of the cylinder. A regular vortex sheet was observed for these gap flows. However, the upper limiting value of the gap depended weakly on the cylinder rotation rate.

In the present study, a simple technique for generating a wide variation in the APG over a flat plate was developed via the use of a cylinder rotating in a counterclockwise direction (see fig. 2.1), such that the cylinder rotation induced a high speed flow through the gap, which resulted in boundary layer separation being induced on the wall just downstream of the cylinder location. A theoretical model for a rotating cylinder near a flat plate predicted the strength of the APG along the plate, based on the rotation rate and the cylinder location. This experimental

setup allows for more versatility in controlling the strength of the APG, when compared to methods that were used previously. Based on previous work performed by others, only the intermediate gap to cylinder diameter ratios ( $G/D$ ) were selected for the present experimental study, as small  $G/D$ s suppress the gap flow and make it extremely weak. The effect of the cylinder location,  $G/D$ , and the dimensionless velocity ratio,  $VR$ , on the global properties of the LSB, such as height, length, and separation point, are documented in this study.

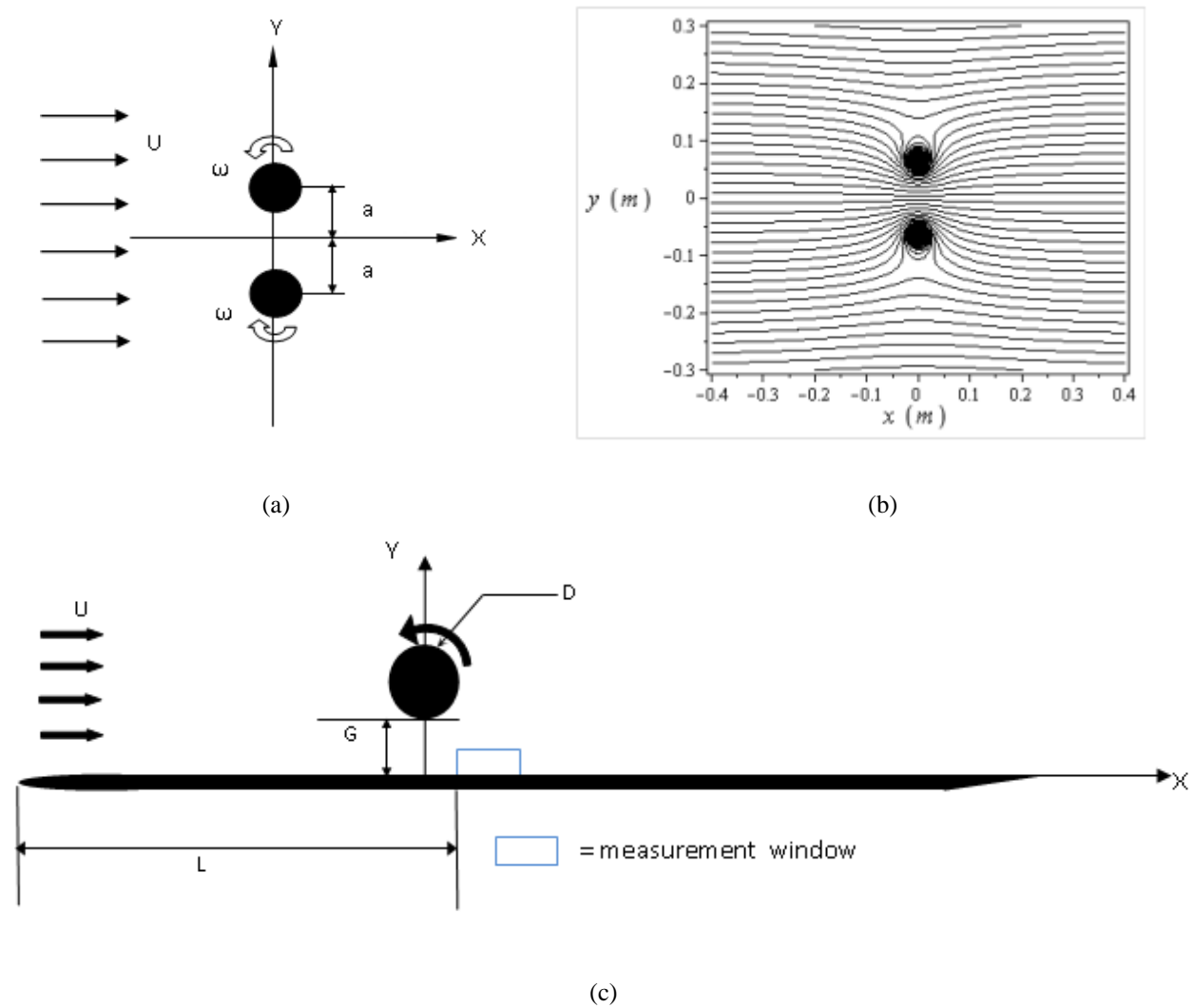


Figure 2.1: (a) Counter-rotating cylinder pair for reverse doublet-like configuration, (b) theoretical streamlines for counter-rotating cylinders, and (c), the schematic diagram of an experimental set-up for generating APG using a rotating cylinder and a location of measurement window

## 2.2 Theoretical Inviscid Model

In the present study, an inviscid theoretical model for the flow surrounding a rotating cylinder located near a wall has been assembled by the superposition of a free stream flow, doublet and vortices. The method of images produced a symmetrical line between two identical rotating cylinders to form the plane wall.

The streamfunction for a single rotating cylinder is

$$\psi_1 = Uy \left[ 1 + \left( \frac{R}{x+iy} \right)^2 \right] + \mu_v \ln (x + iy) \quad (i)$$

where the strength of the vortex is defined as

$$\mu_v = \frac{\Gamma}{2\pi} = \frac{2\pi R^2 \Omega}{2\pi} \quad (ii)$$

The streamfunction equation for the reverse doublet-like configuration of a counter rotating cylinder pair is

$$\psi = Uy + \frac{\pi NR^2}{60} \ln \left( \frac{x^2+(y+a)^2}{x^2+(y-a)^2} \right) + UR^2 y \left( \frac{1}{x^2+(y-a)^2} + \frac{1}{x^2+(y+a)^2} \right) \quad (iii)$$

Figures 2.1 (a) and (b) present the reverse doublet-like configuration and calculated streamlines.

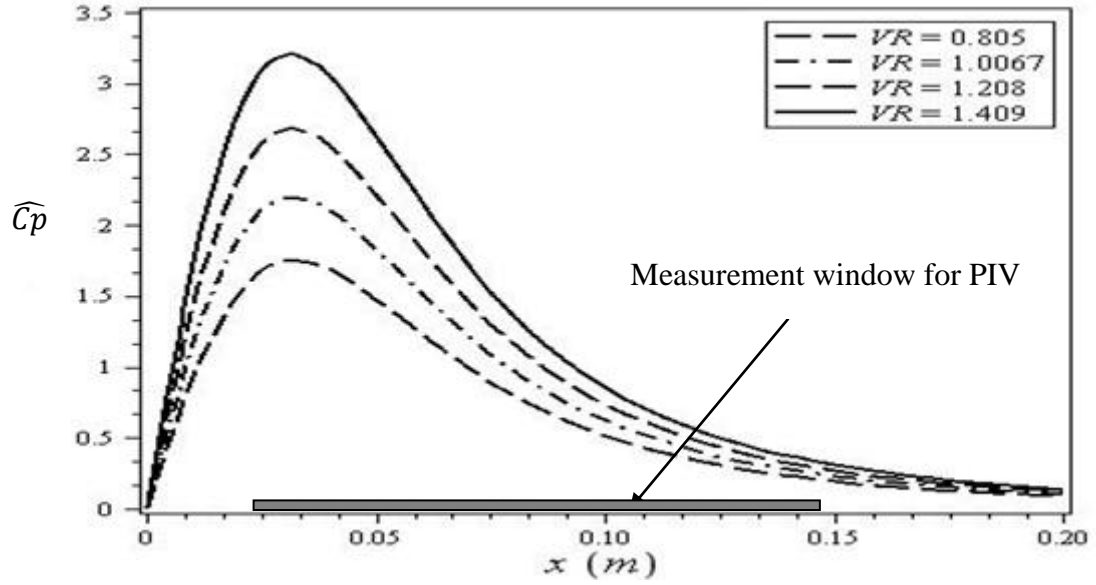
The purpose of the theoretical study is to compute the pressure gradient along the wall for different cylinder rotation speeds and gap to diameter ratios, thereby predicting the zone in which the boundary layer separation begins. A plot of the streamlines shows that, as the cylinder rotates, it compresses the gap flow. The same type of compression of streamlines in the region between two counter-rotating reverse doublet-like cylinders was also observed in the research work conducted by Andre et al. [22].

The x-component of velocity along the wall,  $U_e$ , is

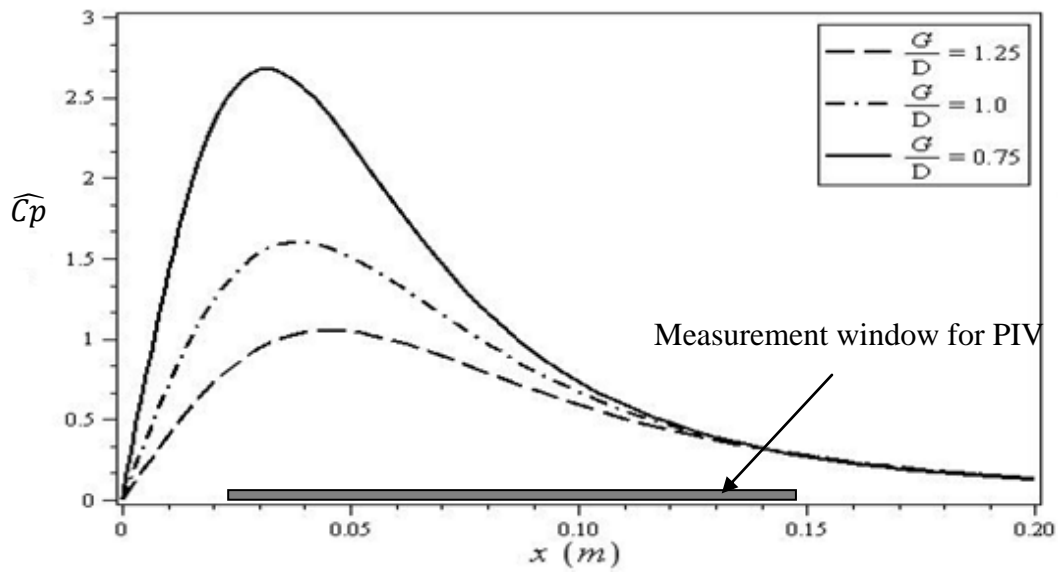
$$U_e = \frac{\partial \psi}{\partial x} (\text{for } y=0) \quad (iv)$$

This velocity can be used to calculate the pressure coefficient, as follows:

$$C_p = \frac{P-P_\infty}{\frac{1}{2}\rho U^2} = 1 - \frac{U_e^2}{U^2} \quad (v)$$



(a)



(b)

Figure 2.2: Theoretical gradient of the pressure coefficient for the reverse doublet-like cylinder rotation along the wall for (a) different velocity ratio, VR at  $\frac{G}{D} = 0.75$ , and (b), at different  $\frac{G}{D}$  for a fixed VR = 1.208.

The tunnel flow speed for all experiments,  $U = 0.132$  m/s, was also used for the theoretical calculations. The corresponding gradient in the pressure coefficient along the wall is presented

for several velocity ratios,  $VR = \frac{\Omega D}{2U}$ , and gap ratios  $G/D$  (Fig 2.2). Pressure gradient variation up to only  $x = 0.2$  m has been presented, as beyond this point the pressure gradient does not vary significantly. Fig. 2.2(a) shows that, as the dimensionless cylinder rotation rate ( $VR$ ) increases, the peak value of the APG increases as well. As predicted, these data also reveal that, at higher rotation speeds ( $VR$ ), the strength of the adverse pressure gradient also increases. This calculation predicts the earlier separation, and thus a larger separation bubble, as the cylinder speed is increased. The measurement location was chosen based on these calculations (highlighted from 0.025 m to 0.145 m in fig. 2.2(a)).

In addition, the strength of the adverse pressure gradient increases and the peak location also moves upstream as the cylinder moves closer to the wall (fig. 2.2(b)). The peak in the APG only varies dramatically as the  $G/D$  decreases from 0.75 to 0.5.

The measurement window covers the area starting from the zone where the boundary layer is subjected to an extreme APG, and includes the zone where the pressure gradient decreases and begins to gradually decline. It was thus predicted that the laminar separation bubble would form and reattach within the measurement region. The same parametric values for cylinder speed ( $VR$ ) and gap to diameter ratio ( $G/D$ ) were used in both the theoretical and experimental cases in order to allow for direct comparison.

Fig. 2.3 presents the prediction of the separation point using the Thwaites method [23].

With these criteria, the separation point is defined when

$$\lambda = -0.09 = \frac{\theta^2}{\nu} \frac{dU_e}{dx} \quad (\text{vi})$$

$$\frac{\theta^2}{\nu} = \frac{0.45}{U_e^6} \int_0^x U_e^5 dx \quad (\text{vii})$$

Here, the value of  $U_e$  along the flat plate is calculated from a theoretical inviscid model.

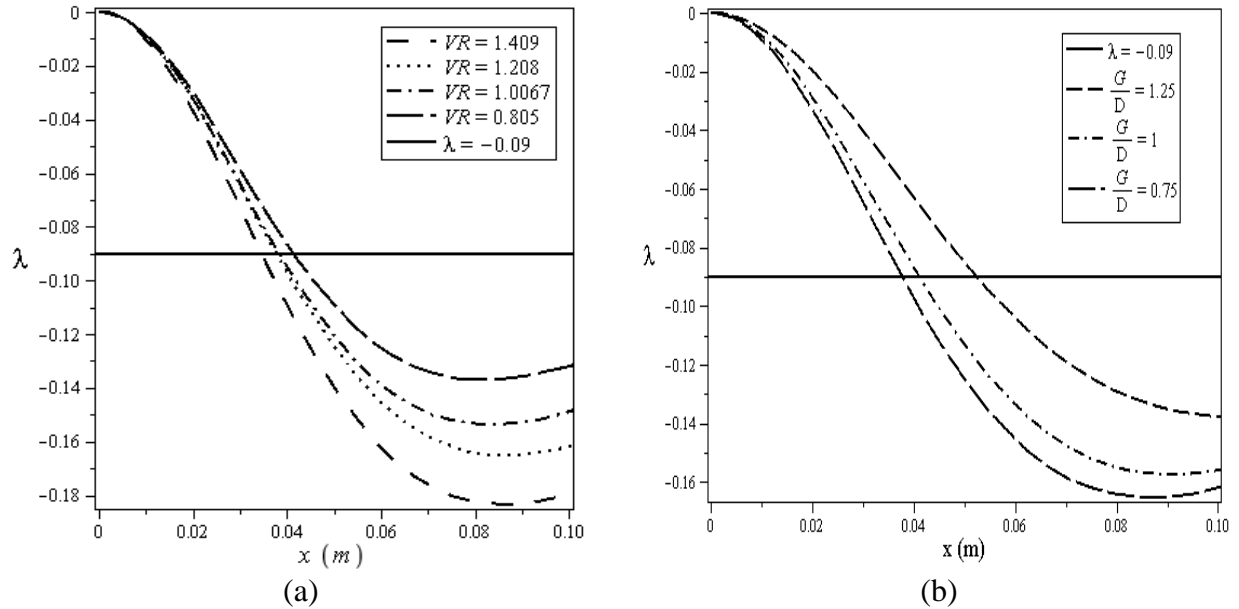


Figure 2.3: Thwaites method of predicting the laminar separation point, (a) for different VR and (b) for different G/D

## 2.3 Experimental Procedure

### 2.3.1 Description of the Experimental Setup

The experimental studies were conducted in a water tunnel facility manufactured by the Rolling Hills Research Corporation at the University of Alabama. It has a test section size of 38 cm wide by 76 cm tall by 275 cm long. A flat plate model, made out of black Plexiglas, with dimensions of 45.72 cm long and 60.96 cm wide, was mounted vertically in the test section. Attached to the front of this plate is a leading plate with an elliptical nose (91.44 cm in length), followed by the flat plate model and a trailing edge flap for controlling the oncoming streamline. This flap is adjusted based on flow speed and blockage, in order to prevent the formation of a separation bubble at the nose of the flat plate. The axes used to display the orientation of the model are labeled as follows:  $x$  is the positive downstream flow direction and  $y$  is positive upwards from the plate (fig. 2.4). A PVC cylinder (diameter of 5.1 cm) was placed at a distance of  $L = 101.6$  cm ( $\approx 20D$ ) downstream from the leading edge of the flat plate, and spanned the

total width (45.72 cm) of the plate (fig. 2.1(C)). Flow visualization was conducted for a constant water tunnel speed of  $U = 0.132$  m/s, giving a Reynolds number for the boundary layer based on the distance from the leading edge of  $Re_x \approx 1.3 \times 10^5$ . The parametric study was carried out by varying both the cylinder rotation speed ( $\Omega$ ) and the cylinder location ( $G/D$ ), in order to vary the strength of the APG. A time-resolved DPIV system was used to document the corresponding size and location of the induced LSB.

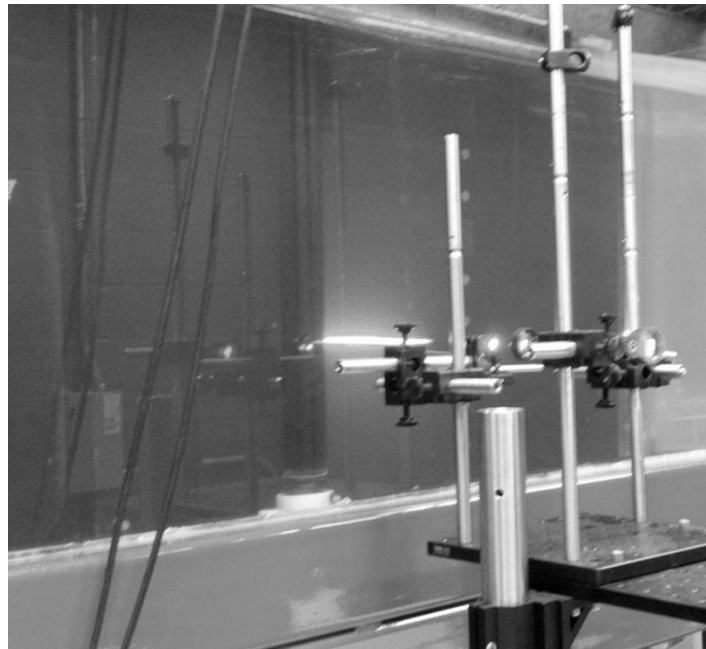


Figure 2.4: Flat plate model and cylinder in the water tunnel

### 2.3.2 Data Acquisition and Analysis Technique

In order to carry out the digital particle image velocimetry (DPIV) measurements, the flow was seeded with  $14 \mu\text{m}$  silver-coated hollow glass spheres and then illuminated by a laser sheet generated by a Quantronix Falcon 20 m J Nd: YLF laser. The maximum power output of this laser is 20 watts, and it has a beam wavelength of 532 nm, 7 to 30 amps current output range, and .1 to 1.0 kHz frequency range. Pulsing of the laser and image acquisition was

synchronized with the help of LabVIEW software. Insight3G DPIV software was used to analyze the acquired images and to obtain the velocity vector field. The size of each measurement window for image acquisition was 6.5 cm x 3.25 cm, and images were captured by a Basler A504K high-speed camera at a rate of 500 frames per second. In many cases, two consecutive measurement windows (1 cm overlap) were needed to capture the entire laminar separation bubble.

A total of 3600 images (7.2 sec) for each rotation speed were captured at 1280 x 512 pixels, and were then analyzed to obtain an average flow field. The images were captured 2.5 cm downstream of the cylinder center, as this is the region in which the boundary layer starts to separate from the flat plate. The measurement area was divided into small interrogation windows. The interrogation window size started at 32x16 pixels and was reduced to 24 x 12 pixels in order to ensure good data resolution. A minimum intensity image generator was used to determine the background noise common to all of the images, and this noise was then subtracted from each image in order to increase the accuracy of the vector calculations. During processing, Insight 3G software utilized a Recursive NyQuist Grid, an FFT Correlation Engine, and a Gaussian Peak Engine, while post-processing filtering was performed to eliminate any bad vectors due to localized insufficient seeding.

### 2.3.3 Uncertainty Analysis and Error Calculation

Several sources of error exist in digital particle image velocimetry (DPIV) measurements. The error associated with the DPIV technique is difficult to compute, as it is primarily the result of insufficient data (poor seeding density or poor image quality) [24, 25]. These limitations were minimized as far as possible in the current experiment by carefully maintaining adequate seeding density. In the existing literature, an acceptable estimate of error is 5% in velocity measurements and 10% in vorticity [25, 26]. The length calibration was performed by placing a ruler within the

plane of the laser sheet and capturing an image. The pixel to distance ratio was then measured manually by calculating the pixels between two marks of one centimeter on the ruler. The microns/pixel calibration for most of the data was calculated to be 37.8. Tilting the ruler in the image is a potential source of error. Based on user experience, the maximum tilting error lies within 5 pixels resulting 1.88% error in the length scale. The camera was fixed at one location for capturing images, and the same calibration was used in every processing set. The edge of the surface often appears in the middle of a processing grid. As these grids are 16 pixels in height, error in the calculation of the edge of the surface may be as high as .32 millimeters, or 0.7% of the total height of the image. An additional source of error may occur during the procedure of data processing. For every image processed, the processing software calculates the vector and then determines whether or not the calculated value of that vector is accurate by comparing with neighboring vectors. The DPIV processing software gave an estimation of the average percentage of valid vectors in each processing window, and the lowest measurement of good vectors was approximately 97%. Hence, we get the following three types of errors—

Calibration error,  $\Delta e_1 = 1.88\%$  or 0.0188

Processing grid error,  $\Delta e_2 = 0.7\%$  or 0.007

DPIV software calculation error,  $\Delta e_3 = 3\%$  or 0.03

As per the root-sum-square (RSS) method, the overall uncertainty combining all three types of error is given by the following equation—

$$\begin{aligned}\Delta e &= \sqrt{\Delta e_1^2 + \Delta e_2^2 + \Delta e_3^2} \\ &= \sqrt{(0.0188)^2 + (0.007)^2 + (0.03)^2} = 0.036 = 3.6\%\end{aligned}$$

Hence, the overall amount of error for the velocity measurements is 3.6%, which is within the acceptable range of error (<5%) for DPIV measurements.

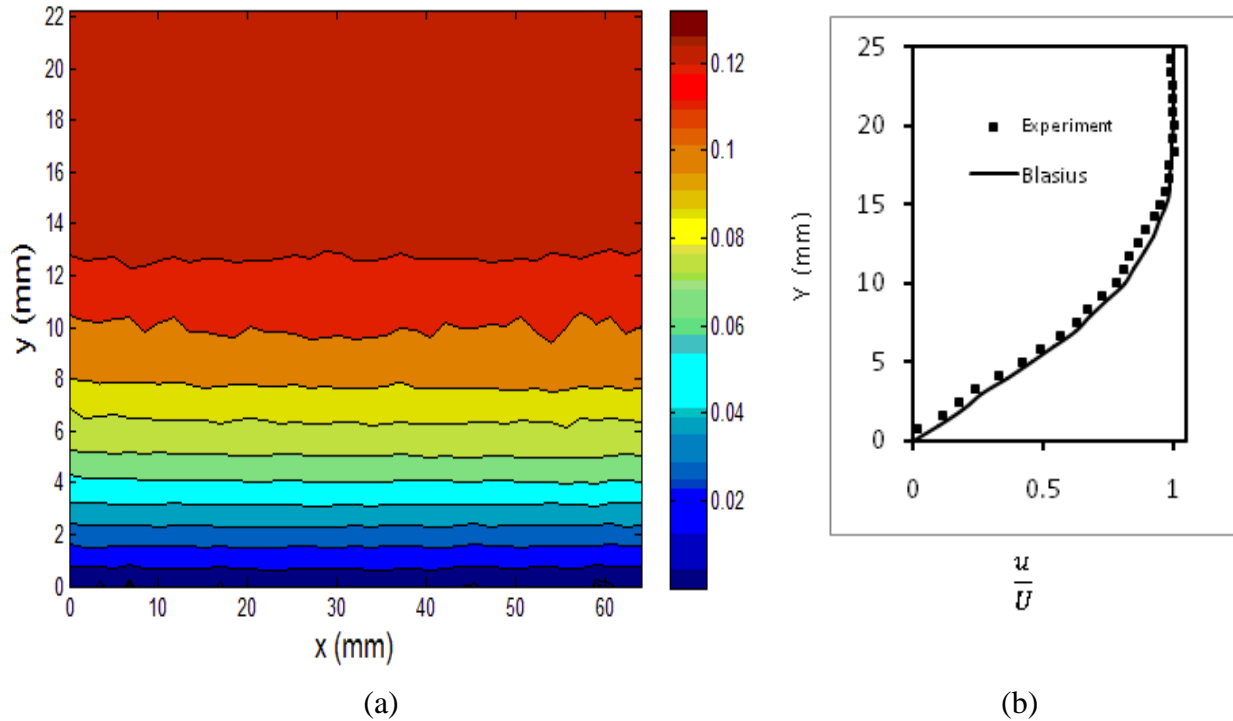
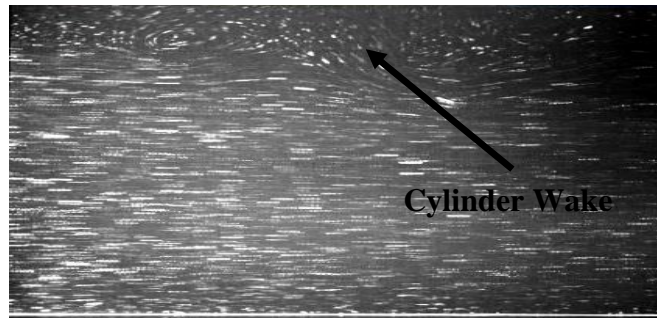
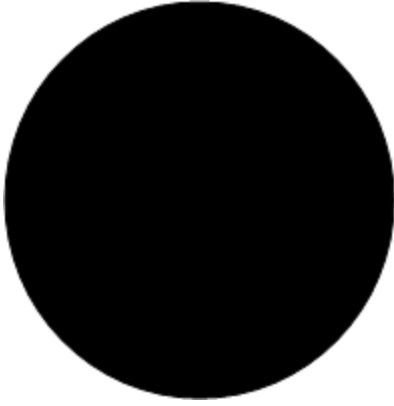


Figure 2.5 (a) Velocity contour for laminar base flow, and (b) the comparison of the experimental laminar stream-wise mean velocity profile with Blasius profile for  $U = 0.132$  m/s

## 2.4 Results and Discussion

### 2.4.1 Laminar Base Flow

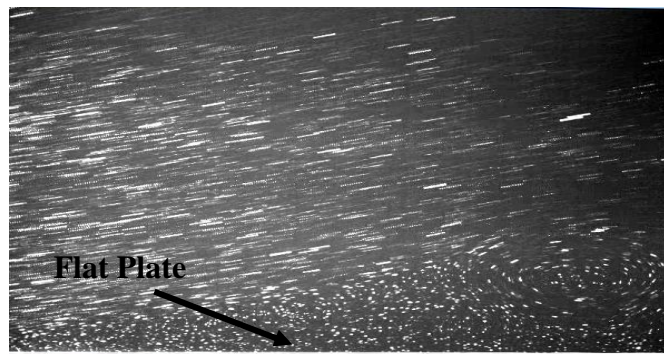
The laminar base flow was first studied in order to document the experimental flow without the presence of the cylinder. After confirming the formation of a clean laminar base flow, the flow was then subjected to an APG in order to induce a laminar separation bubble. The trailing edge flap was kept at  $15^{\circ}$  to prevent the formation of a separation bubble at the nose of the flat plate. In fig. 2.5 (b), the velocity profile for  $U = 0.132$  m/s with a Reynolds number,  $Re_x \approx 1.3 \times 10^5$ , based on the distance from the leading edge is compared with the theoretical Blasius profile. The latter was calculated using Howarth's solution of Blasius' profile with zero incidences, and is in good agreement with the experimental values [27]. The theoretical boundary layer thickness,  $\delta$ , based on Blasius' calculation, is in the region of 13.5 mm and the experimental boundary layer thickness,  $\delta$  is found to be around 13 mm (fig. 2.5(a)).



(a)  $VR = 0$



(b)  $VR = 0.805$



(c)  $VR = 1.409$

Figure 2.6: Instantaneous streak flow visualization for different velocity ratios

#### 2.4.2 The Vorticity Field in the Flat Plate Boundary Layer

The Reynolds number based on the cylinder diameter for the present study is  $Re_D = 6680$ . Therefore, the flow over the cylinder is in the sub-critical regime for Reynolds numbers between 300 and  $1.4 \times 10^5$  [28]. The boundary layer along the surface of the cylinder for this regime is laminar along the circumference until separation. The vortex shedding is regular, and the Strouhal number,  $St$ , which represents the non-dimensional vortex shedding frequency in terms of diameter ( $D$ ) and free stream velocity ( $U$ ), is constant at approximately 0.2. However, due to cylinder rotation, the unsteady wake was observed to be carried up and away from the wall for rotating cylinders; thus, it did not interfere with the flow field, as shown in the instantaneous streak flow visualization in fig. 2.6. In this preliminary flow field study, the measurement window spanned the entire gap between the cylinder and plate. For the stationary cylinder (fig. 2.6 (a)), the cylinder wake is visible outside the flat plate boundary layer. As the cylinder speed increases, the wake is found to be absent from the measurement region as a separation bubble forms on the plate.

From fig. 2.7, it can also be seen that the flow is approximately inviscid outside the boundary layer. To describe this new technique of LSB formation more precisely, consider that the rotating cylinder acts like a real vortex with a solid body rotational core (peak velocity at cylinder edge), after which the flow induced by the cylinder rotation (other than the viscous wake) acts as an irrotational vortex flow. As the cylinder speed increases, the strength of the circulation increases, which causes earlier and stronger separation of the flat plate boundary layer. For both of the cylinder rotation speeds ( $VR$ ), as seen in fig. 2.7, the separated flow forms a free shear layer outside the mean dividing streamline and contains the clockwise, negative

vorticity from the original boundary layer flow. The region between the wall and the mean dividing streamline forms counterclockwise positive vorticity. Again, no positive counterclockwise vorticity from the lower half of the cylinder wake was found to be present in the measurement region, as the rotating cylinder pulls the wake upwards and away from the wall. Thus, a stable separation bubble is formed by this new technique for the study of flow separation on a flat wall.

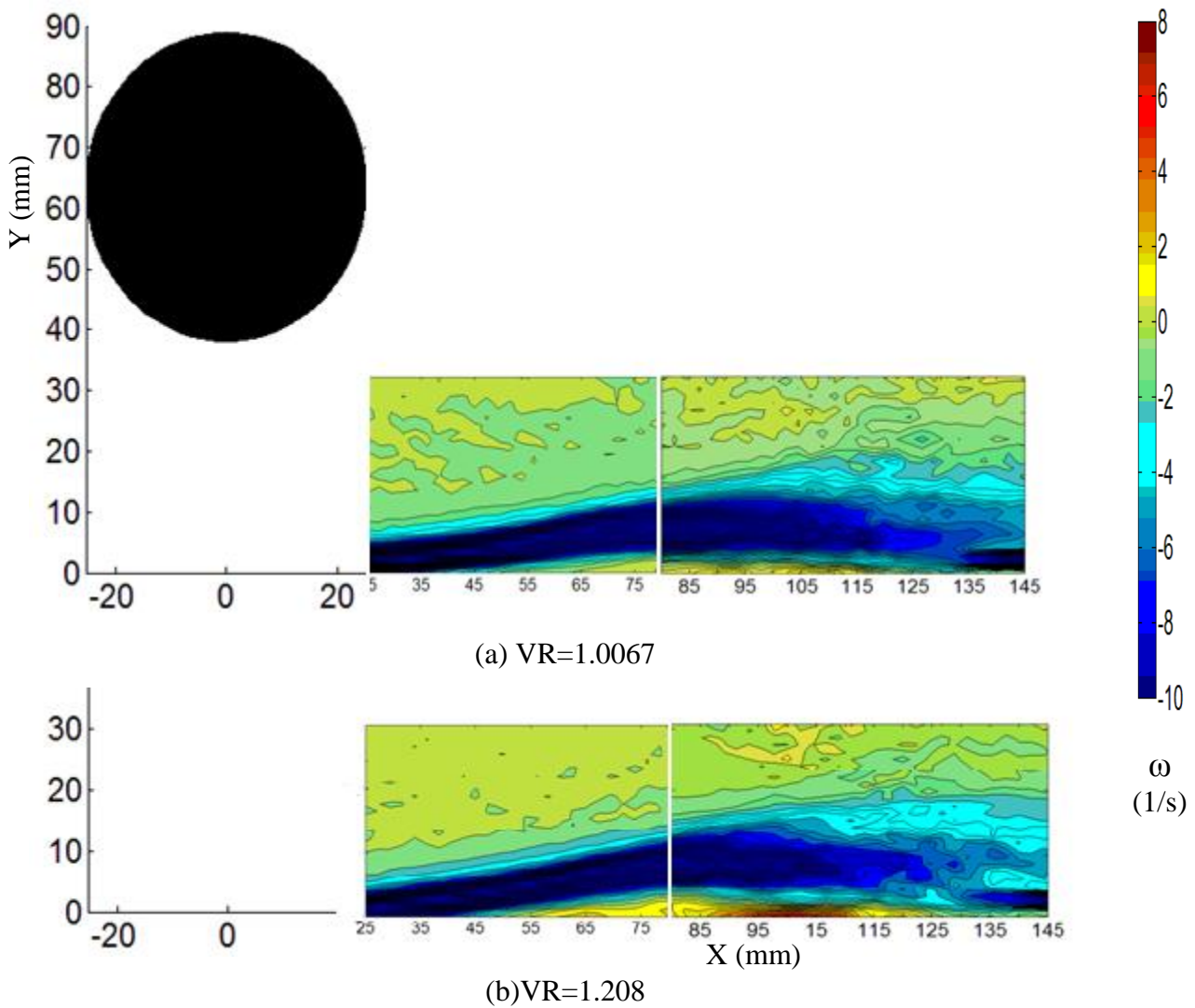


Figure 2.7: Time-averaged vorticity contours for varying velocity ratios for a fixed cylinder location  $G/D = 0.75$  at Reynolds Number,  $Re_x = 1.3 \times 10^5$

### 2.4.3 Structure of the Laminar Separation Bubble

A laminar separation bubble is formed when an attached laminar boundary layer encounters an adverse pressure gradient, leading to flow separation. O'Meara and Mueller [29] describe the typical structure of an LSB in detail and, according to their research, the separation bubble is roughly divided into two main regions by the equation for the mean dividing streamline ( $\int_{y=0}^{y^{DSL}} u(y)dy = 0$ ). The first region is the region between the mean dividing streamline and the flat surface. The mean dividing streamline is defined by the line where the net integrated mass flux is zero. A relatively slow, re-circulatory flow happens in the first region of flow within the bubble. The second region of flow is formed by the combination of a free shear layer between the outer edge of the boundary layer and the mean dividing streamline. This separated shear layer transitions and becomes unstable in this region. Turbulent mixing is responsible for high momentum transfer, which ultimately results in flow reattachment at point R.

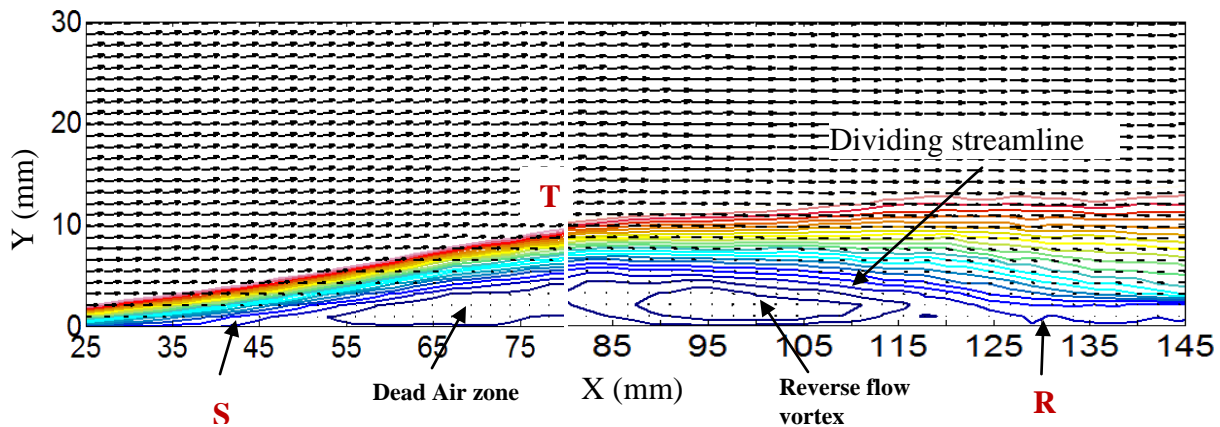


Figure 2.8: Structure of LSB for Reynolds number,  $Re_x = 1.3 \times 10^5$ , due to APG generated for  $VR = 1.208$ ,  $G/D = 0.75$

The structure of an LSB measured in this experiment, where  $VR = 1.208$  and  $G/D = 0.75$  (fig. 2.8), is in good agreement with the structure of a typical LSB as reported by others. The laminar

boundary layer departs at the separation point, S, the flow undergoes a transition (starting in the region of location T), and eventually reattaches at point R as a turbulent boundary layer. This LSB includes a dead zone of separated laminar flow, and then a reverse flow vortex in the transitional turbulent shear region. This type of LSB construction matches the DNS observation of LSB [30, 31].

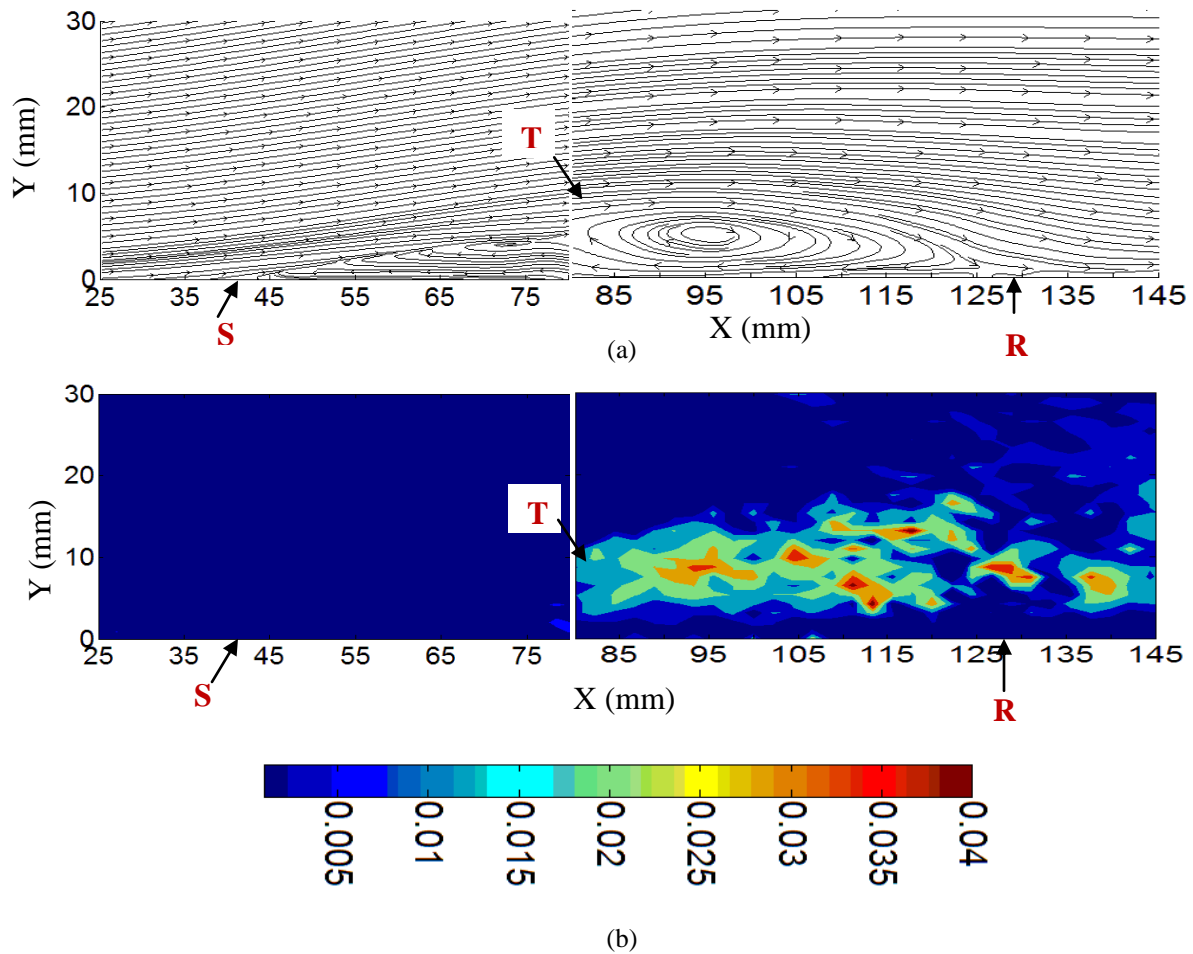


Figure 2.9: PIV measurements of LSB for  $VR = 1.208$ ,  $G/D = 0.75$  and Reynolds number,  $Re_x = 1.3 \times 10^5$ ,  
 (a) Streamlines for mean flow, (b) Normalized Reynolds stress distribution ( $-\frac{\overline{uv}}{U^2}$ )

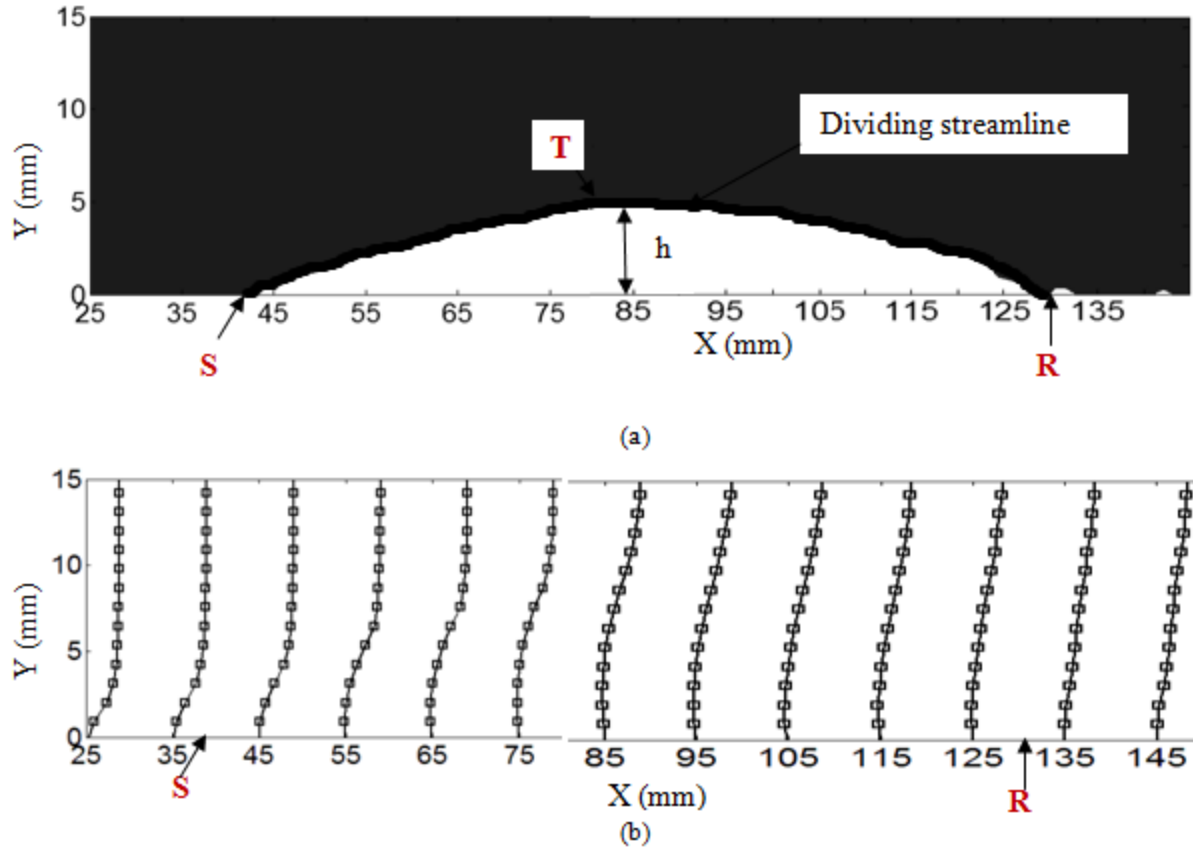


Figure 2.10: (a) Mean dividing streamline, (b) Mean velocity profile at separated, transition and reattachment region for  $VR = 1.208$   $G/D = 0.75$  and Reynolds number,  $Re_x = 1.3 \times 10^5$

#### 2.4.4 Mean and R.M.S Velocity Profiles: Separation, Transition, and Reattachment Points

Documenting mean velocity profiles, turbulence intensity, and Reynolds stress measurements within the shear layer can be an effective way of determining the locations of laminar separation, transition, and turbulent reattachment [32]. The streamlines from the mean flow in fig. 2.9(a) reveal the predicted structure of an LSB. The appearance of a separated turbulent shear region is defined as the point of transition for an LSB. Normalized Reynolds stress ( $-\frac{\overline{uv'}}{U^2}$ ) is a measurement technique for locating the turbulent transition point for a separation bubble. The transition point, T, where the normalized Reynolds stress ( $-\frac{\overline{uv'}}{U^2}$ ) is more

than 0.001, has been used as the critical value for the start of turbulent transition in separated shear layers in the existing literature [33-36], and the contour levels of Reynolds stress above 0.001 are only shown in fig. 2.9(b). It shows that the transition point from the cylinder center starts at position T ( $X = 81$  mm). This technique for identifying the transition point has been used for the LSBs documented here because of the variation of APG, and is tabulated in table 2.1.

Fig. 2.10(a) shows the LSB region bounded by the  $U = 0$  velocity line, on which the separation point, the transition point and the reattachment point are identified. The LSB reaches its maximum height ( $h$ ) at the point of transition, T, and then decreases as a result of the turbulent mixing, eventually reattaching at point, R. The variation in height concurrent with a variation in the strength of the APG is shown in table 2.1. Fig. 2.10(b) shows the profiles of the stream wise mean velocity component, which is normalized with the free stream velocity,  $U$ , when the downstream distance is within the measurement region. It gives a clear picture of what happens when a laminar boundary layer is subjected to an APG. As the velocity profile approaches the separation point, inflection caused by the APG can be observed in the velocity profiles. Beyond the dead zone, an almost constant velocity gradient is maintained.

From table 2.1, it can also be seen that, with an increase of VR, the separation point moves upstream. The height and the length of the bubble also expand with the growth of VR. The angle at which the streamlines separate from the plate, defined as the separation angle, or  $\gamma = \tan^{-1} \frac{h}{X_T - X_S}$ , has also been calculated. The separation angle increases as the cylinder rotation speed increases, and averages in the region of  $7^\circ$ .

Table 2.1: Laminar Separation Bubble Characteristics for Different Velocity Ratios at $Re_x = 1.3 \times 10^5$ and $G/D = 0.75$						
VR	$X_S$ (mm)	$X_R$ (mm)	$L = X_R - X_S$ (mm)	$X_T$ (mm)	h (mm)	$\gamma$
0.805	47	110	63	85	3.8	5.71062
1.0067	43	123	76	82	4.6	6.727082
1.208	38	131	93	81	5.8	7.682131
1.409	34	145	111	90	8	8.130342

Table 2.2: Laminar Separation Bubble Characteristics for Different G/Ds at $Re_x = 1.3 \times 10^5$ and VR = 1.208						
G/D	$X_S$ (mm)	$X_R$ (mm)	$L = X_R - X_S$	$X_T$ (mm)	h (mm)	$\gamma$
1.25	54	128	74	95	3.8	4.462
1.00	47	123	76	85	4.6	7.496079
0.75	38	131	93	81	5.8	7.682131

Table 2.3: Comparison of experimental separation points with predicted values					
VR	$X_s$ (Predicted) (mm)	$X_s$ (Exp.) (mm)	G/D	$X_s$ (Predicted) (mm)	$X_s$ (Exp) (mm)
0.805	44	47	1.25	53	54
1.0067	40	43	1.00	46	47
1.208	36	38	0.75	36	38
1.409	33.7	34			

Table 2.2 depicts the growth in the size of the LSB as cylinder moves close to the wall. The separation angle,  $\gamma$ , increases as the gap between the cylinder and the plate decreases. The separation point predicted by the Thwaites method and that measured experimentally for each case has been tabulated in table 2.3 for comparison. It shows that the Thwaites method gives good agreement, with the theory slightly underpredicting the experimental results.

## 2.4.5 Laminar Separation Bubble

### 2.4.5.1 Variation of Bubble Size with Changes of the Velocity Ratio

Fig. 2.11 and fig. 2.12 demonstrate how a variation in the cylinder rotation speed and the gap height can be used for varying strengths of APG and thus LSB size. The flow data shown in fig. 2.11 agrees with the predictions that are based on the theoretical calculations. As the rotation speed increases, the circulation induced in the inviscid flow region increases, and the laminar boundary layer starts to experience a stronger APG. As the cylinder rotates faster, the strength of the solid body rotation increases and induces greater circulatory motion. The flow in the gap experiences higher acceleration with the increase of the cylinder rotation speed and the pressure is reduced. As a result, the separation point moves upstream with the increase of the cylinder rotation speed, and the separation bubble also increases in size.

### 2.4.5.2 Variation of Bubble Size with a Change of the Cylinder Position

The theoretical calculation (fig. 2.2(b)) shows that keeping a fixed cylinder rotation rate ( $VR = 1.208$ ) while moving the cylinder closer to the wall means that the closer the cylinder the faster the flow, which causes the strength of the APG to increase. As a result, the peak APG moves upstream and increases in magnitude as the  $G/D$  decreases. The DPIV time-averaged velocity field agrees with the theoretical prediction. As the cylinder moves closer to the wall, the inner shear layer deflects away from the wall, producing a larger area of separated flow, while the separation point moves upstream (fig. 2.12). Therefore, a variety of combinations using  $G/D$  and  $VR$  to control these effects can induce different strengths of APG to form a stable laminar separation bubble on a flat plate.

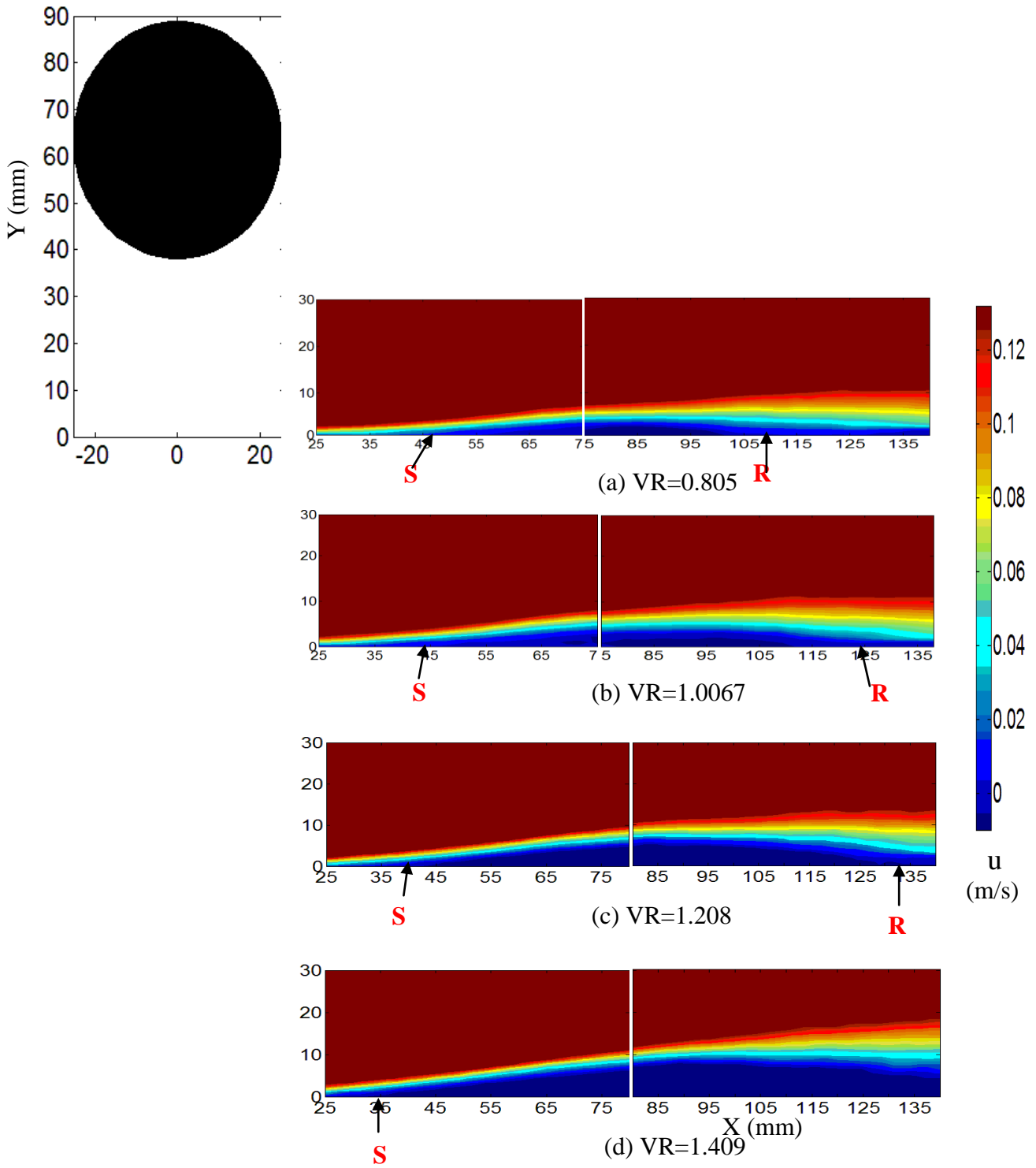


Figure 2.11: Time-averaged velocity field variation of the velocity ratio for a fixed cylinder location  $G/D = 0.75$  at Reynolds Number  $Re_x = 1.3 \times 10^5$

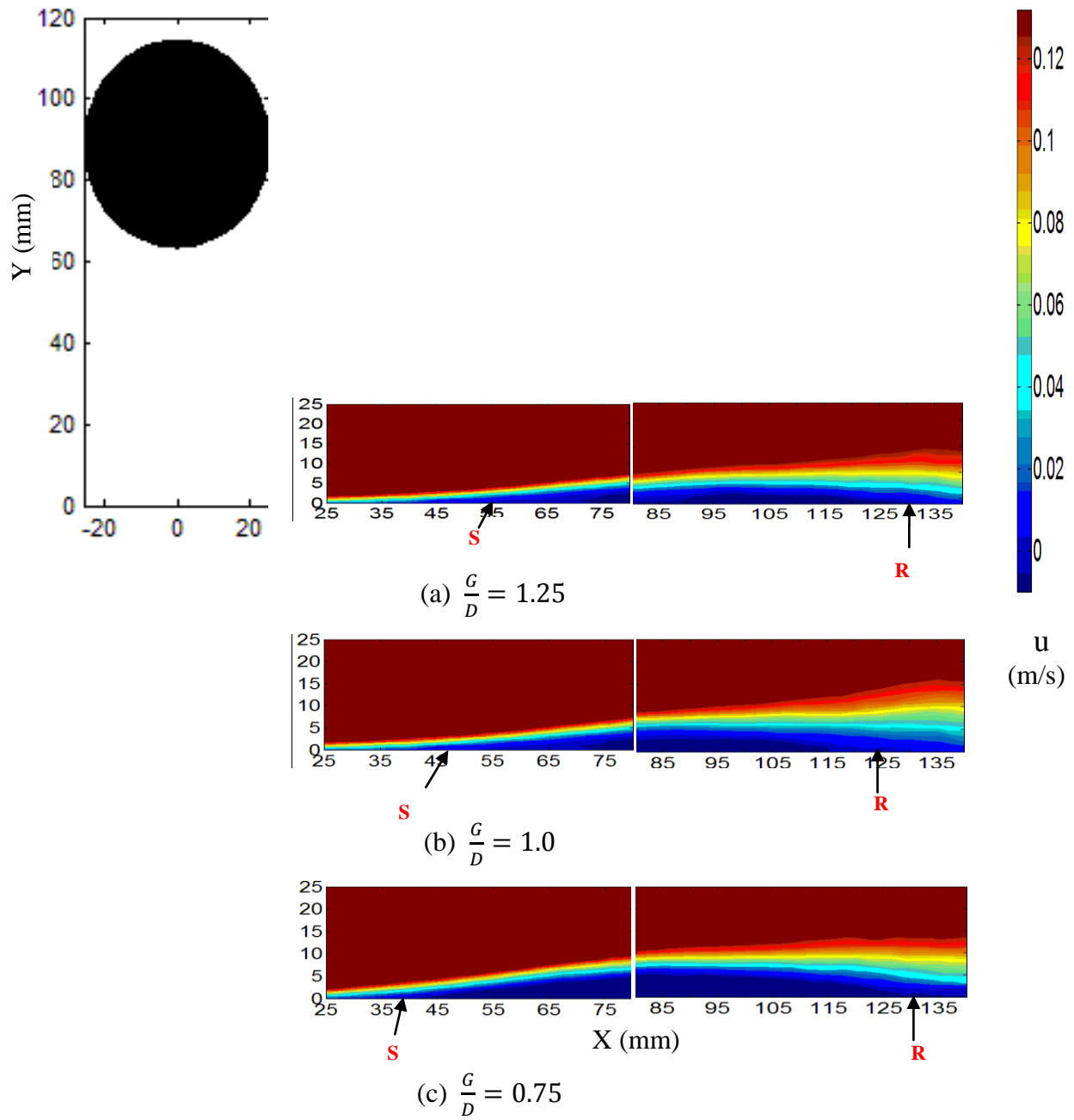


Figure 2.12: Time-averaged velocity contours with variation of cylinder location for fixed  $VR = 1.208$  at Reynolds Number  $Re_x = 1.3 \times 10^5$

## 2.5 Conclusion

The inviscid theoretical model for a cylinder rotating above a flat plate in a free stream flow predicts the strength of the induced adverse pressure gradient at the wall for various rotation speeds ( $VR$ ) and cylinder positions ( $G/D$ ). A parametric experimental study corresponding with the theoretical model conditions was performed, and gives good agreement with the theoretical predictions, including the point of separation using the Thwaites method. The time-averaged DPIV velocity field has been used for capturing the LSB under various cylinder rotation speeds and locations. It can be concluded from this study that a rotating cylinder is an effective method of generating and controlling of the strength of the APG in order to induce various sizes of laminar separation bubbles to form over a flat plate.

## Acknowledgement

Support under NSF grant 0932352 and NSF REU grant 1062611 is gratefully acknowledged. The first author, Farhana Afroz, was also supported by a scholarship through the Alabama EPSCoR Graduate Research Scholars' Program.

## References

1. Diwan, S. S., & Ramesh, O. N. (2007). Laminar separation bubbles: Dynamics and control. *Sadhana*, 32(1-2), 103-109.
2. Sohn, K. H., Shyne, R. J., & DeWitt, K. J. (1998). Experimental investigation of boundary layer behavior in a simulated low pressure turbine (Vol. 207921). *National Aeronautics and Space Administration, Lewis Research Center*.
3. Lang, M., Rist, U., & Wagner, S. (2004). Investigations on controlled transition development in a laminar separation bubble by means of LDA and PIV. *Experiments in Fluids*, 36(1), 43-52.
4. Gaster M. (1966), The structure and behavior of laminar separation bubbles. *AGARD CP* 4, pp. 813–854
5. Jiang Chen, X., Kim, K., & Sung, H. J. (2006). Effects of local blowing from a slot on a laminar boundary layer. *Fluid dynamics research*, 38(8), 539-549.
6. Marxen, B. O., Kotapati, R. B., & You, D. (2006). Evaluation of active control of a laminar separation bubble based on linear stability theory. *Center for Turbulence Research, Annual Research Briefs*.
7. Na, Y., & Moin, P. (1998). The structure of wall-pressure fluctuations in turbulent boundary layers with adverse pressure gradient and separation. *Journal of Fluid Mechanics*, 377, 347-373.
8. Griffin, J., Oyarzun, M., Cattafesta, L. N., Tu, J. H., Rowley, C. W., & Mittal, R. (2013). Control of a Canonical Separated Flow, *43rd Fluid Dynamics Conference*.
9. Rampi R. M. (2012). Design and characterization of a separation system for a flat plate model in a low-speed wind tunnel , *Undergraduate thesis, University of Florida*.
10. Jones, B. M. (1934). Stalling. *JR Aeronaut. Soc*, 38(285), 753.
11. Gault, D. E. (1957). A correlation of low-speed, airfoil-section stalling characteristics with Reynolds number and airfoil geometry. *National Advisory Committee for Aeronautics*.

12. Bearman, P. W., & Zdravkovich, M. M. (1978). Flow around a circular cylinder near a plane boundary. *Journal of Fluid Mechanics*, 89(1), 33-47.
13. Price, S. J., Sumner, D., Smith, J. G., Leong, K., & Paidoussis, M. P. (2002). Flow visualization around a circular cylinder near to a plane wall. *Journal of Fluids and Structures*, 16(2), 175-191.
14. Muraoka, K. & Tashiro, S. (1985). The effect of the wake from circular cylinder on boundary-layer transition: (The effect of gap between the cylinder and surface), *J. Japan Soc. Mech. Eng. B*, 50(460), 3152-3158 (in Japanese).
15. Taniguchi, S., & Miyakoshi, K. (1990). Fluctuating fluid forces acting on a circular cylinder and interference with a plane wall. *Experiments in Fluids*, 9(4), 197-204.
16. Lei, C., Cheng, L., & Kavanagh, K. (1999). Re-examination of the effect of a plane boundary on force and vortex shedding of a circular cylinder. *Journal of Wind Engineering and Industrial Aerodynamics*, 80(3), 263-286.
17. Lin, C., Lin, W.J., Hsieh, S.C. & Dey, S. (2008). Near Wake Flow of a Circular Cylinder Placed Adjacent to a Plane Boundary, *International Conference on Hydrodynamics*.
18. Sarkar, S., & Sarkar, S. (2010). Vortex dynamics of a cylinder wake in proximity to a wall. *Journal of Fluids and Structures*, 26(1), 19-40.
19. Doolan, C. J. (2009). Flat-plate interaction with the near wake of a square cylinder. *AIAA journal*, 47(2), 475-479.
20. Rao, A., Stewart, B. E., Thompson, M. C., Leweke, T., & Hourigan, K. (2011). Flows past rotating cylinders next to a wall. *Journal of Fluids and Structures*, 27(5), 668-679.
21. Cheng, M., & Luo, L. S. (2007). Characteristics of two-dimensional flow around a rotating circular cylinder near a plane wall. *Physics of Fluids*, 19, 063601.
22. Chan, A. S., Dewey, P. A., Jameson, A., Liang, C., & Smits, A. J. (2011). Vortex suppression and drag reduction in the wake of counter-rotating cylinders. *Journal of Fluid Mechanics*, 679(1), 343-382.
23. Thwaites, B., & Meyer, R. E. (1960). Incompressible aerodynamics. *Journal of Applied Mechanics*, 27, 760.

24. Hart, D. P. (2000). PIV error correction. *Experiments in fluids*, 29(1), 13-22.
25. Willert, C. E., & Gharib, M. (1991). Digital particle image velocimetry. *Experiments in fluids*, 10(4), 181-193.
26. Huang, H., Dabiri, D., & Gharib, M. (1997). On errors of digital particle image velocimetry. *Measurement Science and Technology*, 8(12), 1427.
27. Howarth, L. (1938). On the solution of the laminar boundary layer equations. Proceedings of the Royal Society of London. Series A, *Mathematical and Physical Sciences*, 164(919), 547-579.
28. Niemann, H. J., & Hölscher, N. (1990). A review of recent experiments on the flow past circular cylinders. *Journal of Wind Engineering and Industrial Aerodynamics*, 33(1), 197-209.
29. O'Meara, M., & Mueller, T. J. (1987). Laminar separation bubble characteristics on an airfoil at low Reynolds numbers. *AIAA journal*, 25(8), 1033-1041.
30. Alam, M., & Sandham, N. D. (2000). Direct numerical simulation of 'short' laminar separation bubbles with turbulent reattachment. *Journal of Fluid Mechanics*, 410(1), 1-28.
31. Singh, N. K., & Sarkar, S. (2011). DNS of a Laminar Separation Bubble., *World Academy of Science, Engineering and Technology*.
32. Häggmark, C. P., Bakchinov, A. A., & Alfredsson, P. H. (2000). Experiments on a two-dimensional laminar separation bubble. *Philosophical Transactions of the Royal Society of London. Series A: Mathematical, Physical and Engineering Sciences*, 358(1777), 3193-3205.
33. Hu, H., & Yang, Z. (2008). An experimental study of the laminar flow separation on a low-Reynolds-number airfoil. *Journal of Fluids Engineering*, 130(5), 51101.
34. Volino, R. J., & Hultgren, L. S. (2001). Measurements in separated and transitional boundary layers under low-pressure turbine airfoil conditions. *Journal of turbomachinery*, 123(2), 189-197.

35. Ol, M. V., McAuliffe, B. R., Hanff, E. S., Scholz, U., & Kähler, C. (2005). Comparison of laminar separation bubble measurements on a low Reynolds number airfoil in three facilities. *AIAA paper*, 5149(1), 2005.
36. Burgmann, S., Brücker, C., & Schröder, W. (2006). Scanning PIV measurements of a laminar separation bubble. *Experiments in Fluids*, 41(2), 319-326.

## CHAPTER THREE

### NUMERICAL STUDY OF GENERATING ADVERSE PRESSURE GRADIENT OVER A FLAT PLATE USING A ROTATING CYLINDER<sup>\*</sup>

Farhana Afroz, Muhammad A.R. Sharif, Amy Lang

Department of Aerospace Engineering and Mechanics, The University of Alabama

#### Abstract

Generating an adverse pressure gradient, using a rotating cylinder in the proximity of a plane wall under a laminar free stream flow, is studied numerically in this work. The magnitude of the generated adverse pressure gradient is a function of the gap,  $G$ , between the cylinder and the wall and the rotational speed of the cylinder,  $\Omega$ . The flow in such a configuration is characterized by periodic transient vortex shedding at high Reynolds number. A numerical model for the computation of the transient flow for this configuration is developed using the ANSYS Fluent commercial CFD code. The model is validated against published experimental and numerical data of other researchers for similar flow configurations and excellent agreement is observed. A parametric study is carried out for different combinations of  $G$  and  $\Omega$  for two different Reynolds numbers of 200 and 1,000 to examine the development of the resulting separation bubble due to the generated adverse pressure gradient. The mechanism of the boundary layer separation over the plane wall and the corresponding wake dynamics is investigated. Results are presented in terms of the distribution of the pressure coefficient and skin friction coefficient along the wall and flow patterns around and downstream of the cylinder in the proximity of the wall. Computations are also performed for a higher Reynolds number of 6,700 conforming to the conditions of a recent experimental study on similar flow configuration by Farhana et al. (2013). The predicted ensemble-averaged separation bubble development is compared with the

---

<sup>\*</sup>*To be submitted for review in ASME Journal of Fluid Engineering*

experimental results for a few combinations of  $G$  and  $\Omega$ . The numerical predictions for this configuration also, show close agreement with the experimental data. The results of these computations confirm that using a rotating cylinder over a plane wall in a free stream flow is an effective technique to generate controlled range of adverse pressure gradients.

**Keywords:** Adverse pressure gradient, plane wall bounded flow, boundary layer separation, separation bubble, rotating cylinder, transient numerical model.

### 3.1 Introduction

The fluid dynamics of an isolated circular cylinder in a steady free stream cross-flow is well-understood in terms of the vortex shedding phenomenon. When the cylinder is placed near a plane wall, it introduces additional complexity in the flow. The effect of placing a stationary cylinder of diameter,  $D$ , near a stationary plane wall at a gap distance,  $G$ , has been experimentally and numerically investigated by several researchers. Experimental study by Bearman and Zdravkovich [1] suggested that, while vortex shedding was suppressed for small cylinder gap to diameter ratios,  $G/D$ , the flow separated both upstream and downstream of the cylinder on the solid wall. Forces on circular cylinder near wall were measured experimentally for different  $G/D$  values by Zdravkovich [2, 3]. The lift coefficient was found to be governed by the value of  $G/D$ , while the drag coefficient was dominated by the ratio of gap to the boundary layer thickness,  $G/\delta$ .

A numerical investigation was carried by Lei et al. [4] to observe the suppression of the vortex shedding for flow over circular cylinder near a plane wall. The minimum value of  $(G/D)$  at which the vortex shedding could be suppressed was predicted for different Reynolds numbers,  $Re$ , based on the diameter of cylinder and the free stream velocity. The gap ratio  $(G/D)$  was found to have a stronger effect at high Reynolds numbers on the vortex shedding frequency. For intermediate gaps ( $G/D \geq 0.5$ ), the vortex shedding from the cylinder was not interrupted by the wall shear layer.

A significant amount of experimental work has been conducted by Price et al. [5] to study the flow around a circular cylinder near a wall for various Reynolds numbers. Flow visualization studies, using particle image velocimetry and hot-film anemometry, identified four different characteristic configurations based on the gap ratio  $(G/D)$ . For very small gaps ( $G/D \leq 0.125$ )

the flow in the gap is suppressed or extremely weak, and boundary layer separation happens both upstream and downstream of the cylinder. No regular vortex shedding occurs at this range of the gap ratio. For small gap ratio ( $0.125 \leq G/D \leq 0.5$ ), the flow is very similar to that for very small gaps when the inner shear-layer, shed from the cylinder, pairs with the wall boundary layer. The flow for the intermediate gap ratios,  $0.5 \leq G/D \leq 0.75$ , are characterized by the onset of vortex shedding from the cylinder. For large gap ratios,  $G/D \geq 1$ , no wall boundary layer separation, either upstream or downstream of the cylinder, happens.

A vortex-induced instability mechanism occurring in the incompressible wall shear layer has been proposed by Sengupta et al. [6]. According to this theory, instability arises from the interactions between a convecting finite-core vortex and an underlying shear layer and results in unsteady flow separation. Experimental flow visualizations of Price et al. [5] were compared with numerical investigation of Dipankar and Sengupta [4] who explained the vortex induced unsteady flow behavior with the help of vorticity dynamics. For the smaller gap ratio case, a significant interaction between the two vorticity fields occurred, and as a result, the flow over the flat plate suffered unsteady separation upstream and downstream of the cylinder. As the gap ratio increased, major vortex-induced instability was seen to occur near the cylinder surface accompanied by very little instability on the plane wall shear layer.

An experimental investigation was conducted using digital particle image velocimetry [8], to visualize the flow characteristics in the near wake region of a circular cylinder placed close to the wall in a fully developed turbulent boundary layer over a flat plate. The results showed that, the wall effect on cylinder wake was negligible for the gap ratios  $G/D \geq 0.8$ . Within the intermediate gap ratios ( $0.3 \leq G/D \leq 0.6$ ), the wall boundary layer periodically destabilized by the shed vortices from the lower side of cylinder. The evolution of shed vortices

for two representative cases, small gap ratio  $G/D = 0.2$  and intermediate gap ratio  $G/D = 0.6$ , revealed that shed vortices moved downstream parallel to wall with a constant velocity.

An interesting numerical study was done by placing a stationary circular cylinder inside a plane channel and at various distances from the channel wall [9]. In the unsteady regimes, when the cylinder was placed at a far distance from one wall, the vortex shedding produced a similar pattern of von Karman vortex street, even if the confinement due to the channel walls produced an inversion on the position of vortices. But when the cylinder moved very close to the wall, it behaved as a surface-mounted obstacle with a larger resistance. The two layers of opposite signed vorticity, separated from the cylinder and the wall, formed a pair of vortex sheets which dissipated during the mutually induced stretching and eventually substitute von Karman vortex sheet with a unique row of like-signed vortices.

The flow over a circular cylinder, located near a wall moving at the same velocity as the free stream, was studied numerically by Huang and Sung [10]. The moving wall caused the flow in the gap to be accelerated at a much larger rate than that for the stationary wall. As a result, vortex shedding was observed even for small gap ratios compared to the stationary wall case.

The wake dynamics for flow past a rotating cylinder is much more complicated than flow past a stationary cylinder and is of interest due to its potential applications in flow control. Modi et al. [11] described how flow past airfoils could be controlled by increasing lift achieved by placing a hollow rotating cylinder at the leading edge and/or trailing edge as well as the top surface of the airfoil. It is also useful for performance improvement of aircrafts by reducing drag and suppressing vortex resonance [12]. A detailed computational study of flow dynamics of rotating cylinder was conducted by Mittal and Kumar [13] which showed that vortex shedding ceases as the rotation rate of the cylinder increases. When the rotation rate of cylinder is

increased, a positive vortex is developed close to the upper surface of the cylinder, and as the vortex increased in size, it moved outward and away from the cylinder. As a result, it caused the whole wake to deflect upward and a reduction of the cross-stream width of the wake occurred. Moreover, the cause of the flow stability with the increase of the rotation speed was also explained in this study. As the rotation speed increases, the strength of the vorticity increases which accompanies the increase of thickness of the region of closed streamlines around the cylinder, and this results in a stable flow.

When the rotating cylinder is placed near a plane wall, much complexity arises in vortex shedding and wake development compared to that of a stationary cylinder. The resulting flow dynamics is much different than that of an isolated rotating cylinder, or a stationary cylinder near a plane wall. There are only a few studies available which were performed to visualize the flow around a rotating cylinder in the vicinity of a plane wall. Cheng and Luo [14] simulated a two-dimensional incompressible flow using lattice Boltzmann method around a rotating circular cylinder near a plane wall at a Reynolds number of 200. Effects of cylinder rotation rate and gap ratio on the hydrodynamic forces and vortex shedding frequency from the cylinder were obtained. Two critical limiting values of gap were identified, a lower limiting value and an upper limiting value, both of which depended on cylinder rotation rate. Below the lower limiting gap value, the flow was steady and the gap flow was either completely suppressed or extremely weak. Also, the boundary layer separated both upstream and downstream of the cylinder and there was no vortex shedding in the wake, resulting in a stable wake flow. As the cylinder rotation speed increased, the lower limiting gap at which vortex shedding was suppressed, also increased. No boundary layer separation happened on the plane wall, and neither upstream nor downstream of the cylinder for the gaps larger than the upper limiting value. A regular vortex

sheet was observed for flows with these larger gaps. But, the upper limiting value of the gap weakly depended on cylinder rotation rate. One interesting phenomenon reported in the numerical study of two-dimensional flow by Cheng and Luo [15] was that, for moderate Reynolds numbers ( $20 \leq Re_D \leq 750$ ), a reverse rotation (aiding the flow in the gap between the wall and the cylinder) of the cylinder can completely suppress the vortex shedding.

Flow separation occurs when a flow encounters an adverse pressure gradient (APG). Understanding the mechanism of boundary layer separation is very important because of its occurrence in various applications such as lifting surfaces, turbine blades, diffusers, etc. Flow separation can increase drag and results in a considerable limitation on operating characteristics of airfoils, propellers, and turbines which leads to a significant degradation of overall performance. For practical importance, research trends focus on understanding the flow separation dynamics and delaying or controlling this flow separation. Little research has been done to develop a system to generate an APG over flat plate to induce laminar and turbulent separation. To study the physics of boundary layer separation, more research needs to be done for developing simple systems which will allow imposing wide variation of APG. In the case of turbulent boundary layer separation, although there are many numerical and experimental works done, the process leading to separation and the ability to completely control flow separation has not been fully understood. Turbulent boundary layer separation can be induced by surface curvature, APG, or combination of both. Simpson [16] summarized the effects of surface curvature on turbulent separation bubble and as the surface curvature changes sharply, the outer-region streamlines do not curve rapidly. To understand the structure of turbulent separation without the effect of surface curvature, research must be carried out for developing systems where only an APG is present over a flat surface.

One widely used system of imposing APG over plane surface is by changing the contour of wall making it a convex wall; as a result flow separation occurs due to area change over the surface [17-20]. The magnitude of the APG is varied by varying the top wall contour. In this method, after a short region of favorable pressure gradient, an adverse pressure gradient induces the separation bubble. But this technique requires an additional arrangement, such as wall suction, to prevent boundary layer separation over the top wall itself for high curvatures and thus high APG.

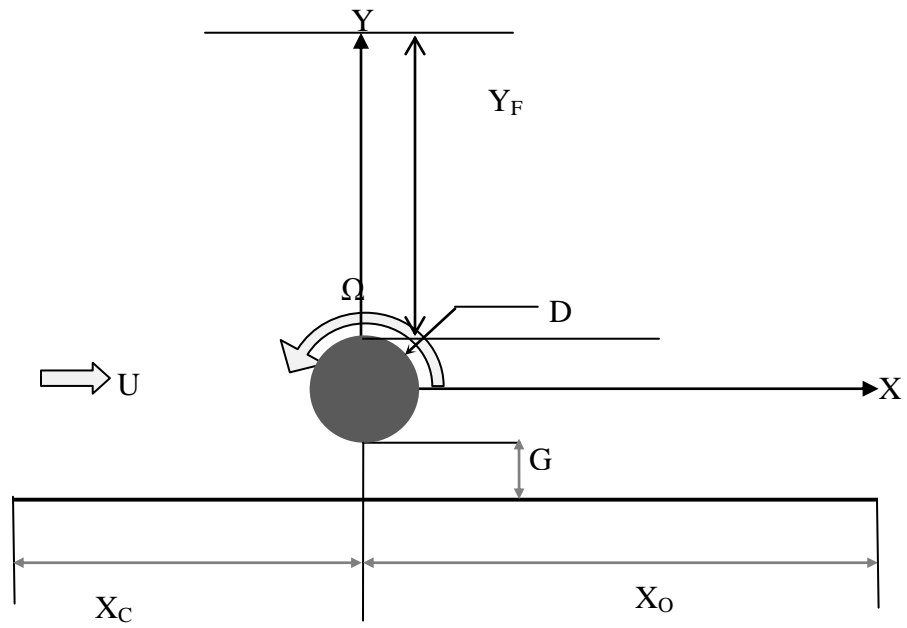
From the literature review of flow over a circular cylinder it can be comprehended that, when a circular cylinder rotates near a flat plate, the wake behind the cylinder and the flow along the wall mainly depends on four parameters: the boundary layer thickness on the flat wall, the rotation rate of the cylinder, the Reynolds number, and the gap ratio ( $G/D$ ). An innovative and easy technique has been developed to induce various magnitudes of APG by using a rotating cylinder in the water tunnel laboratory at the University of Alabama. Experimental studies [20-22] were conducted in the water tunnel to analyze laminar and turbulent boundary layer separation using Time-Resolved Digital Particle Image Velocimetry (TR-DPIV). The results showed that the cylinder rotation speed and the gap ratio impact the nature and extent of the laminar and turbulent separation regions. Experimentally measured separation points for both laminar and turbulent conditions produced good agreement with theoretical predictions. This system has been proven to be an effective method to induce both laminar and turbulent boundary layer separation.

There is a potential research scope to identify the range of cylinder gap ( $G/D$ ) for different rotation speeds where the cylinder wake will not interfere with the wall shear layer and no external disturbances can influence flow separation over a flat wall. The present numerical

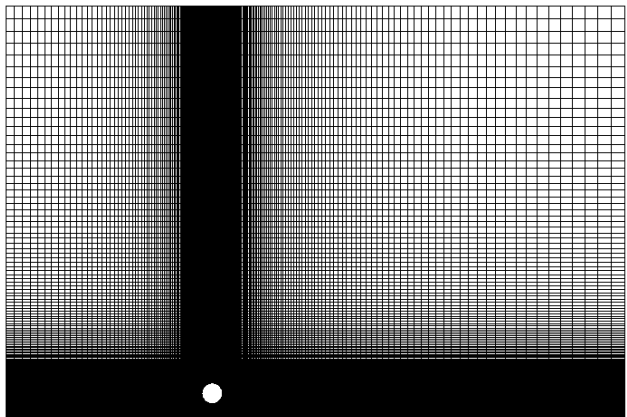
study addresses this particular flow configuration and focuses on visualizing the wake dynamics and mechanism of boundary layer separation over a flat plate. Moreover, the pressure gradient along the flat plate is numerically obtained for different combinations of rotation speed and cylinder gap. To the best of the knowledge of the present authors, this is the first study to be performed for this flow configuration.

### 3.2 Problem Description

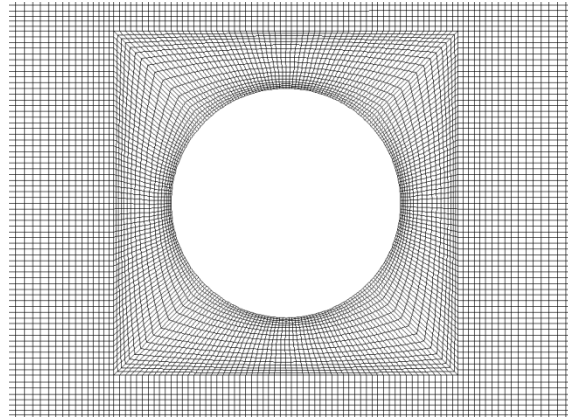
A circular cylinder rotating near a plane wall as shown in fig. 3.1 (a) has been used in the present numerical analysis. The dimensions of the computational domain are  $L_x \times L_y = 30D \times 20D$  in size and the cylinder center is situated  $10D$  downstream from the left inlet boundary. The center of the cylinder is taken as the geometric origin of the domain. The study has been conducted for three different Reynolds number,  $Re = 200, 1,000$  and  $6,700$ , where the Reynolds number is defined as  $Re = \frac{UD}{\nu}$ . The cylinder gap to diameter ratio ( $G/D$ ) is varied from  $0.25$  to  $1.0$  and the non-dimensional cylinder rotation speed,  $VR$ , defined as  $\Omega D/2U$ , is varied from  $0.125$  to  $2$ . The wake dynamics and mechanism of separation formation has been analyzed for different combinations of Reynolds number, cylinder gap and cylinder speed. It has been proven to be an effective method to generate different values of APG as a function of cylinder gap,  $G/D$ , and cylinder speed,  $VR$ , for this range of Reynolds number. The ensemble averaged skin friction coefficient,  $\overline{C_f}$ , along the wall is used here to identify the separation and reattachment point for the separation bubble under different values of the APG.



(a)



(b)



(c)

Fig. 3.1. (a) Schematic diagram of flow configuration, (b) Sample mesh, and (c) zoomed view of mesh around the cylinder.

### 3.3 Numerical Procedure

#### 3.3.1 Governing equations

The governing equations are the continuity and Navier-Stokes equation. The mass balance is described by continuity equation (1).

$$\frac{\partial \rho}{\partial \tau} + \rho \frac{\partial u_i}{\partial x_i} = 0 \quad (1)$$

Compared to the steady case, the unsteady case includes an additional time-derivative term in the Navier-Stokes equations:

$$\frac{\partial(\rho \vec{u})}{\partial \tau} + \rho(\vec{u} \cdot \nabla) \vec{u} = -\nabla p + \mu \nabla^2 \vec{u} \quad (2)$$

Here,  $p$ ,  $u$ ,  $\tau$  are the pressure, velocity, and time, whereas  $\rho$  and  $\mu$  are the fluid density and dynamic viscosity.

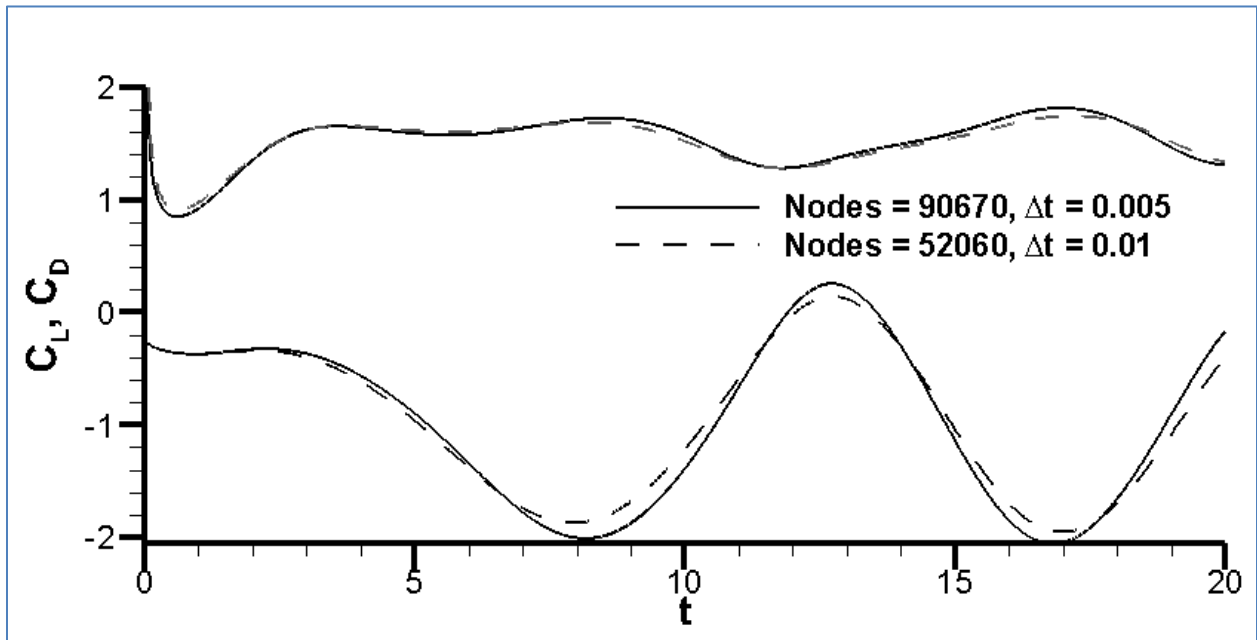


Fig. 3.2 Grid independence and time step independence study  $Re = 1000$ ,  $G/D = 0.5$ ,  $VR = 0.5$

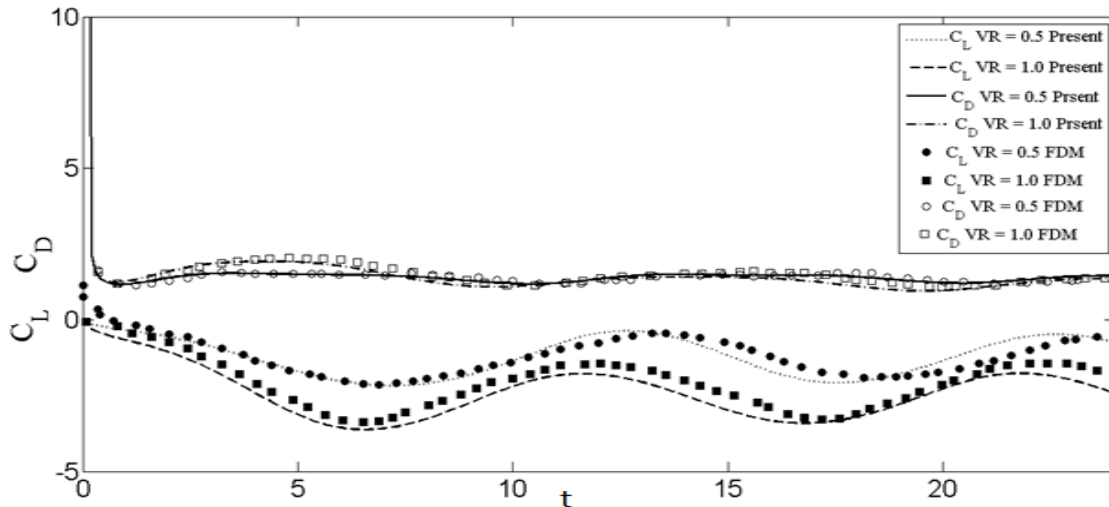


Fig. 3.3. Comparison of the time evolution of the lift and drag coefficients between the present computation and that in [25] for flow past a rotating circular cylinder without any wall in the vicinity at  $Re = 200$  and  $VR = 0.5$  and  $1.0$ .

### 3.3.2. Boundary Conditions

The boundary conditions are given as a uniform flow ( $U$ ) at the inflow boundary located on the left, a constant pressure outlet boundary at the right, far-field boundary at the top with a flow velocity of  $U$ , and a no-slip wall boundary at the bottom. The cylinder surface is set as a moving rotational wall and all the cylinder rotation rate,  $\Omega$ , is in the counter-clockwise direction.

### 3.3.3. Computational Details

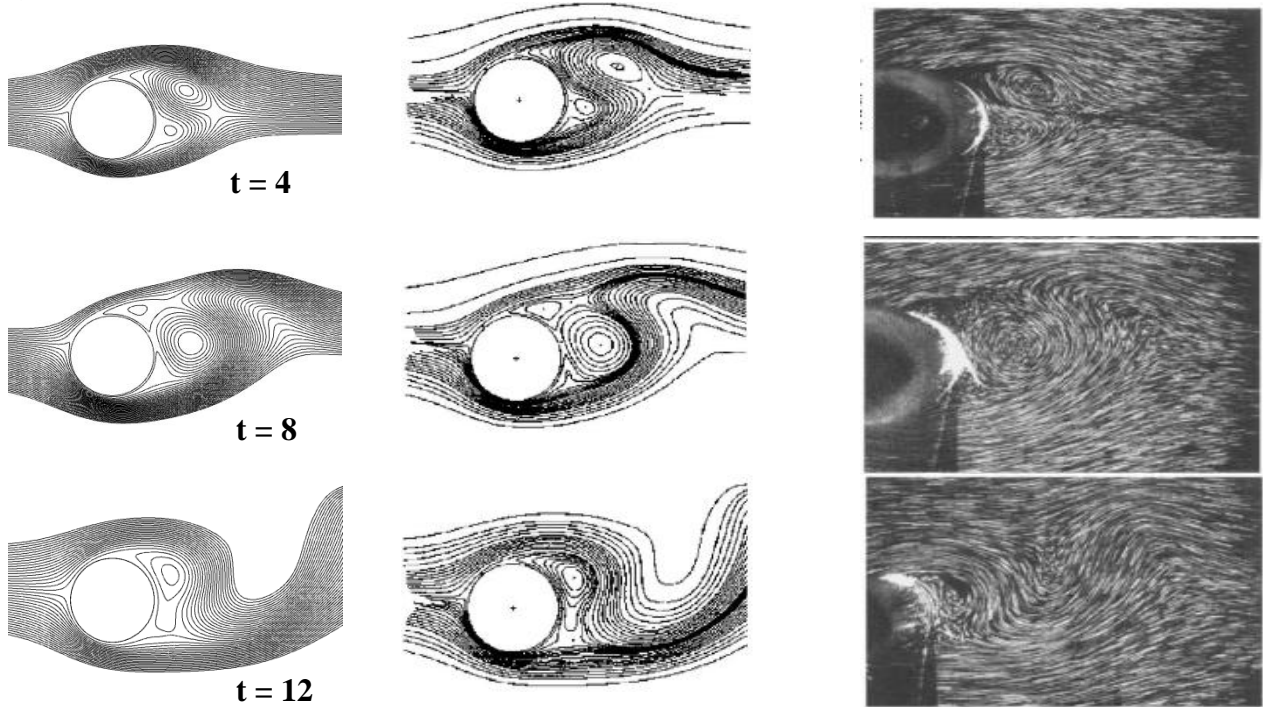
A non-uniform finite volume mesh with collocated variable locations is used for the computations. The computational domain is a rectangular window. A boolean operation has been performed to subtract the circular cylinder from the rectangle. A small rectangle is created outside the circular cylinder for generating uniform o-type mesh around the cylinder. Outside the small rectangle, rest of the domain is meshed with an expanding grid from small rectangle outlet to right, left, top and bottom boundary using a suitable bias factor. A sample mesh is shown in fig 3.1(b) and (c). The computations are performed using commercial software ANSYS Fluent

13.0 [26]. The set of governing equations are integrated over the finite volumes, which produces a set of linear algebraic equations. The pressure velocity coupling is done using the well-known SIMPLE method. The transient formulation is calculated using second order (both temporal and spatial) implicit method.

For the numerical computation, the inlet velocity  $U$  (also the reference velocity) is taken as 1 m/s, the cylinder diameter,  $D$  (also the reference length) is taken as 1 m and the constant fluid density,  $\rho$  (also the reference density) is taken as 1 kg/m<sup>3</sup>. Thus the Reynolds number,  $Re$  becomes the function of only dynamic viscosity,  $\mu$  which is taken as 1/Re kg/m s. The non-dimensional time,  $t$  is defined as  $t = \frac{\tau U}{a} = \frac{2\tau U}{D}$ , i.e.,  $t = 2\tau$  since  $U$  and  $D$  both are assigned a unit value.

The Strouhal number for the flow past cylinder is roughly 0.2 for a wide range of Reynolds number. In order to capture the shedding correctly, at least 20 to 25 time steps in one shedding cycle should be ensured. The cycle period for one shedding is roughly 5 second and a time step duration of about 0.2 second should give a reasonable result. However, the time stepping method is fixed to as low as 0.01 second and maximum 30 iterations per time step is specified during calculation. The flow field is allowed to evolve for sufficient number of vortex shedding cycles to get a dynamically periodic steady condition. The lift and drag coefficients plot shows that it attains to a dynamically steady periodic condition after a dimensionless time period of  $t = 100$ . Then the data are collected for at least 15 vortex shedding cycles at dynamic steady condition for ensuring a good time-averaging velocity field which is also found to be sufficient to ensure statistically converged results [28]. The solution is considered converged when the normalized residual falls below  $10^{-6}$  for the governing transport equations.

a)  $VR = 0.5$



(b)  $VR = 1$

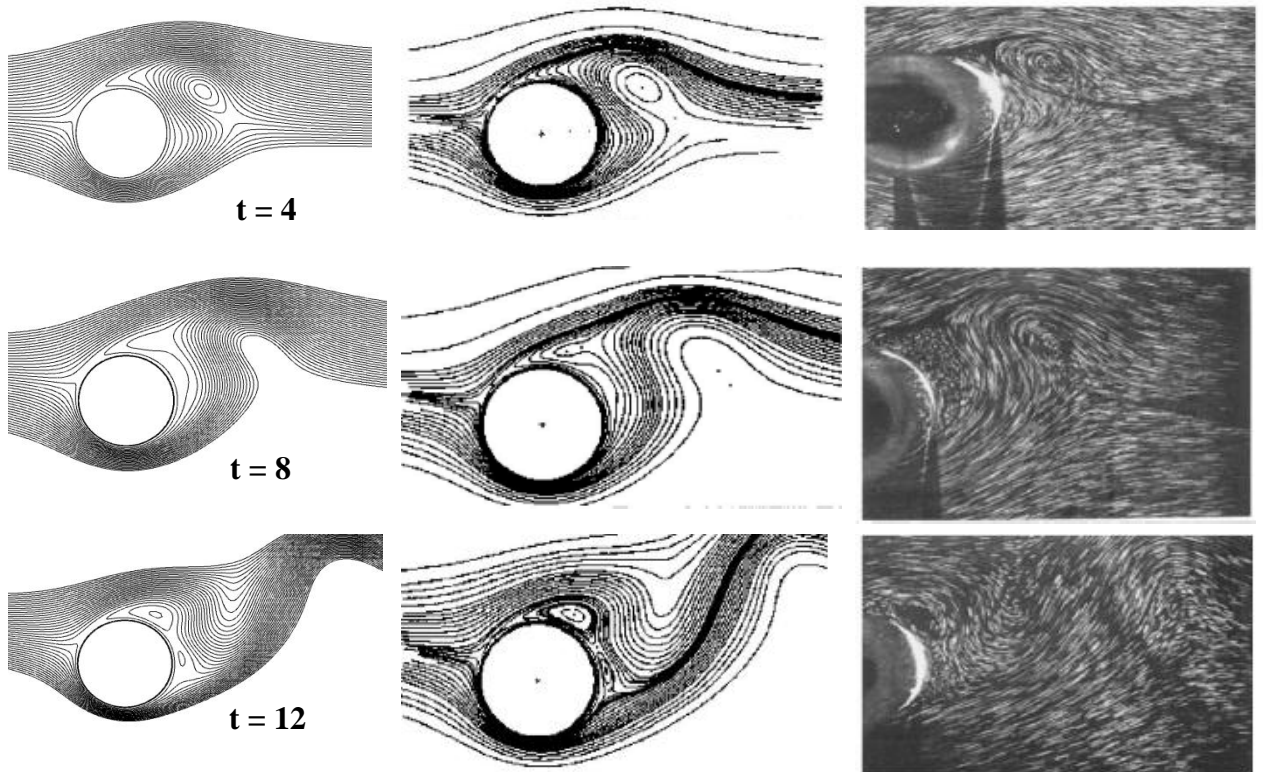


Fig. 3.4. Instantaneous streamlines around the rotating cylinder at different times for  $Re=200$ ; present study (left), semianalytical method [23] (center), and experimental flow visualization [23] (right).

### 3.3.4. Numerical Model Validation

In order to determine the optimal spatial mesh resolution and optimal time step for the transient flow computations, two different meshes and two different time steps (52,060 cells with a time step of 0.01 and 90,670 cells with a time step of 0.005) were used to compute the flow for a  $G/D$  value of 0.5. The time history of the lift and drag coefficients at the cylinder for these two meshes with the two mentioned time steps, plotted in fig. 3.2, indicates insignificant change. Based on these evidences, a mesh with 52,060 cells and a time step of 0.01 is deemed optimal and used for all computations in this study.

The model predictions are validated against the semi-analytical numerical and experimental data for flow past an isolated rotating circular cylinder studies [23-25]. Fig. 3.3 shows comparison, between the present computation and [25], of the time evolution of the lift and drag coefficients for flow past an isolated cylinder at  $Re = 200$  and  $VR = 0.5$  and  $1.0$  where a strong agreement is noticed. The comparison of the instantaneous streamlines at different dimensionless time,  $t$ , for the flow past an isolated rotating circular cylinder at  $Re = 200$  and  $1,000$ , with  $VR = 0.5$  and  $1.0$  are presented in fig. 3.4 and fig. 3.5. The comparison is between the present computation and those obtained by a semi-analytical method and experiments [23-25] where excellent agreement is noticed. The validation is further acknowledged in fig. 3.6 by the excellent agreement of the predicted instantaneous velocity profiles at different times, along the horizontal line through the center of the cylinder, with the semi-analytical results of Badr and Dennis [23, 25] for  $VR = 0.5$ .

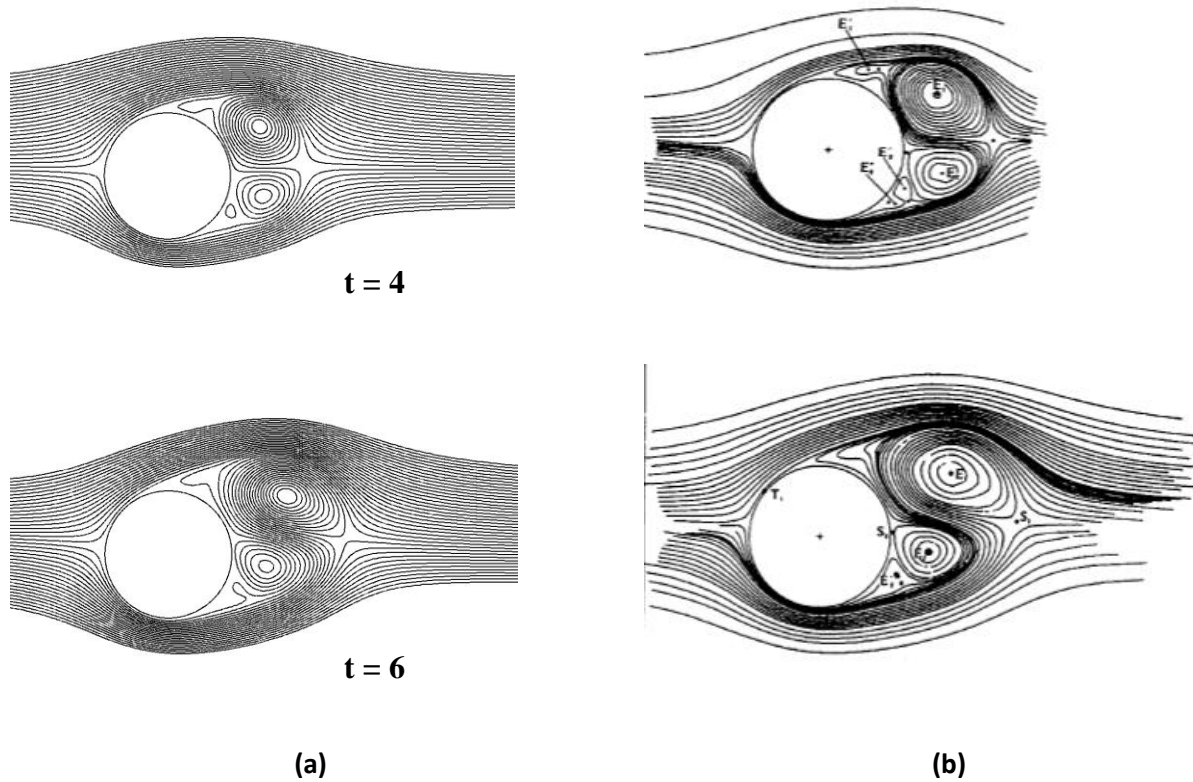


Fig. 3.5 Instantaneous streamlines around the rotating cylinder at different times for  $Re=1,000$  and  $VR = 0.5$ ; present study (left) and semianalytical method [25] (right).

### 3.4. Results and Discussions

Being confident about the predictive capability of the numerical model through the mesh and time step refinement study as well as validation of the predictions against semi-analytical and experimental data of other researchers [23-25], a parametric study of the flow in similar configurations has been conducted. The flow and geometric parameters considered are the Reynolds number,  $Re$ , the non-dimensional gap between the wall and the cylinder bottom designated as the gap ratio,  $G/D$ , and the non-dimensional velocity of the cylinder surface designated as the velocity ratio,  $VR$ . Two specific Reynolds number has been considered– 200 and 1,000. The value of  $G/D$  has been varied as 0.25, 0.5, 0.75, and 1 whereas  $VR$  has been varied as 0.25, 0.5, 1, 1.5, and 2. Thus, a total of 40 cases are computed and the results are systematically analyzed to understand the effects of variation of the gap ratio and the velocity

ratio on the development of the resulting flow separation and the separation bubble. These analyses are done based on the time averaged results which are obtained by averaging the instantaneous computed data when the steady periodic flow cycles are established for any case. The data over few steady periodic cycles are averaged over time. These results are presented and discussed in the next few sections.

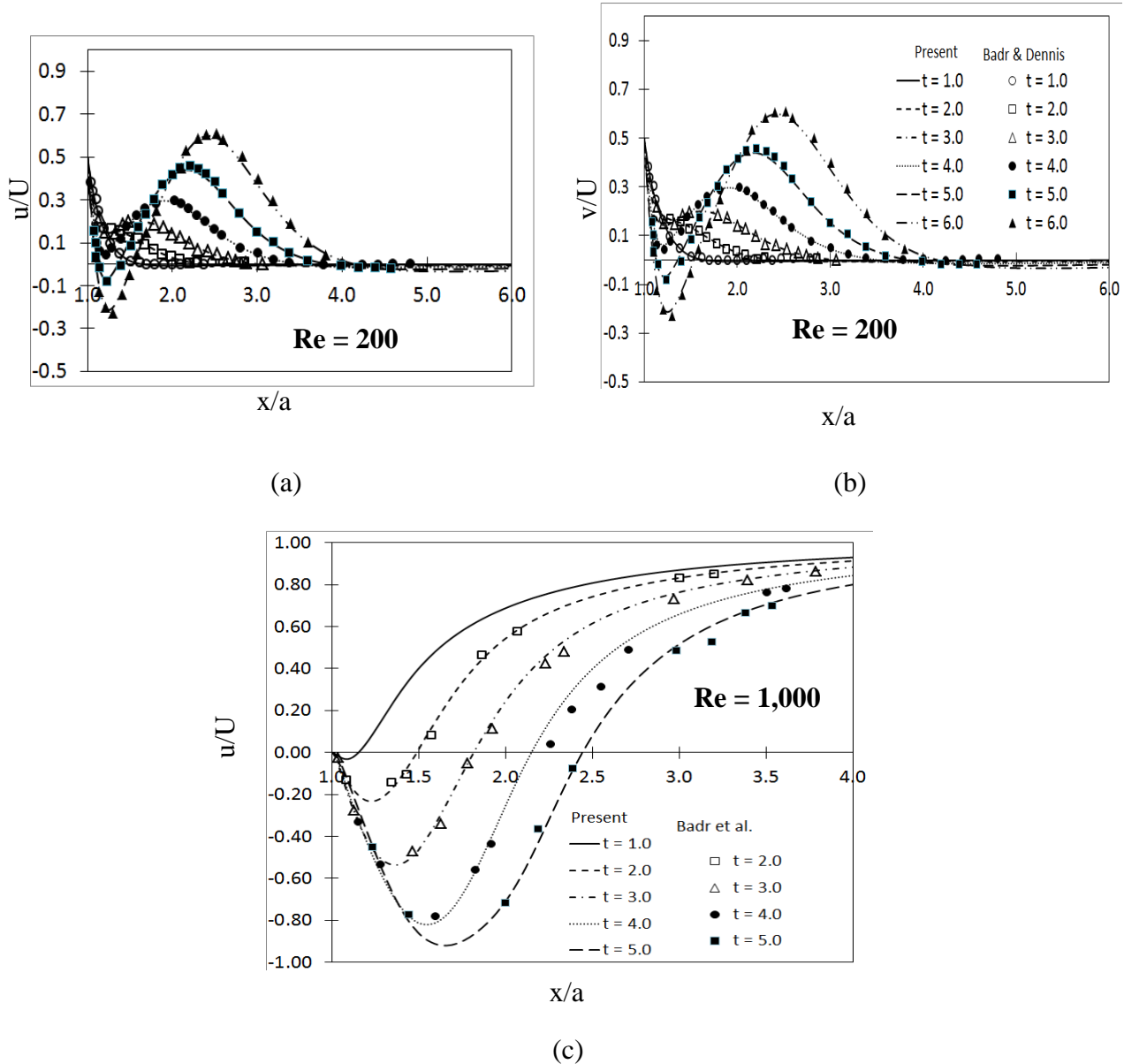


Fig. 3.6. Comparison of velocity profiles, along the horizontal line through the center of the cylinder, with the semi analytical results of Badr and Dennis [23, 25] for  $VR = 0.5$ .

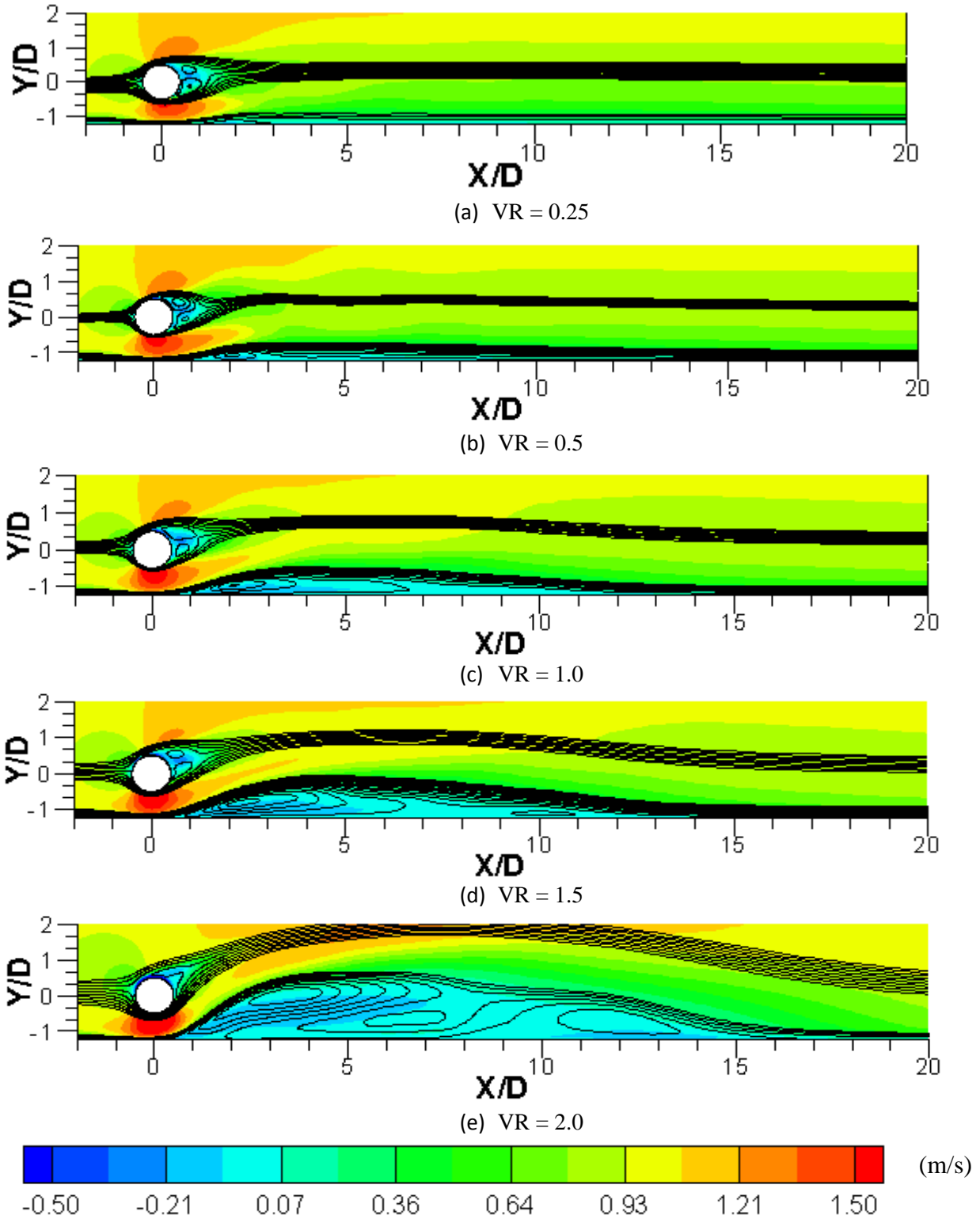


Fig. 3.7. Time-averaged stream wise velocity contours along with few selected streamlines for different cylinder speed ( $VR$ ) at  $Re = 1,000$  and  $G/D = 0.75$

### 3.4.1. Time-averaged Flow Feature

Some representative time-averaged streamlines are plotted for few combinations of  $VR$ ,  $G/D$ , and  $Re$  to gain insights about the modifications of wake dynamics of the circular cylinder as well as the wall boundary layer separation mechanism as the rotating cylinder is placed in the proximity to the plane wall. These cases are divided into two categories. In the first category, the cylinder rotation speed is varied for fixed gap ratios (0.75 and 0.25) and Reynolds number (1,000 and 200) while in the second category, the gap ratio is varied for fixed cylinder rotation speed (0.5 and 0.25) and Reynolds number (1,000 and 200). The effects of variation of the cylinder rotation speed and the gap ratio is examined by looking at the time averaged flow streamlines and the distribution of the time averaged pressure coefficient and the skin friction coefficient. The pressure coefficient is defined in terms of the free stream pressure,  $p_0$ , the wall pressure,  $p_w$ , and the freestream dynamic pressure,  $\frac{1}{2}\rho U^2$ , as  $C_p = \frac{p_w - p_0}{\frac{1}{2}\rho U^2}$  while the skin friction coefficient,  $C_f$ , is defined in terms of the wall shear stress,  $\tau_w$ , and freestream dynamic pressure as  $C_f = \frac{\tau_w}{\frac{1}{2}\rho U^2}$ . These plots are important because the negative values of  $C_p$  and  $C_f$  are indicative of adverse pressure gradient and flow separation. These effects are presented and discussed separately in the next two subsections for the above mentioned two categories.

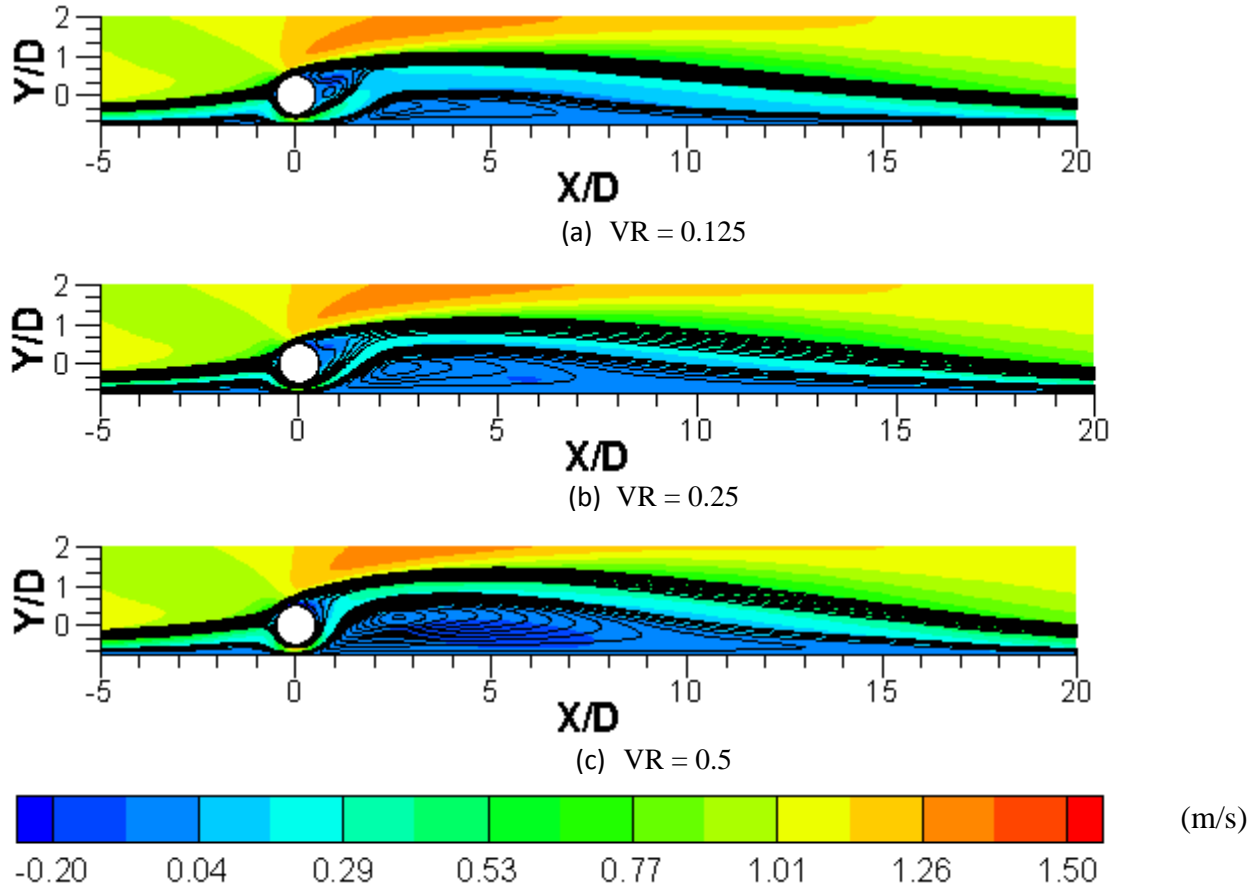


Fig. 3.8. Time-averaged stream wise velocity contours along with few selected streamlines for different cylinder speed ( $G/D$ ) at  $Re = 200$  and  $G/D = 0.25$

### 3.4.1.1. Effect of Cylinder Rotational Speed on Adverse Pressure Gradient

The time averaged streamline patterns for varying cylinder speed are shown in fig. 3.7 for a fixed  $G/D = 0.75$  and  $Re = 1,000$  and in fig. 3.8 for a fixed  $G/D = 0.25$  and  $Re = 200$ . In these plots the streamlines are the solid lines drawn in a background of the flooded contour of magnitude of the  $x$ -velocity components. These streamline plots qualitatively show the effect of cylinder speed and gap on the development of the separation bubble. The corresponding time averaged distribution of the pressure coefficients and skin friction coefficients are plotted in figs. 3.9 and 3.10.

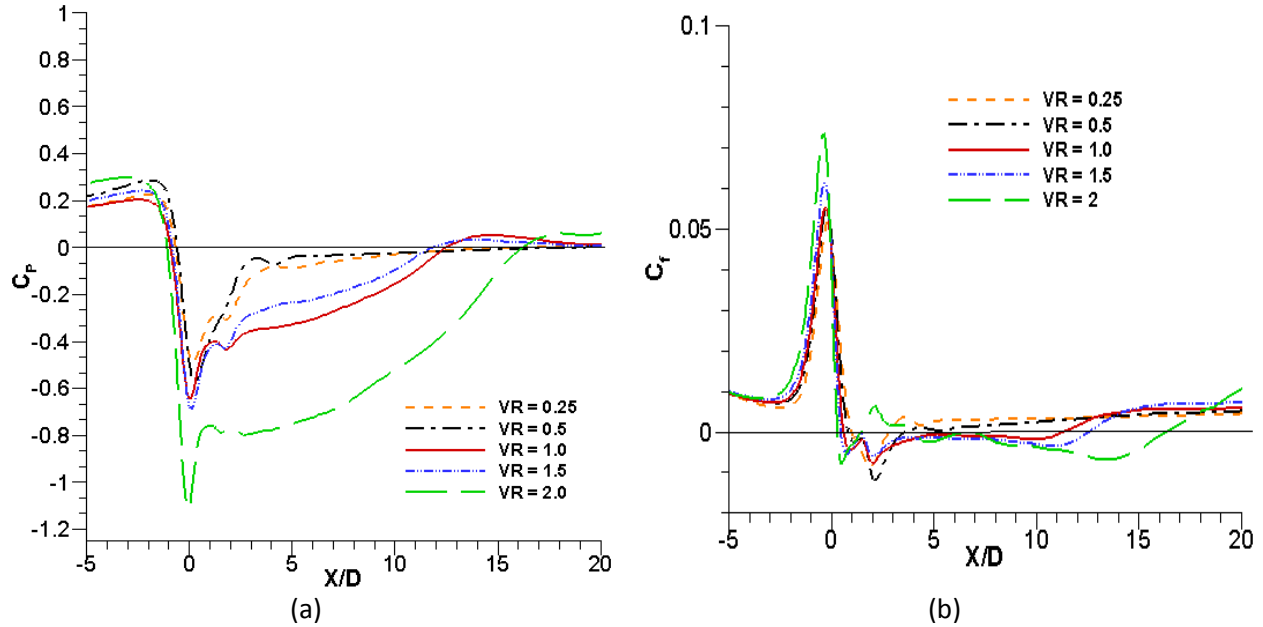


Fig. 3.9 (a) Distribution of the mean pressure coefficient ( $C_p$ ) along the wall and (b) distribution of the mean skin friction coefficient ( $C_f$ ) on the wall for different cylinder speed for  $Re = 1,000$  and  $G/D = 0.75$

It is seen from these figures that, starting the inlet location ( $X = -5$ ) the pressure coefficients mildly increases to a peak near the upstream of the cylinder and then sharply drops to a negative minimum at the location right below the cylinder bottom ( $X \approx 0$ ) and then gradually increases with a plateau in  $C_p$  that tends to recover downstream. This is due to the fact that the flow accelerates as it approaches the region between the cylinder bottom and the wall. The magnitude of the difference between the peak and minimum pressure coefficients (the sudden drop) increases with the increase of the cylinder speed and the magnitude of negative  $C_p$  value increases with a large plateau indicating a large separation region in the presence of the induced adverse pressure gradient. As for the skin friction coefficient, a sharp rise upstream of  $X = 0$  can be seen as flow accelerates beneath the cylinder. As cylinder rotation rate increases, higher speed flow is induced in the gap and as a result, the peak of  $C_f$  increases due to the maximum negative pressure at this zone. Downstream of this zone,  $C_f$  becomes negative and this point is identified as the onset of separation and the point where  $C_f$  attain the positive value again is identified as

reattachment points. It can be seen from the streamlines as well as  $C_f$  plots (figs. 3.7 and 3.9b), that for higher cylinder rotation speed, the separation happens early and separation bubble increases in size. For higher rotation rate ( $VR = 2$ ), the separation bubble has complex structure having secondary positive bubble which reflects the evolution of mean skin friction,  $C_f$  along the wall. If the gap ratio is small ( $G/D = 0.25$ ), the flow also separates upstream of cylinder as can be seen in fig. 3.8. Fig. 3.10b shows the  $C_f$  distribution along the wall for three different cylinder rotation speeds at  $G/D = 0.25$ . It shows that  $C_f$  drops close to zero, upstream of the cylinder, then rise to a peak value which happens for moderate gap ratios. At these gap ratios, early separation and increase of the separation size downstream of the cylinder occurs for higher cylinder rotation speed.

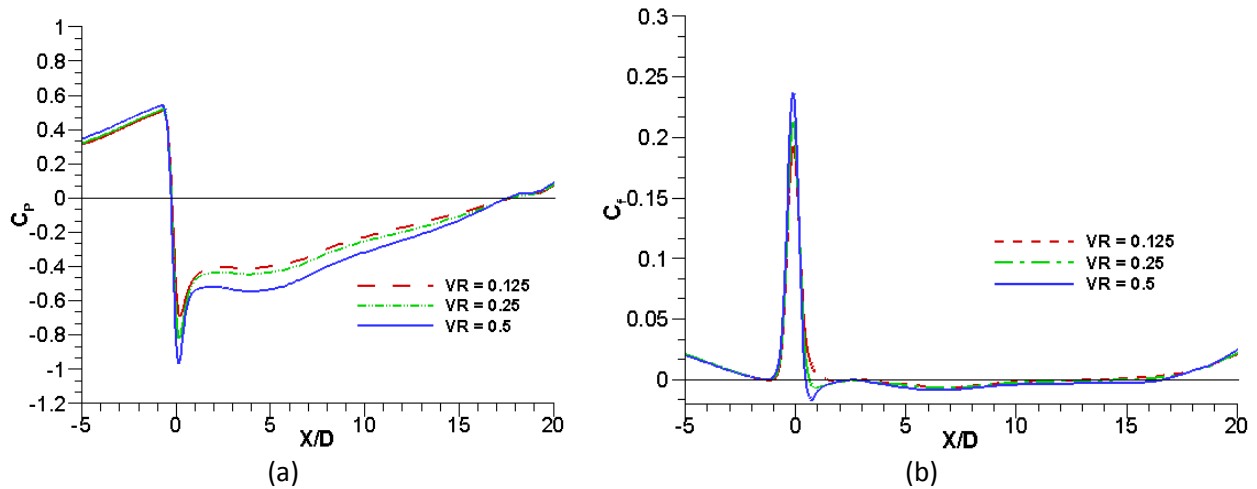


Fig. 3.10 (a) Distribution of the mean pressure coefficient ( $C_p$ ) along the wall and (b) distribution of the mean skin friction coefficient ( $C_f$ ) on the wall for different cylinder speed for  $Re = 200$  and  $G/D = 0.25$

#### 3.4.1.2. Effect of Cylinder Wall Gap on Adverse Pressure Gradient

The strength of APG is not only a function of cylinder rotation speed ( $VR$ ), it is also a function of gap ratio,  $G/D$ . To investigate the effects of varying the gap ratio on the separation bubble development, some representative time averaged streamline patterns for varying cylinder to wall gap are plotted in fig. 3.11 for a fixed  $VR = 0.5$  and  $Re = 1,000$  and in fig. 3.12 for a fixed

$VR = 0.25$  and  $Re = 200$ . These plots demonstrate that as the cylinder moves closer to the wall, early separation occurs and the size of the separation bubble also increases. The corresponding distribution of the pressure coefficient and the skin friction coefficient along the wall for these cases are shown in figs. 3.13 and 3.14.

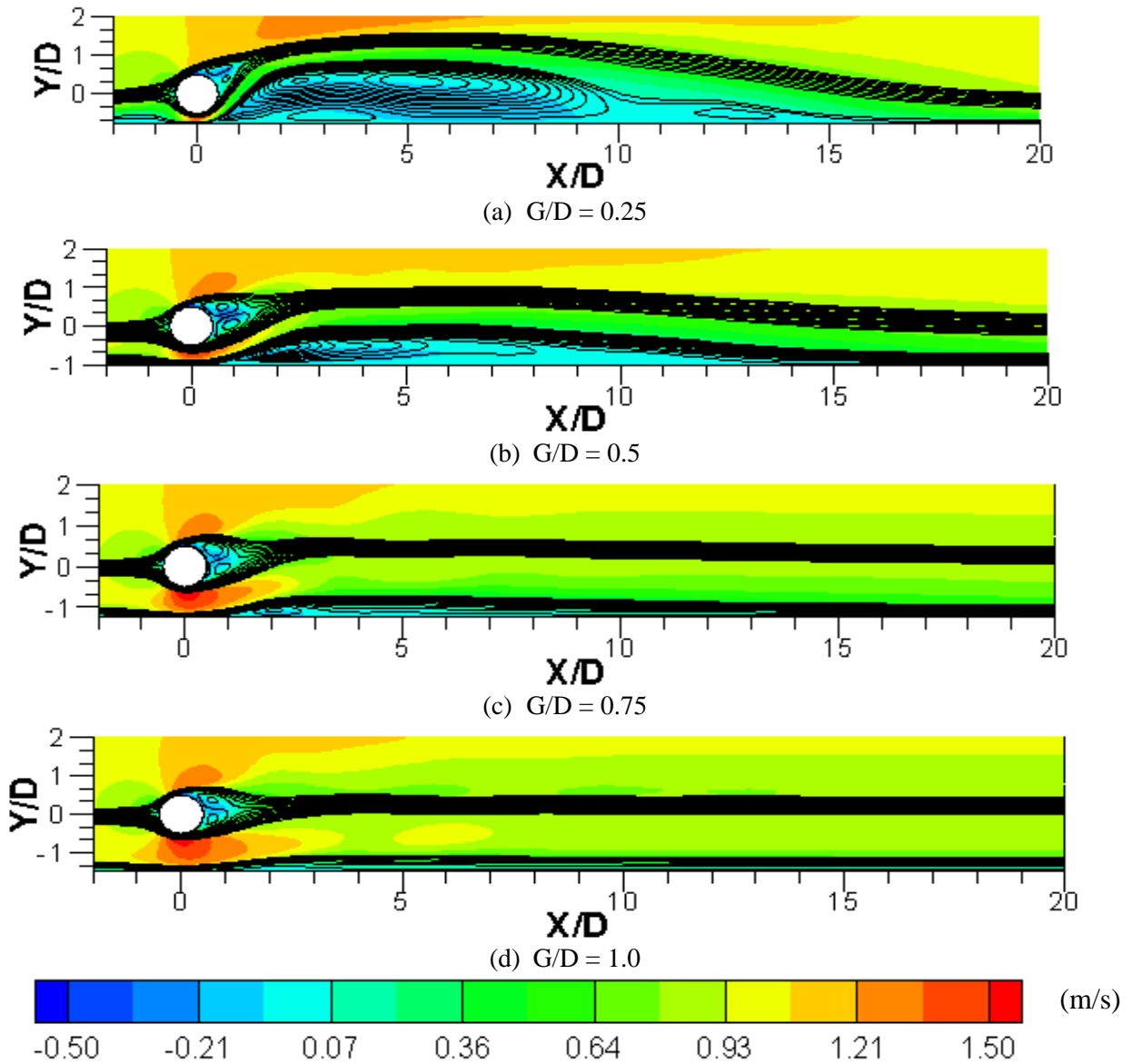


Fig. 3.11 Time-averaged stream wise velocity contours along with few selected streamlines for different cylinder gap ( $G/D$ ) at  $Re = 1000$ ,  $VR = 0.5$  (corresponding to the cases in fig. 3.13)

While the general behavior pattern of the variation of  $C_p$  and  $C_f$  is similar to those presented in the figs. 3.9 and 3.10, some features are evident. As the gap ratio is gradually increased from 0.25, the flow decelerates more and more in the gap, resulting in a gradual decrease of the upstream peak value of  $C_p$  and the corresponding sudden drop to the minimum value. So, with an increase of the  $G/D$  ratio, the magnitude of negative  $C_p$  value decreases with a smaller plateau illustrating a smaller separation region. Here an important phenomenon can be observed as the location of the minimum  $C_p$  moves a little downstream, whereas the location of the maximum  $C_p$  moves upstream with the increase in the gap ratio. Similar effects were also found in the experiments conducted by Choi and Lee [28].

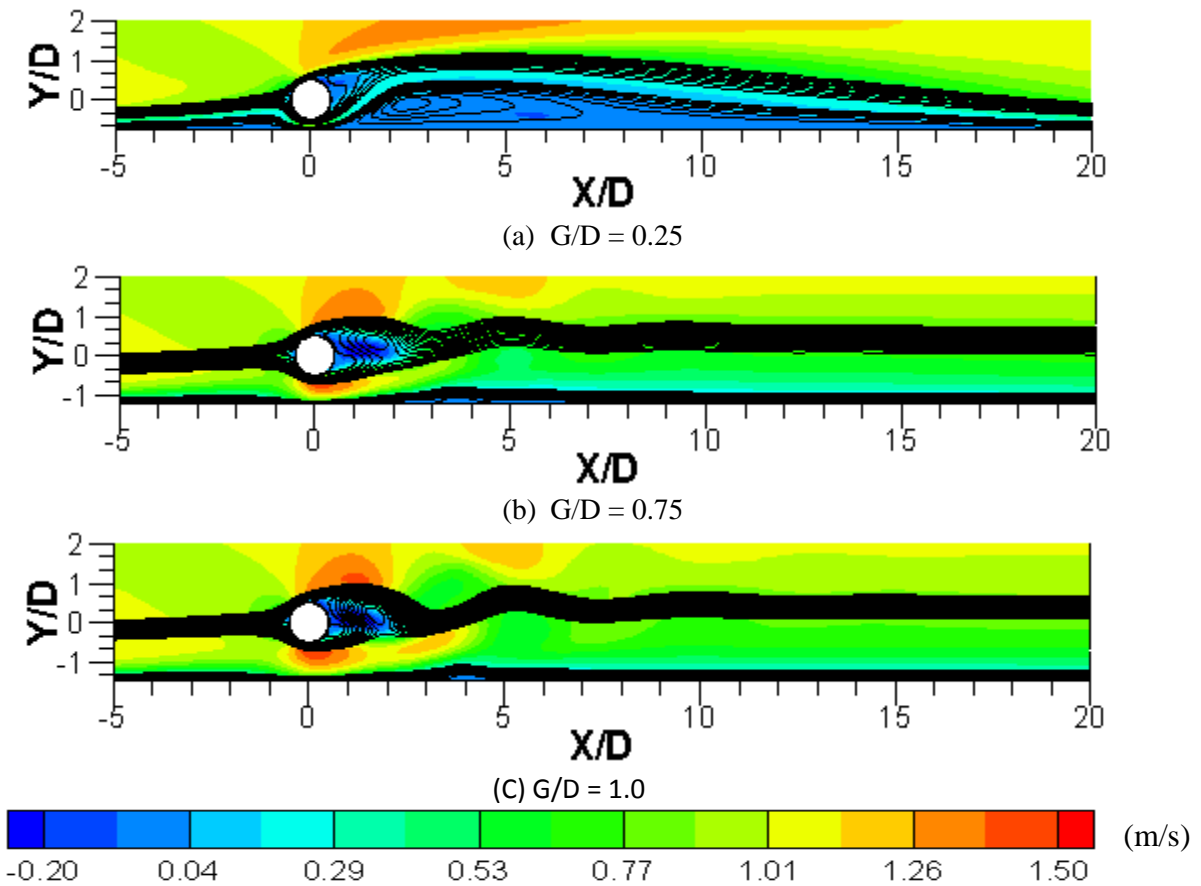


Fig. 3.12 Time-averaged stream wise velocity contours along with few selected streamlines for different cylinder gap ( $G/D$ ) at  $Re = 200$ ,  $VR = 0.25$  (corresponding to the cases in fig. 3.14)

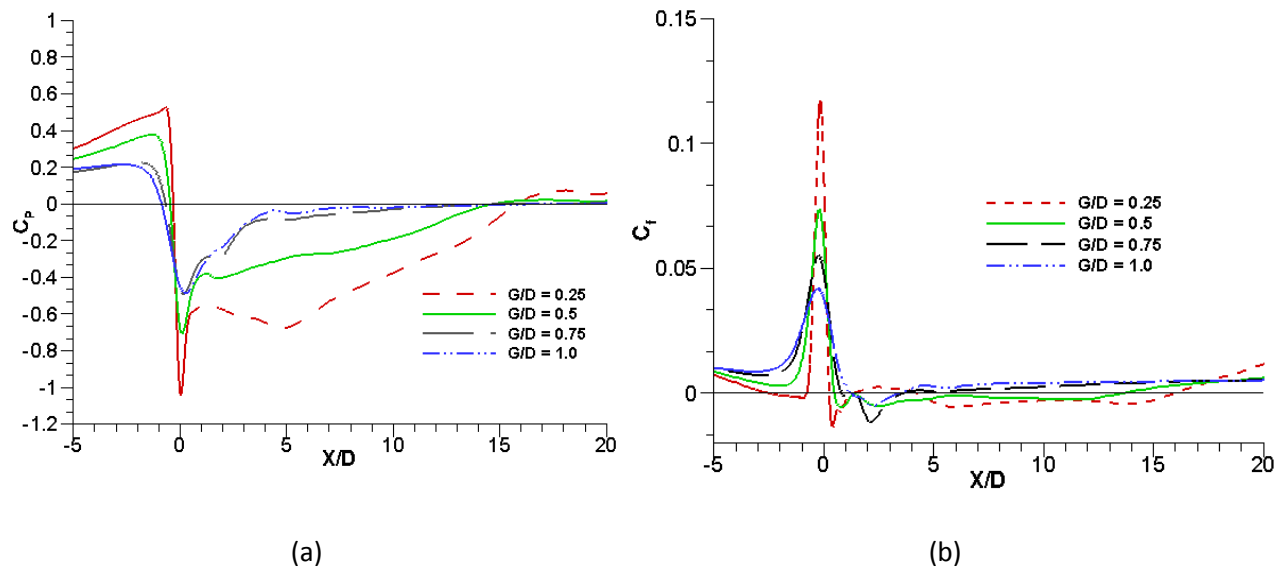


Fig. 3.13 (a) Profiles of mean pressure coefficient on the wall ( $C_p$ ), (b) Profiles of mean coefficient of friction ( $C_f$ ) on the wall for different cylinder gap ( $G/D$ ) at  $Re = 1000$ ,  $VR = 0.5$

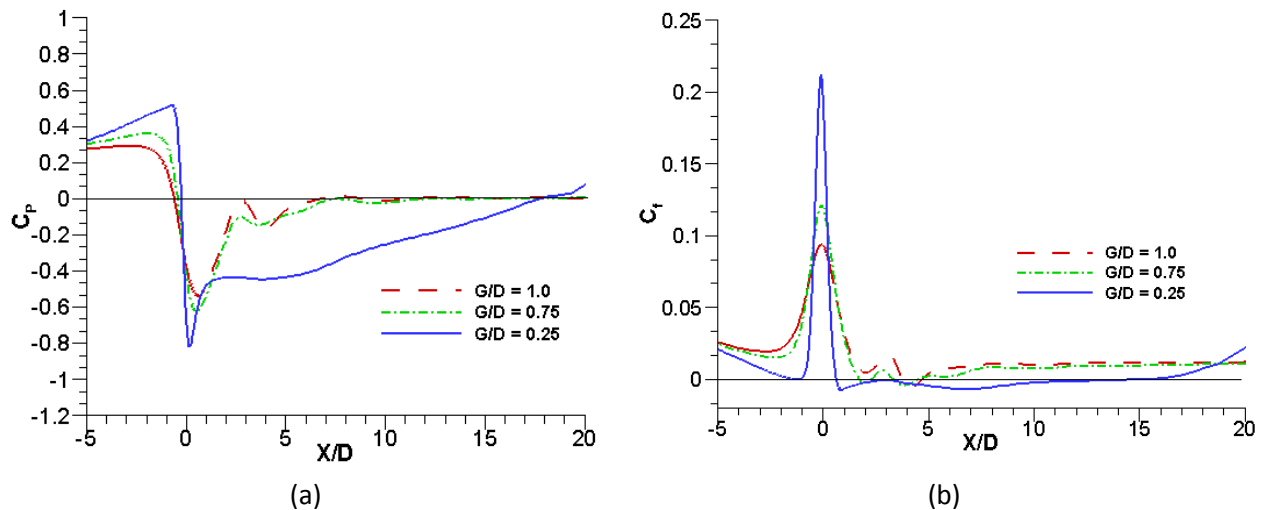


Fig. 3.14 (a) Profiles of mean pressure coefficient on the wall ( $C_p$ ), (b) Profiles of mean coefficient of friction ( $C_f$ ) on the wall for different cylinder gap ( $G/D$ ) at  $Re = 200$ ,  $VR = 0.25$

Fig. 3.13b shows the time averaged skin coefficient,  $C_f$  along the wall for 4 different gap ratios while keeping cylinder rotation speed,  $VR$ , fixed at 0.5 for  $Re = 1,000$ . For  $G/D = 0.25$ ,  $C_f$  becomes negative at an upstream position indicating an upstream separation, which is absent at higher gap ratios. As the gap ratio gradually decreases from 1, the peak of  $C_f$  increases beneath

the cylinder since the flow directly below the cylinder accelerates with decreasing gap height. Fig. 3.14b shows the time averaged skin friction coefficient,  $C_f$ , along the wall for  $VR = 0.25$  and for three different cylinder gap ratios at  $Re = 200$ . For lower gap ratio ( $G/D = 0.25$ ), there is a presence of a secondary positive bubble indicated by the negative  $C_f$  values.

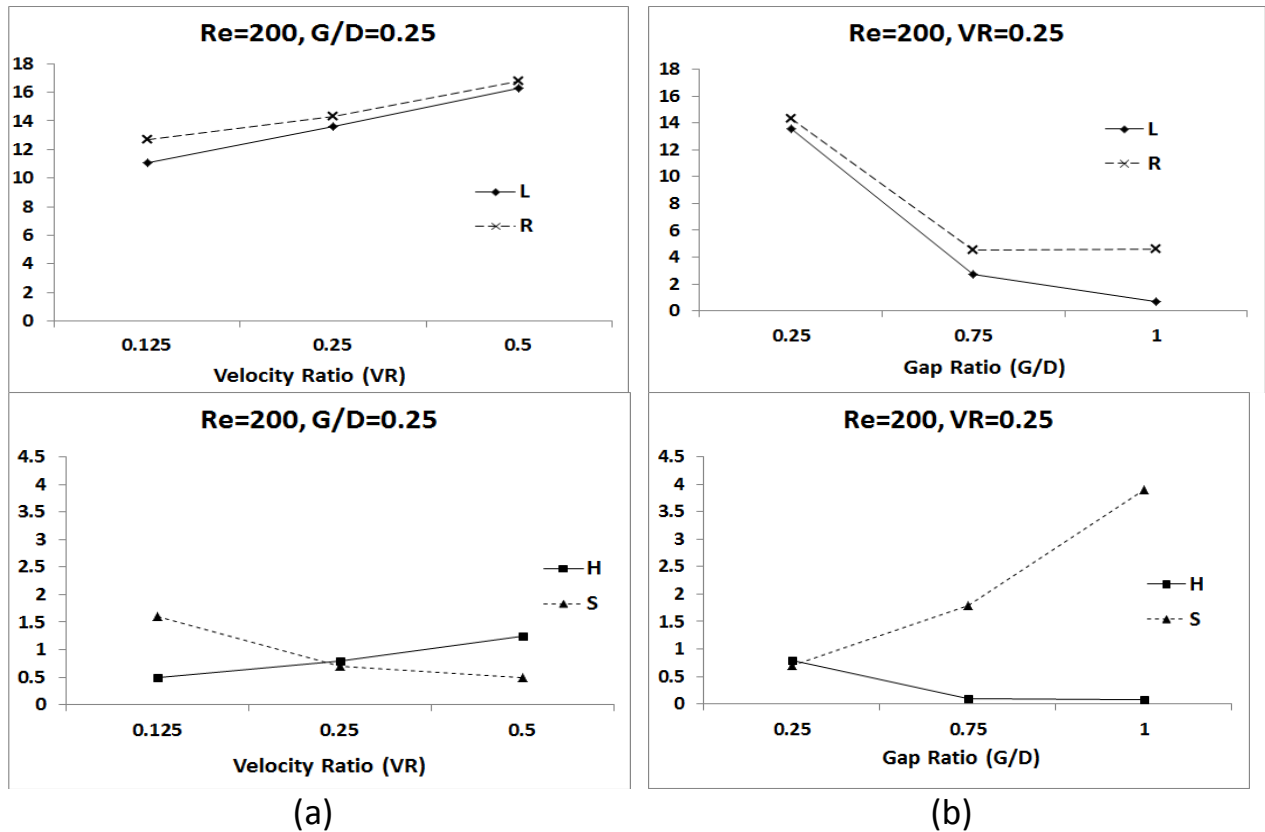


Fig. 3.15 Separation bubble properties as function of (a) Cylinder rotation speed ( $VR$ ), (b) Gap Ratio,  $G/D$  for  $Re = 200$

The effect of  $VR$  and  $G/D$  on separation bubble properties are summarized in fig. 3.15 and fig. 3.16. Dimensionless separation bubble length ( $L$ ), height ( $H$ ), distances to the separation point ( $S$ ) and reattachment point ( $R$ ) are presented as functions of  $VR$  and  $G/D$  for  $Re = 200$  and  $1,000$ . It is shown in fig. 3.15a ( $Re = 200$ ) that, for a fixed  $G/D$ , the bubble length ( $L$ ) and height ( $H$ ) value increases with the increase of  $VR$ . At the same time, the separation point ( $S$ ) moves upstream while the reattachment point ( $R$ ) moves downstream position as  $VR$  increases. Fig.

3.15b shows the effect of  $G/D$  on the properties of separation bubble at  $Re = 200$  for a fixed  $VR$ . With the increase of  $G/D$ , a reduction of bubble length ( $L$ ) and height ( $H$ ) can be observed. It also delays the separation and causes early reattachment. Similar features are observed for the cases with  $Re = 1,000$  (fig. 3.16) and is not discussed here.

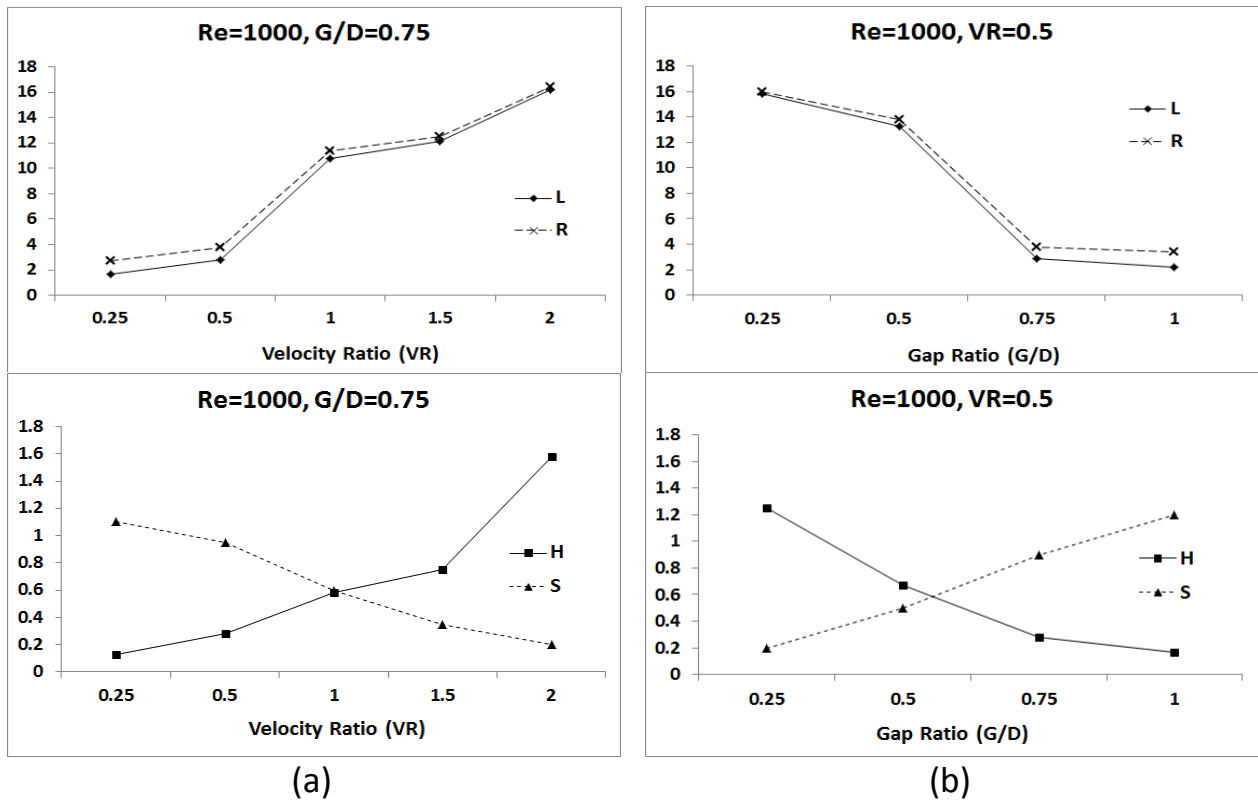


Fig. 3.16 Separation Bubble properties as function of (a) Cylinder rotation speed ( $VR$ ), (b) Gap Ratio,  $G/D$  for  $Re = 1,000$

### 3.4.2. Comparison of Separation Bubble for High $Re$ with Experimental Results

Fig. 3.17 presents the time averaged skin friction,  $C_f$  along the wall and the time-averaged streamlines for an experimental condition [20], where  $Re_D \approx 6,700$ ,  $VR = 0.75$ ,  $G/D = 0.8$ . At this condition, the experimental results show that the rotating cylinder can induce a stable separation bubble over flat plate. Flow separation, in the numerical model, is found to be at a point  $S = 1.1$  which reattaches at  $R = 2.3$ . Thus, the predicted non-dimensional bubble length,  $L = 1.2$  and the non-dimensional bubble height is estimated to be  $H = 0.12$ . The experimental

separation bubble length and height was found to be 1.24 and 0.08. Flow separates experimentally at  $S = 0.925$  and reattaches at  $R = 2.16$ . Thus, the predicted separation bubble size is found to be a close match to experimental separation bubble size. This is yet another validation of the numerical model even for high Reynolds number flows.

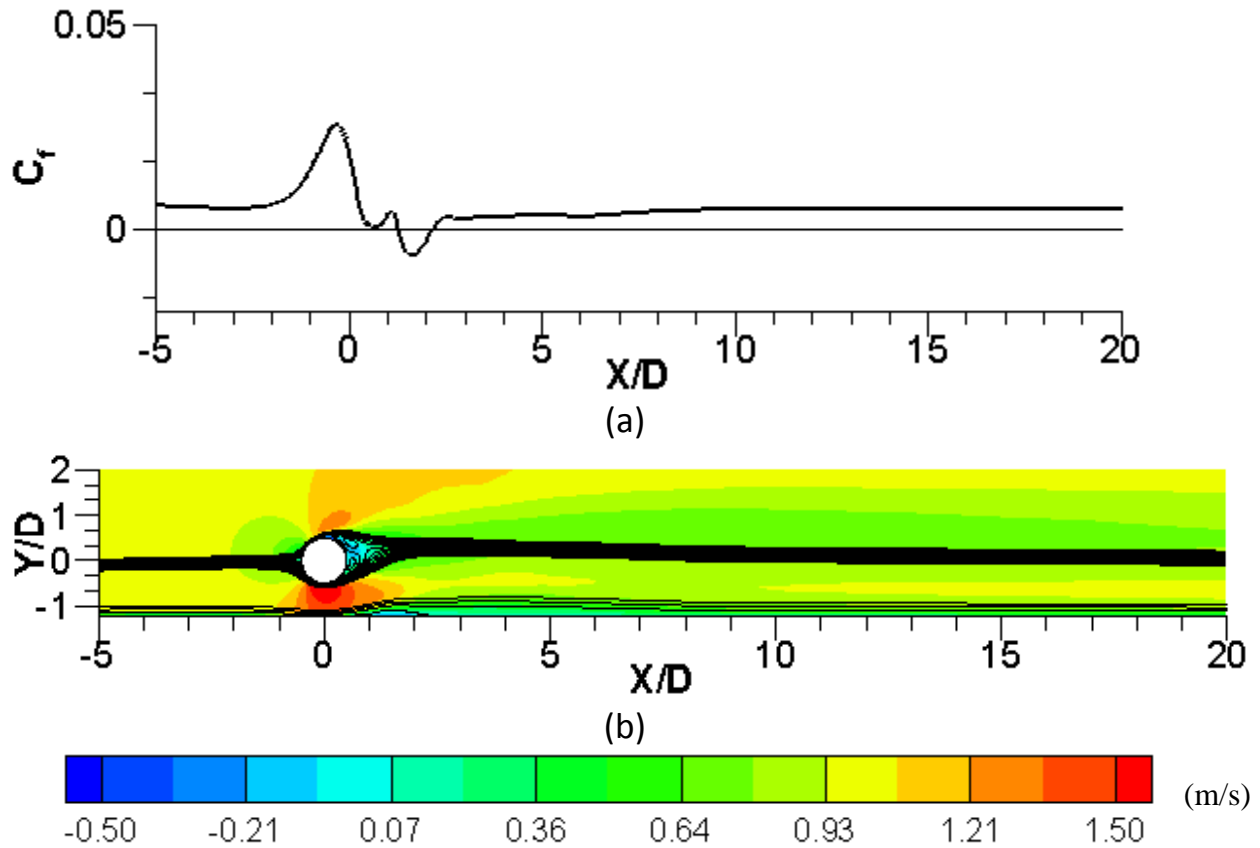


Fig. 3.17 Time-averaged (a) mean streamline  $C_f$  along wall (b). stream wise velocity contours along with selected streamlines for different cylinder gap ( $G/D$ ) at  $Re = 6,700$ ,  $G = 0.75$ ,  $VR = 0.8$

### 3.4.3. Vortex Dynamics and Wake Evolution

The dependence on  $VR$  and  $G/D$  of the vortex-shedding evolution process in the near-wake region are studied by observing the time averaged vorticity field plotted for some sample cases in figs. 3.18 and 3.19. The plots show some typical evolution patterns of the vorticity field for two different combinations of  $G/D$  and  $VR$ , in which positive and negative vorticities are represented by the solid and the dashed lines, respectively.

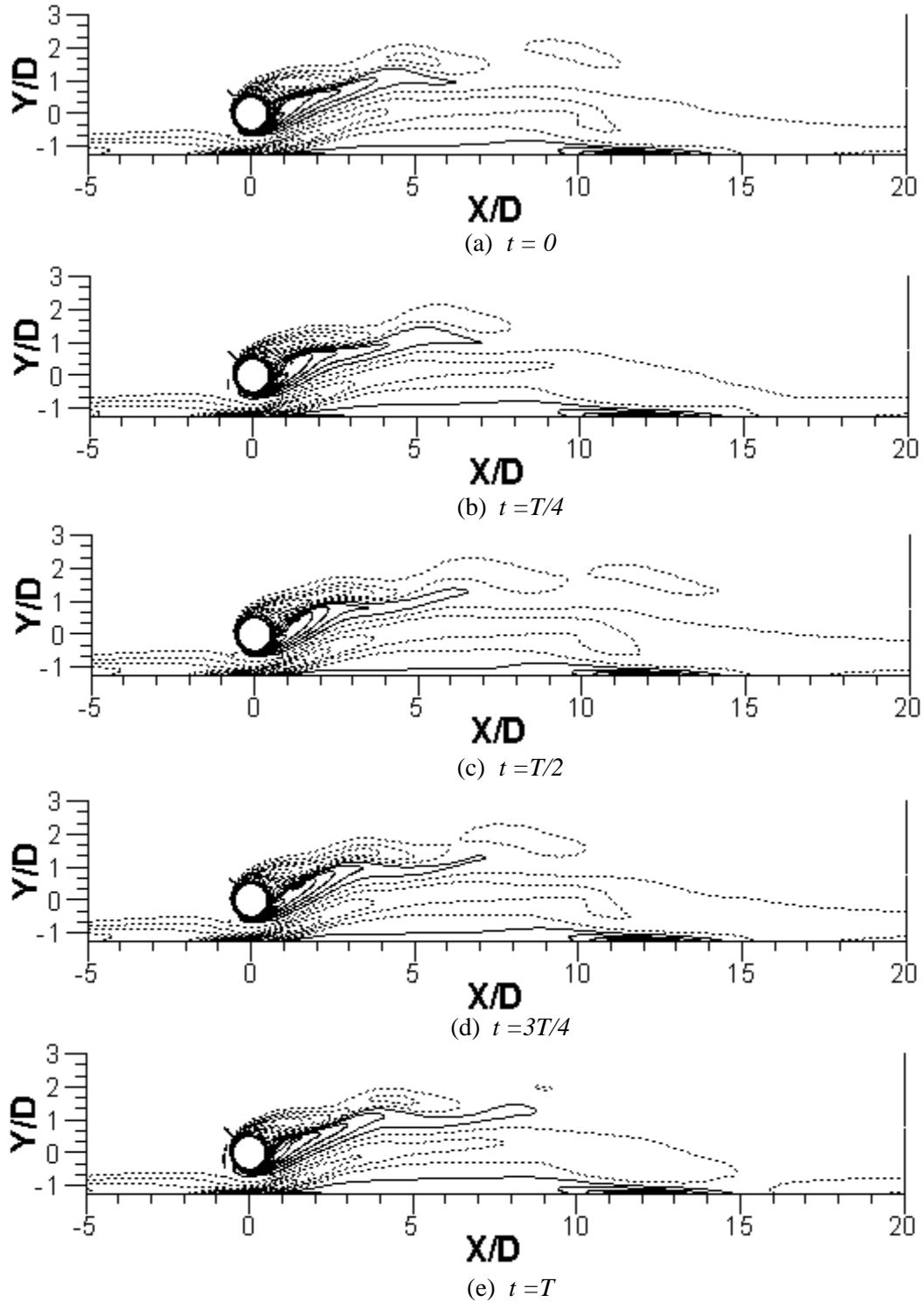


Fig. 3.18. Vorticity contours around the rotating cylinder near a flat wall during one cycle of vortex shedding for  $Re = 200$ ,  $G/D = 0.75$  and  $VR = 1$

These figures are shown between a time period ( $T$ ) of vortex shedding that has been calculated based on the assumption of Strouhal number,  $St$ , as 0.2. The Strouhal number value of

0.2 is just an approximate average value over the range of  $G/D$  and  $VR$  in the present study. A brief description of the vortex formation, interaction of the boundary layers is presented next.

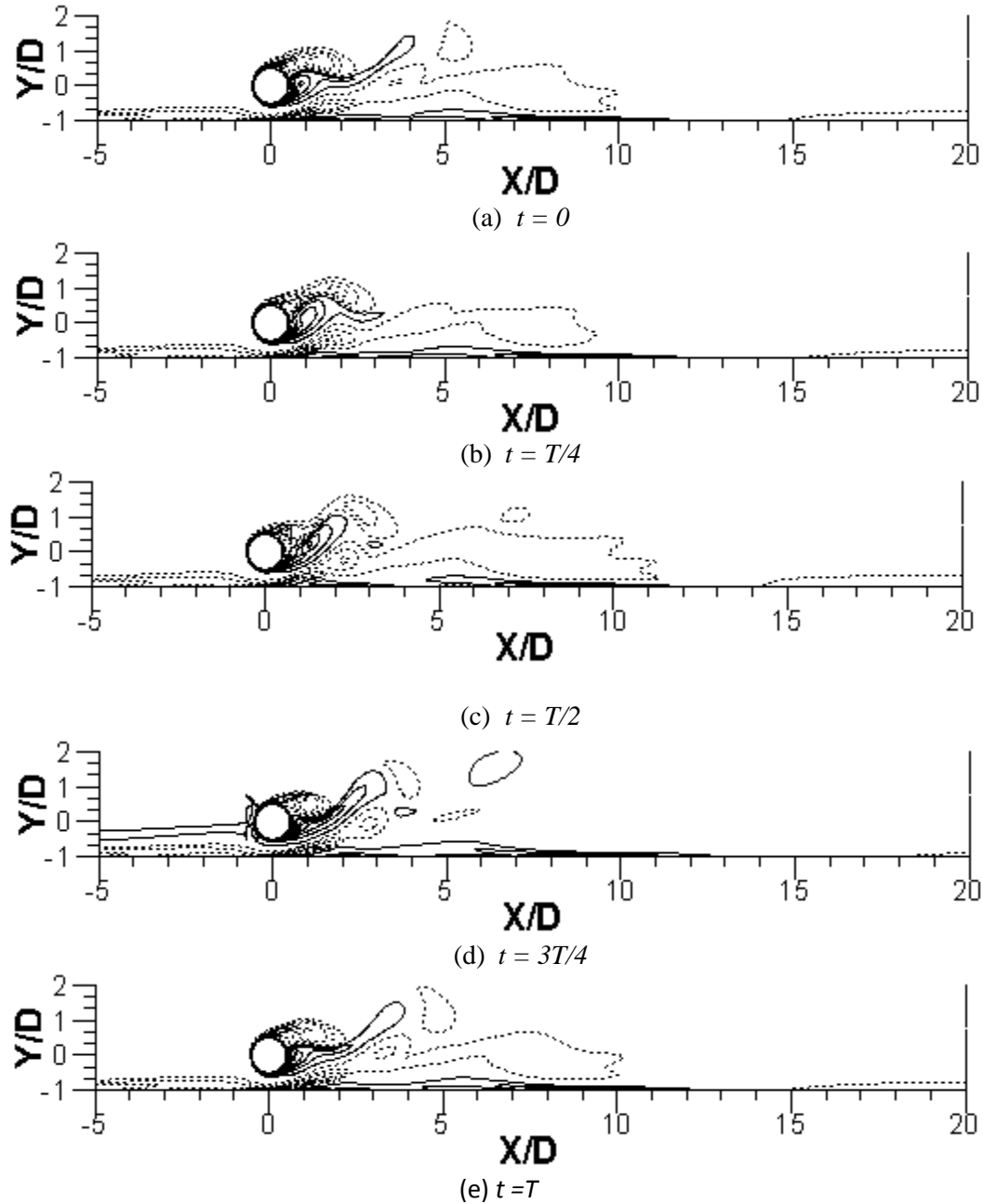


Fig. 3.19. Vorticity contours around the rotating cylinder near a flat wall during one cycle of vortex shedding for  $Re = 1,000$ ,  $G/D = 0.5$  and  $VR = 0.5$

Five different instantaneous time starting from  $t = 0$  to  $t = T$  with an increment of  $T/4$  for one cycle of vortex shedding have been presented in fig. 3.18 and 3.19 for a combination of  $G/D = 0.75$ ,  $VR = 1.0$  for  $Re = 200$  and  $G/D = 0.5$ ,  $VR = 0.5$  for  $Re = 1,000$ . Three main vortices; one

positive vortex (counterclockwise) from the lower side of the cylinder and two negative vortices (clockwise) from the upper side of the cylinder and the plane wall underneath cylinder, are noticed in these figures. The vortex, generated from the lower side of the cylinder in combination with the accelerated flow in the gap between the cylinder and the wall, is responsible for the negative vortex growth in the boundary layer on the plane wall. There is another thin region of positive vortices over the wall because of the formation of separation bubble over wall. The key characteristic of the vortex evolution is that the cylinder rotation pulls away the unsteady cylinder wake. It can be considered as a fact that rotating cylinder acts like a real vortex with a solid body rotational core (peak velocity at cylinder surface). As the rotating cylinder viscous wake is induced to move away by the cylinder rotation, the rest of the flow acts as an irrotational vortex flow [29]. The negative vortex generated at the wall is the dominating flow for the separation on the wall. The positive vortex generated from the bottom of the cylinder grows considerably in size for higher gap ratio ( $G/D = 0.75$ ).

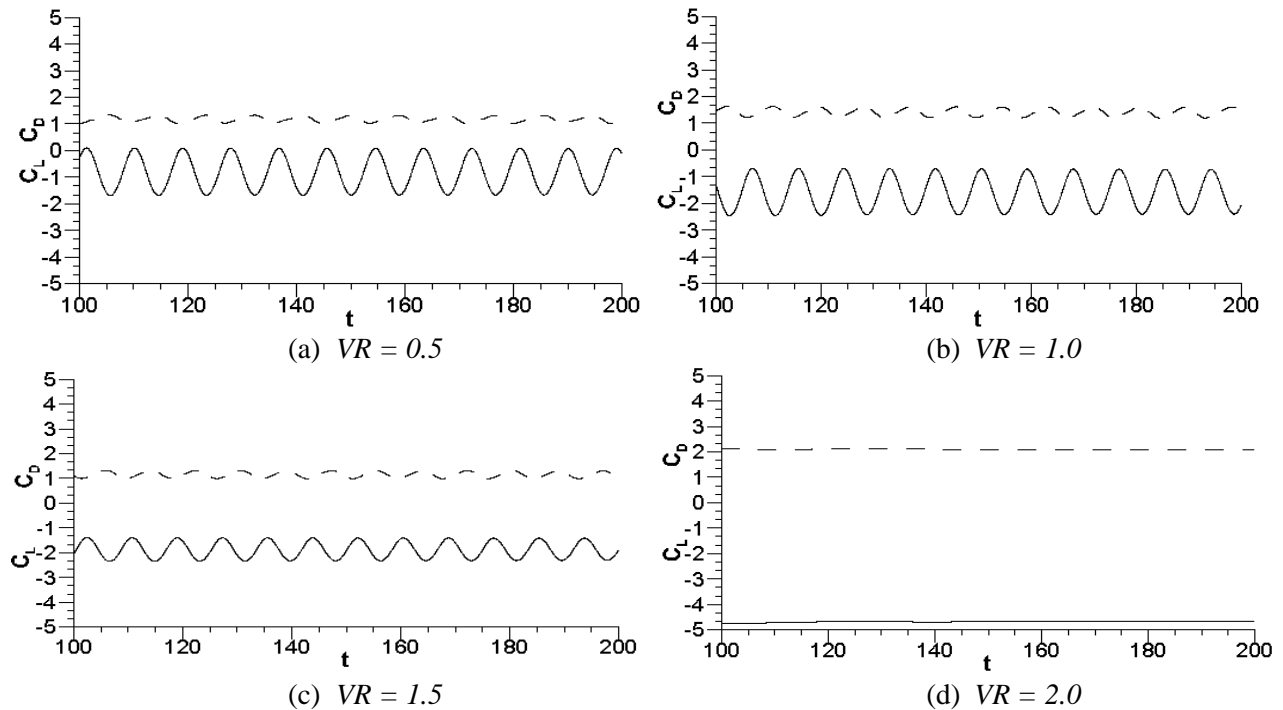


Fig. 3.20. Time history of lift and drag coefficient for  $Re = 1,000$  and  $G/D = 0.75$

### 3.4.4. The Lift and Drag Coefficients

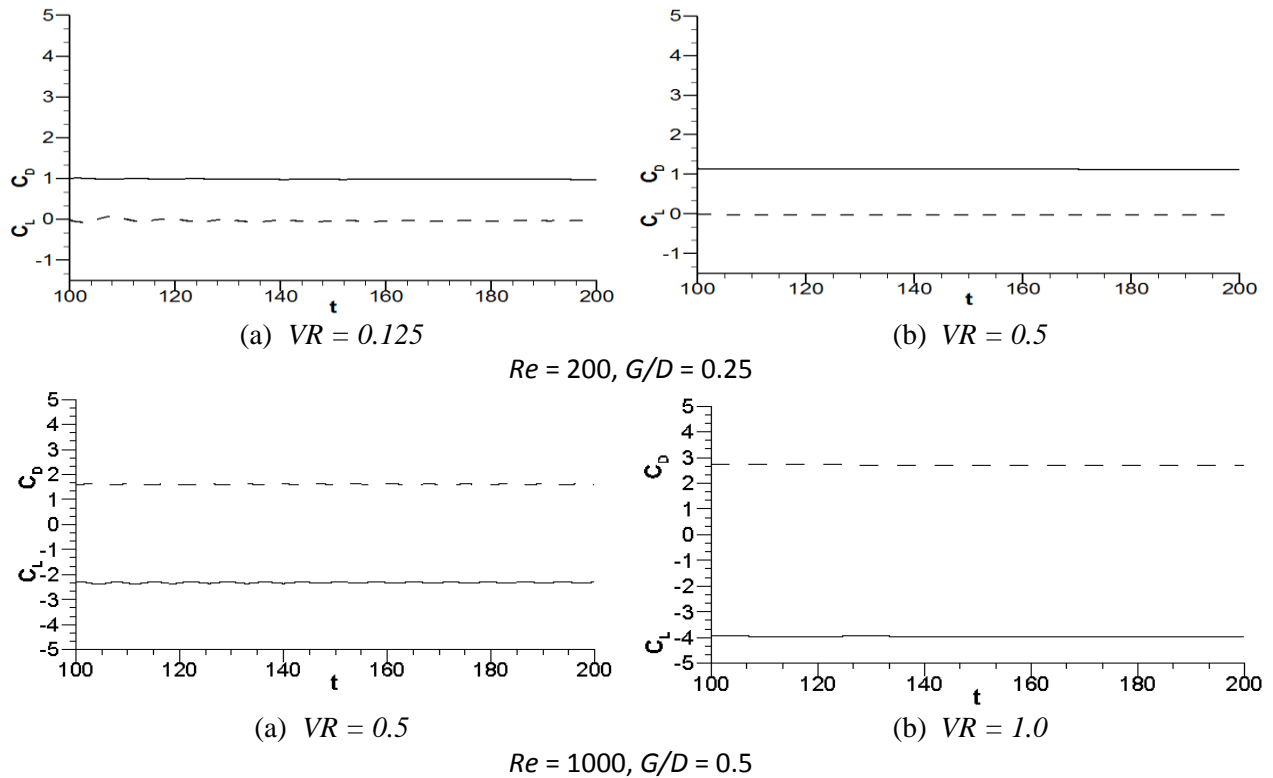


Fig. 3.21 Elimination of vortex shedding indicated by steady (time independent) variation of drag and lift coefficients for various combinations of  $Re$ ,  $G/D$ , and  $VR$ .

Fig. 3.20 and fig. 3.21 presents the time history of the lift and drag coefficients for different combination of  $Re$ ,  $G/D$ , and  $VR$ . Fig. 3.20 shows the time history of  $C_L$  and  $C_D$  for  $Re = 1,000$  and  $G/D = 0.75$  while the cylinder is rotating at different speeds. It reveals that, as  $VR$  increases from 0.5 to 1.5, the lift and drag coefficients attain a periodic variation pattern, but the amplitude decreases in magnitude. It indicates regular vortex shedding for these combinations of  $G/D$  and  $VR$ . As  $VR$  reaches to the value of 2.0 or greater, the variation of both  $C_L$  and  $C_D$  with time almost gets steady. It indicates the presence of a steady wake without any vortex shedding at this combination of cylinder gap and rotation speed. On the other hand, it can be seen from fig. 3.21 that for lower gap ratio  $G/D = 0.25$  or less) at  $Re = 200$ , the value of  $C_L$  and  $C_D$  are also almost steady for different values of  $VR$ . So if the cylinder is located very close to the wall, there

is no vortex shedding in the wake and the wake flow is stable. For  $Re = 1,000$  and  $G/D = 0.5$ , the time history of  $C_L$  and  $C_D$  exhibits irregular behavior and as  $VR$  increases to 1.0, both  $C_L$  and  $C_D$  remains almost constant. So both the gap ratio and cylinder rotational speed has a strong influence on vortex shedding behavior which is manifested in the time variation patterns of the lift and drag coefficients.

### 3.5. Conclusions

A numerical study of a novel system of generating adverse pressure gradient on a flat wall by using a rotating cylinder in the proximity of the wall is presented in this paper. It has been demonstrated to be an effective method to generate various strengths of adverse pressure gradient as a function of the cylinder rotation speed ( $VR$ ) and the cylinder to diameter gap ratio ( $G/D$ ) for a range of Reynolds number,  $200 \leq Re_D \leq 6,700$ . A parametric study is conducted to see the effect of  $VR$  and  $G/D$  on the size and extent of the resulting separation bubble due to the generated adverse pressure gradient. The time-averaged flow features and vortex dynamics reveal that there is a critical gap ratio below which the plane wall boundary layer separation occurs both upstream and downstream of the cylinder. If cylinder moves close to wall at a fixed rotation speed or the cylinder rotation speed increases at a fixed cylinder gap, the gap flow experiences higher acceleration and the pressure is lowered. As a result, the separation point moves upstream because of this accelerated gap flow and the separation bubble also grows larger in size.

## References

1. Bearman, P.W., Zdravkovich, M.M., (1978). Flow around a circular cylinder near a plane boundary. *Journal of Fluid Mechanics* 89,33–47.
2. Zdravkovich, M. M. (1985). Forces on a circular cylinder near a plane wall. *Applied Ocean Research*, 7(4), 197-201.
3. Zdravkovich, M. M. (1997). Flow around circular cylinders, volume 1: fundamentals. *Oxford University Press*, Oxford, 19, 185.
4. Lei, C., Cheng, L., Armfield, S. W., & Kavanagh, K. (2000). Vortex shedding suppression for flow over a circular cylinder near a plane boundary. *Ocean Engineering*, 27(10), 1109-1127.
5. Price, S. J., Sumner, D., Smith, J. G., Leong, K., & Paidoussis, M. P. (2002). Flow visualization around a circular cylinder near to a plane wall. *Journal of Fluids and Structures*, 16(2), 175-191.
6. Sengupta, T. K., De, S., & Sarkar, S. (2003). Vortex-induced instability of an incompressible wall-bounded shear layer. *Journal of Fluid Mechanics*, 493, 277-286.
7. Dipankar, A., & Sengupta, T. K. (2005). Flow past a circular cylinder in the vicinity of a plane wall. *Journal of Fluids and Structures*, 20(3), 403-423.
8. Wang, X. K., & Tan, S. K. (2008). Near-wake flow characteristics of a circular cylinder close to a wall. *Journal of Fluids and Structures*, 24(5), 605-627.
9. Zovatto, L., & Pedrizzetti, G. (2001). Flow about a circular cylinder between parallel walls. *Journal of Fluid Mechanics*, 440(1), 1-25.
10. Huang, W. X., & Sung, H. J. (2007). Vortex shedding from a circular cylinder near a moving wall. *Journal of Fluids and Structures*, 23(7), 1064-1076.
11. Modi, V. J., Mokhtarian, F., Fernando, M. S. U. K., & Yokomizo, T. (1991). Moving surface boundary-layer control as applied to two-dimensional airfoils. *Journal of Aircraft*, 28(2), 104-112.
12. Modi, V. J. (1997). Moving surface boundary-layer control: A review. *Journal of Fluids and Structures*, 11(6), 627-663.
13. Mittal, S., & Kumar, B. (2003). Flow past a rotating cylinder. *Journal of Fluid Mechanics*, 476(4), 303-334.

14. Rao, A., Stewart, B. E., Thompson, M. C., Leweke, T., & Hourigan, K. (2011). Flows past rotating cylinders next to a wall. *Journal of Fluids and Structures*, 27(5), 668-679.
15. Cheng, M., & Luo, L. S. (2007). Characteristics of two-dimensional flow around a rotating circular cylinder near a plane wall. *Physics of Fluids*, 19, 063601.
16. Simpson, R. L. (1989). Turbulent boundary-layer separation. *Annual Review of Fluid Mechanics*, 21(1), 205-232.
17. Lang, M., Rist, U., & Wagner, S. (2004). Investigations on controlled transition development in a laminar separation bubble by means of LDA and PIV. *Experiments in Fluids*, 36(1), 43-52.
18. Simpson, R. L., Chew, Y. T., & Shivaprasad, B. G. (1981). The Structure of a Separating Turbulent Boundary Layer. Part 1. Mean Flow and Reynolds Stresses. *Journal of Fluid Mechanics*, 113, 23-51.
19. Simpson, R. L., Chew, Y. T., & Shivaprasad, B. G. (1981). The structure of a separating turbulent boundary layer. Part 2. Higher-order turbulence results. *Journal of Fluid Mechanics*, 113(1), 53-73.
20. Afroz, F., Lang, A., Jones, E., & Bradshaw, M. (2012). Laminar separation bubble formation using a circular cylinder rotating adjacent to a flat plate. *Bulletin of the American Physical Society*, 57.
21. Afroz, F., Lang, A., & Jones, E. Using a Rotating Cylinder to Induce a Laminar Separation Bubble over a Flat Plate, *European Journal of Mechanics B/Fluids* (under review)
22. Afroz, F., Lang, A., & Jones, E. Experimental Study of Turbulent Boundary Layer Separation over a Flat Plate Induced by a Rotating Cylinder, *European Journal of Mechanics B/Fluids* (under review)
23. Badr, H. M., & Dennis, S. C. R. (1985). Time-dependent viscous flow past an impulsively started rotating and translating circular cylinder. *Journal of Fluid Mechanics*, 158(1), 447-488.
24. Badr, H. M., Coutanceau, M., Dennis, S. C. R., & Menard, C. (1990). Unsteady flow past a rotating circular cylinder at Reynolds numbers 103 and 104. *Journal of Fluid Mechanics*, 220, 459-484.
25. Pearlstein, A. J. (1993). Development of the wake behind a circular cylinder impulsively started into rotatory and rectilinear motion. *Journal of Fluid Mechanics*, 253, 449-484.
26. ANSYS FLUENT, Computational Fluid Dynamics Code Version 13, ANSYS Inc., <http://www.ansys.com>.

27. Sarkar, S., & Sarkar, S. (2010). Vortex dynamics of a cylinder wake in proximity to a wall. *Journal of Fluids and Structures*, 26(1), 19-40.
28. Choi, J. H., & Lee, S. J. (2000). Ground effect of flow around an elliptic cylinder in a turbulent boundary layer. *Journal of Fluids and Structures*, 14(5), 697-709.
29. Kundu, P. (1990). Fluid Mechanics, *Academic Press, San Diego, CA*.

## CHAPTER FOUR

### \*EXPERIMENTAL STUDY OF TURBULENT BOUNDARY LAYER

#### SEPARATION OVER A FLAT PLATE INDUCED BY A ROTATING CYLINDER

Farhana Afroz, Amy Lang, Emily Jones

Department of Aerospace Engineering and Mechanics, University of Alabama

#### Abstract

The physical behavior of a turbulent boundary layer (TBL) induced to separate over a flat plate was examined. An innovative and easy technique using a rotating cylinder system has been implemented in a water tunnel experiment to generate an adverse pressure gradient (APG). The turbulent separation over the flat plate was induced by varying the strength of the APG through adjustment in the rotation speed and location of the cylinder. The mean detachment locations of TBL separation are determined by three different definitions: (1) location predicted by Stratford's turbulent separation criteria, (2) backflow coefficient ( $\chi$ ) = 50%, and (3) location of the start of a negative mean skin friction coefficient ( $C_f$ ); all are in good agreement. Time-resolved digital particle image velocimetry (TR-DPIV) was used to explore the unsteady, turbulent separation bubble in a 2-D plane aligned with the flow and perpendicular to the plate. The time-averaged velocity profile obtained from this DPIV investigation revealed that the nature and extent of the separation region depends on the rotation speed and location of cylinder.

Keywords: Rotating Cylinder, Adverse Pressure Gradient, Turbulent Boundary Layer Separation, Particle Image Velocimetry.

*\*European Journal of Mechanics – B/Fluids (Under Review)*

## 4.1 Introduction

Understanding the formation of turbulent boundary layer separation is very important because of its occurrence in various applications such as lifting surfaces, turbine blades, diffusers, etc. Although there are many numerical and experimental works on separated turbulent flow, the process leading to separation and the ability to completely control flow separation has not been fully understood or achieved. Turbulent boundary layer separation is highly unsteady, and it does not have a single stationary separation point like laminar separation. Quantitative definitions on the detachment state near the wall were proposed based on the fraction of time flow moves against the flow direction [1, 2]. The separation points typically defined are incipient detachment (ID), which occurs where an instantaneous backflow 1% of the time ( $\chi = 0.01$ ) is measured; intermittent transitory detachment (ITD), which occurs for an instantaneous backflow 20% of the time ( $\chi = 0.20$ ); transitory detachment (TD), which occurs for an instantaneous backflow 50% of the time ( $\chi = 0.50$ ); and detachment (D), which occurs where the time-averaged wall shearing stress ( $\tau_w$ ) equals zero. Available data suggests that TD matches well with point D very well.

Turbulent boundary layer (TBL) separation is induced by the presence of an adverse pressure gradient (APG), surface curvature, or a combination of both. To eliminate the effect of surface curvature on TBL separation, research must be carried out where only an APG is present over a flat surface; to date, few experimental studies have been carried out of this nature, and hence, the focus of the work presented here.

The structure of turbulent flow over curved surfaces was summarized by Simpson [3]. He concluded that convex curvature is responsible for lower entrainment, less mixing, and lower Reynolds stress, while a concave curvature oppositely results in greater entrainment, mixing, and

turbulent shearing stresses. When the surface curvature changes quickly, the outer-region streamlines do not curve rapidly. The lag of turbulent flow in responding quickly to a diverging wall was due to the inability of large energy-containing eddies to rapidly respond to the change in boundary condition.

Recent experimental investigations looked at the effect of both the adverse pressure gradient generated by flow expansion and the strong convex curvature on a turbulent flow over a convex-walled ramp [4–6]. The turbulent flow separated on the ramp and reattached at a short distance downstream of the ramp trailing edge, thereby forming a small separation bubble. Investigation revealed one key feature: the inner layer recovered relatively quickly in the redeveloping region while the outer layer recovery was slowed down by the large eddies in the separation region.

A numerical study was also conducted for flow over a thick half plate with a rounded front edge to study the effect of curvature on the separation bubble while keeping the Reynolds number based on the height of the half plate constant [7, 8]. The curvature effects deeply influenced the separation bubble dynamics. Separation angle as well as kinetic energy was observed to increase for high curvature. Receptivity of the flow with respect to upstream conditions was also found to be decreased for high curvature.

The effect of convex and concave surface curvature on boundary layer separation showed an asymmetric response [9]. Results from this study showed that the boundary layer recovering from the sequence of concave to convex curvature had a sustained lower skin friction level than the sequence of convex to concave curvature. More investigation over a bump was carried out to see the detailed response of a turbulent boundary layer to a series of perturbations [10, 11]. Boundary layers in these studies experienced a short concave region, a longer convex region,

another short concave region, and then finally followed a flat plate. In other words, the flow was subjected to stream wise pressure gradients: first mild adverse pressure, strong favorable, strong adverse, and eventually mild favorable. Results revealed that the response of a turbulent flow over a series of external perturbations could not be considered a simple summation of the responses from individual perturbations.

The pioneering work of turbulent boundary layer separation was carried out by Simpson et al. [1, 2], where an adverse pressure gradient was imposed and varied by an adjustable upper wall. Patrick [12] later experimentally studied the separation and reattachment of a large-scale, two-dimensional turbulent boundary layer at a low subsonic speed on a flat plate. The results agreed with the findings of Simpson et al. [1, 2] and also revealed low-frequency nonperiodic flapping in the reattachment region. Another study looked at a completely separated separation bubble and an attached turbulent boundary layer over a flat plate under adverse pressure gradient (which was imposed by an adjustable top wall) was studied with help of DPIV. To understand the two-dimensional structure of TBL separation, DPIV proved to give a good resolution of the velocity field for this setup [13].

Like experiments, there are also only a limited number of numerical studies on turbulent separated flow. Direct numerical simulation was performed by Coleman and Spalart [14] for a very weakly separated turbulent boundary layer. An extensive numerical study was later carried out by Na and Moin [15]. An adverse pressure gradient was imposed and varied by applying a suction and blowing velocity distribution through the upper boundary of the computational domain. The study showed that the locations of maximum turbulence intensities and Reynolds shear stress occurred in the middle of the shear layer. Reynolds shear stresses and their gradients were found to be larger away from the wall in the detached flow region, and thus, the largest

pressure fluctuations are in the middle of the shear layer. Direct numerical simulation was also performed for a fully turbulent flow with separation induced by a stream wise adverse pressure gradient [16]. It was discovered that increased Reynolds stresses played a prominent role in controlling the structure and geometry of the separation bubble. Another numerical study using strong adverse pressure gradient conditions showed that the flow characteristics near the wall were mainly dependent on local parameters, and thus not strongly dependent on the history of the boundary layer [17].

Previous research clearly shows that the effect of surface curvature and the presence of an adverse pressure gradient on turbulent separation is not just a summation of these separate effects. In order to eliminate the curvature effect and understand turbulent boundary layer separation over a flat plate induced by adverse pressure gradient, additional research must be conducted where a wide variation in the induced adverse pressure gradient is possible.

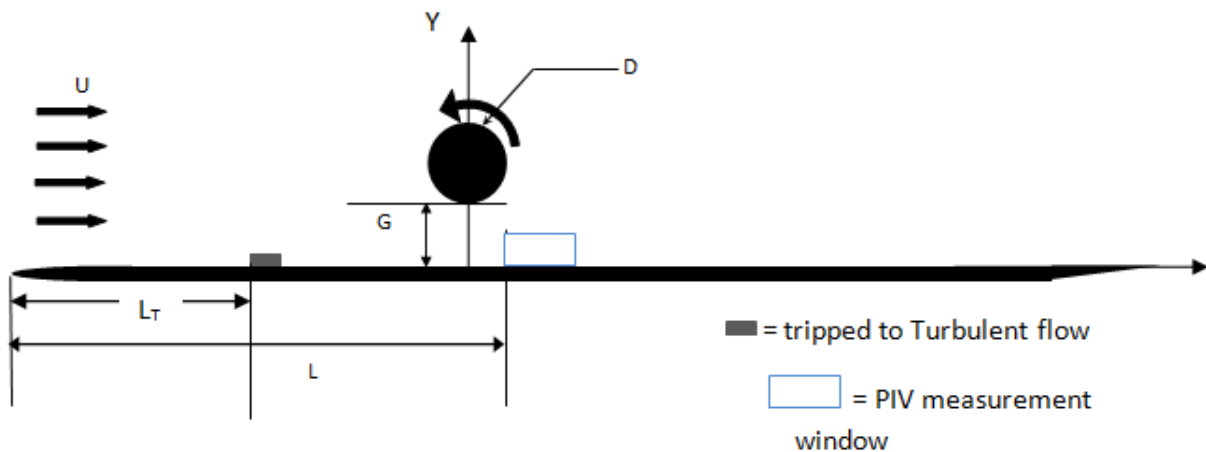


Figure 4.1: Using a rotating cylinder to generate APG to induce a separate turbulent boundary layer over a flat plate

The use of rotating a circular cylinder to induce a widely varying magnitude of adverse pressure gradient has been proven to be a simple technique to induce the formation of a laminar

separation bubble over a flat plate [18]. The strength of the adverse pressure gradient was varied by adjusting the cylinder gap to diameter ratio ( $G/D$ ) and cylinder rotation speed. In the present experiment, the same technique was applied to induce turbulent boundary layer separation over a flat plate (fig. 4.1). The effect of cylinder location,  $G/D$  and dimensionless velocity ratio,  $VR$ , on the extent and nature of TBL separation is documented in this study. Turbulent intensities and Reynolds stresses inside the turbulent separation region was also analyzed to understand the near-wall behavior of TBL separation.

## 4.2 Theoretical Inviscid Model of Turbulent Separation

An inviscid theoretical model for flow about a rotating cylinder located near a wall consists of the superposition of a free stream flow, doublet and vortices. The method of images produced a symmetry line between two identical rotating cylinders to form the plane wall. This inviscid model is used to quantify the strength of pressure gradient induced along the wall for a different cylinder rotation speed,  $VR$  and cylinder location, and  $G/D$ . This same model was used by the authors to predict the strength of the induced pressure gradient for inducing a similar study to look at laminar separation over a flat plate [18]. It should be noted that this model works well because of the fact that the rotating cylinder viscous wake is induced to move up and away from the measurement region, thereby not affecting the measurements. The remaining viscous flow induced by the cylinder rotation can be shown to be that of an irrotational vortex [19]. The tunnel flow speed used for the experiments,  $U = 0.25$  m/s, was used here as well as for the theoretical calculations.

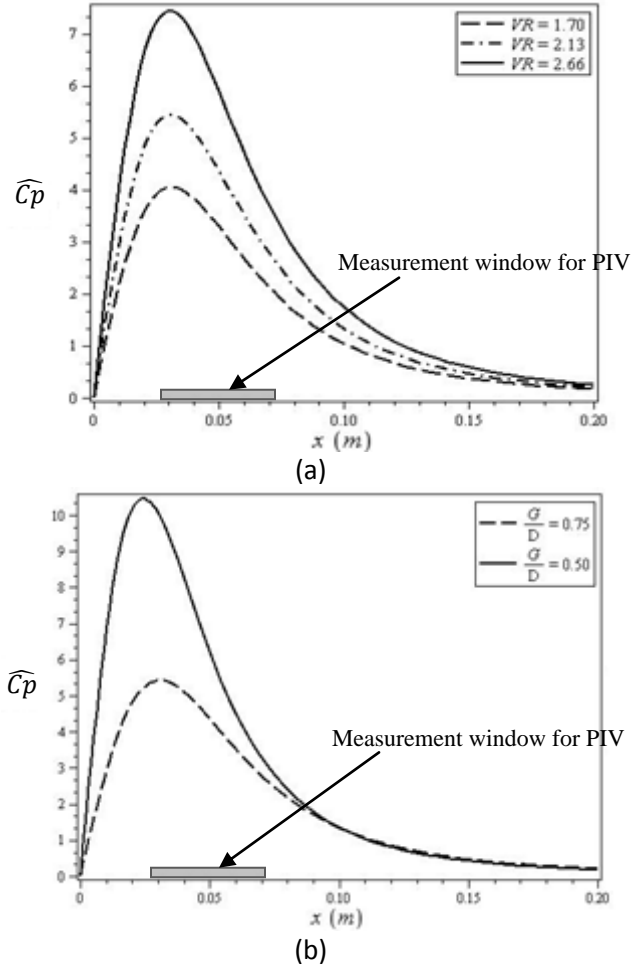
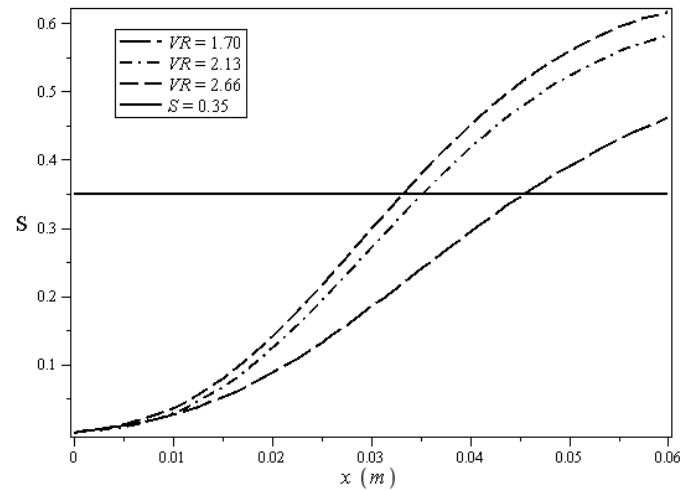


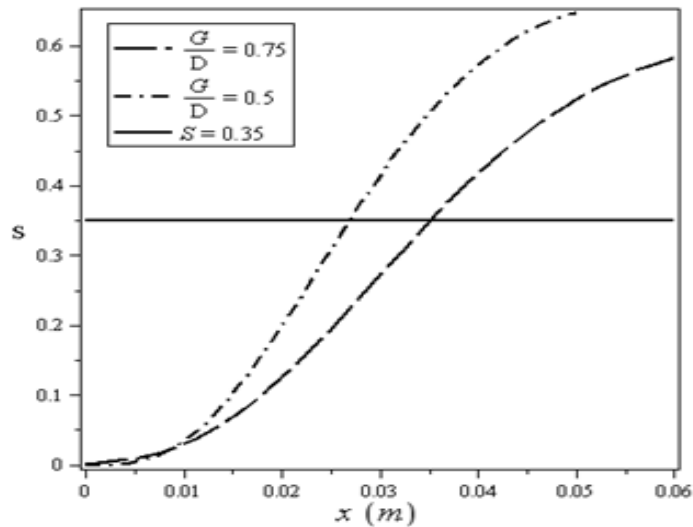
Figure 4.2: Theoretical pressure coefficient gradient for reverse-doublet-like cylinder rotation along the wall for (a) different velocity Ratio, VR at  $\frac{G}{D} = 0.75$ , (b) at different  $\frac{G}{D}$  for a fixed VR = 2.13

Figure 4.2 shows the impact of changing VR and G/D on the gradient of the pressure coefficient  $\left(\frac{\partial C_p}{\partial x}\right)$ . Pressure gradient variation up to only  $x = 0.2$  m has been presented here, as beyond this point, any variation in pressure gradient was insignificant. As predicted, an increase of dimensionless cylinder rotation speed also resulted in an increase in the pressure gradient (fig. 4.2a). This calculation predicts the earlier separation from the wall as well as the increase in rotation speed. These same trends are true for the decrease in gap height (fig. 4.2b).

The measurement location for the experiments was chosen based on these calculations (highlighted from  $x = 0.026$  m to  $x = 0.07$  m). It covers the area where the boundary layer is subjected to an extreme adverse pressure gradient (APG) and also includes the area where APG decreases. The same parametric values for VR and G/D were used in both experimental and theoretical cases for direct comparison.



(a)



(b)

Figure 4.3: Stratford's criteria for predicting turbulent separation point for (a) different velocity ratio, VR at  $\frac{G}{D} = 0.75$ , (b) at different  $\frac{G}{D}$  for a fixed VR = 2.13

Fig. 4.3 presents the prediction of the separation point as calculated using Stratford's turbulent separation criteria [20].

This separation point is defined as

$$C'_p \sqrt{\frac{dC'_p}{dx}} = \left(\frac{Re}{10^6}\right)^{0.1} S \quad (i)$$

This formula is only valid as long as  $C'_p < \frac{4}{7}$

$C'_p$  is the canonical pressure distribution defined by

$$C'_p = 1 - \left(\frac{u}{u_{max}}\right)^2 \quad (ii)$$

$u$  is the local velocity and is  $u_{max}$  the maximum velocity at the start of the pressure recovery.

The constant  $S$  is 0.35 when  $\frac{d^2P}{dx^2} < 0$  (concave recovery)

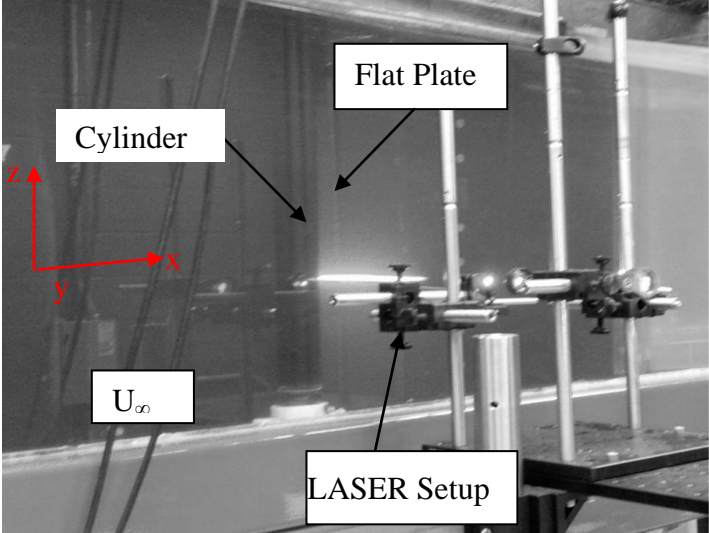
and 0.39 when  $\frac{d^2P}{dx^2} > 0$  (convex recovery). Here the separation point prediction was done by matching with the line,  $S = 0.35$ .

## 4.3 Experimental Setup and Procedure

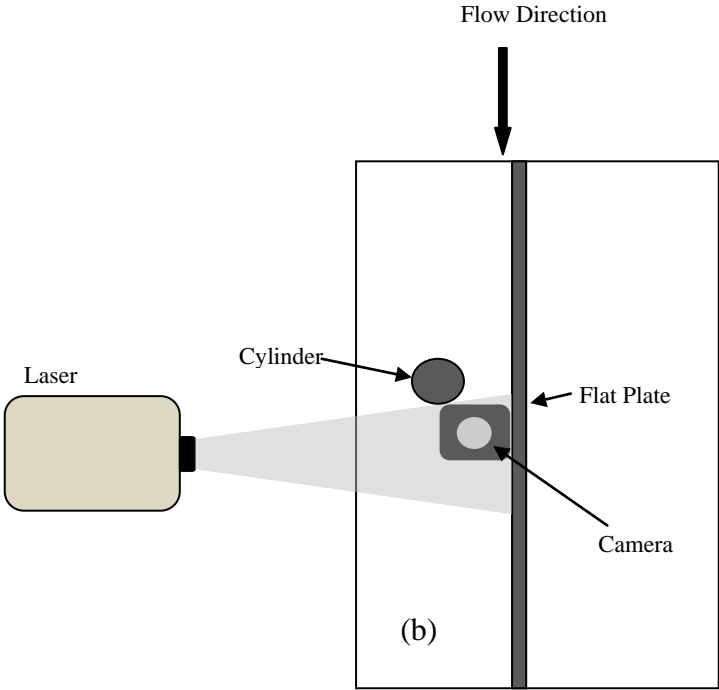
### 4.3.1 Description of Experimental Setup

All the experiments were conducted in the water tunnel facility located at the University of Alabama, manufactured by Rolling Hills Research Corporation. It has a test section size of 38 cm wide by 76 cm tall by 275 cm long. A flat plate model, made out of black Plexiglas, which has the dimensions of 45.72 cm long and 60.96 cm wide, was mounted vertically in the test section. Attached to the front of the flat plate, there is a front plate with an elliptical nose (91.44 cm in length); the flat plate model was followed by a trailing edge flap for controlling the oncoming streamline. This flap was adjusted based on flow speed and blockage to prevent the formation of a separation bubble near the leading edge. Axes used to display the orientation of

the model are labeled as follows:  $x$  is positive downstream flow direction, and  $y$  is positive upward from the plate (fig. 4.4a), and the top schematic view gives a clear picture of the location of various components with respect to the flow direction.



(a)



(b)

Figure 4.4: Experimental setup in water tunnel (a) different components of experimental setup (b) schematic diagram of arrangement of components

A PVC cylinder (diameter,  $D = 5.1$  cm) was placed at a distance of  $L = 100$  cm ( $\approx 20D$ ) downstream from the leading edge of the plate and spanned the total width (45.72 cm) of the plate (fig. 4.1). The flow was tripped to be turbulent at a distance,  $L_T = 50$  cm ( $\approx 10D$ ). Flow visualization was conducted for a constant water tunnel speed  $U = 0.25$  m/s, which gives a Reynolds number for the boundary layer based on distance from the leading edge of  $Re_x \approx 2.46 \times 10^5$ . The parametric study was conducted by varying both the dimensionless cylinder  $VR$  and  $G/D$  for varying the strength of the APG. A time-resolved DPIV system was used to identify the corresponding location of the induced TBL separation. It also documented the effect of varying APG on the size and extent of TBL separation.

#### 4.3.2 Data Acquisition and Analysis Technique

To carry out the digital particle image velocimetry (DPIV) measurements, the flow was seeded with  $14 \mu\text{m}$  silver-coated hollow glass spheres and then illuminated by a laser sheet generated by a Quantronix Falcon 20 m J Nd:YLF laser. The maximum power output of this laser is 20 watts, and it has a beam wavelength of 532 nm, 7 to 30 amps current output range, and 0.1 to 1.0 kHz frequency range. Pulsing of the laser and image acquisition was synchronized with the help of LabVIEW software. Insight3G DPIV software was used to analyze the acquired images and obtain the velocity vector field and other unsteady properties of turbulent separation. The size of each measurement window for image acquisition was  $4.5 \times 2.25$  cm, and images were captured by a Basler A504K high-speed camera at a rate of 1,000 frames per second.

A total of 9,600 images (9.6 sec) for each rotation speed were captured at  $1280 \times 512$  pixels and then analyzed to obtain both instantaneous and averaged statistics of the flow field. The images were captured 2.6 cm downstream of the cylinder center as identified in fig. 4.2. The measurement area was divided into small interrogation windows. The interrogation window size

started with  $64 \times 32$  pixels and reduced to  $16 \times 8$  pixels for increased data resolution. A minimum intensity image generator was used to determine the background noise common to all of the images, and this noise was subtracted from each image to increase the accuracy of the vector calculations. During processing, Insight 3G software utilized a Recursive Nyquist Grid, FFT correlation engine, and Gaussian peak engine, while post processing filtering was performed to eliminate any bad vectors due to localized insufficient seeding. The error associated with the DPIV technique is difficult to compute as it is primarily due to insufficient data (poor seeding density or image quality) [21, 22]. In this study, care has been taken to ensure that adequate seeding density has been maintained during acquisition of the data. Thus, an acceptable error estimate of 5% in velocity measurements and 10% in vorticity is assumed [22, 23]. The pixel/cm calibration for these data sets was 37.8 microns/pixel. Combining the error for tilting of the ruler and processing grid error, the total error for each velocity vector was kept below 5%.

## 4.4 Results and Discussion

### 4.4.1 Turbulent Base Flow

Since the local  $Re$  of the boundary layer within the measurement region was below that where natural transition occurs ( $Re_x < 5 \times 10^5$ ), the flow was tripped ( $x \approx 10D$ ) downstream from the leading edge by placing a thin plate (10 mm in height and 25 mm in width), which spanned the whole width. Reynolds number based on trip height was 2,500, which met Schlichting's [24] criterion, where Reynolds number needs to be at least 900 if turbulence is to be induced. For the steady state turbulence boundary layer over a flat plate, according to Prandtl [25], the one-seventh power law is a good approximation for the velocity profile up to the Reynolds number,  $Re = 10^5$ , based on the distance from the leading edge of the plate. The turbulent boundary layer

was first studied to ensure the development of fully turbulent flow after which the turbulent flow was subjected to the APG by placing the cylinder in the test section. In fig. 4.5, the velocity profile for  $U = 0.25$  m/s at  $Re_x \approx 2.5 \times 10^5$  is compared with the theoretical one-seventh power law; the experimental velocity profile gave a good agreement. A theoretical turbulent boundary layer thickness as it enters the measurement region is calculated at about 31 mm.

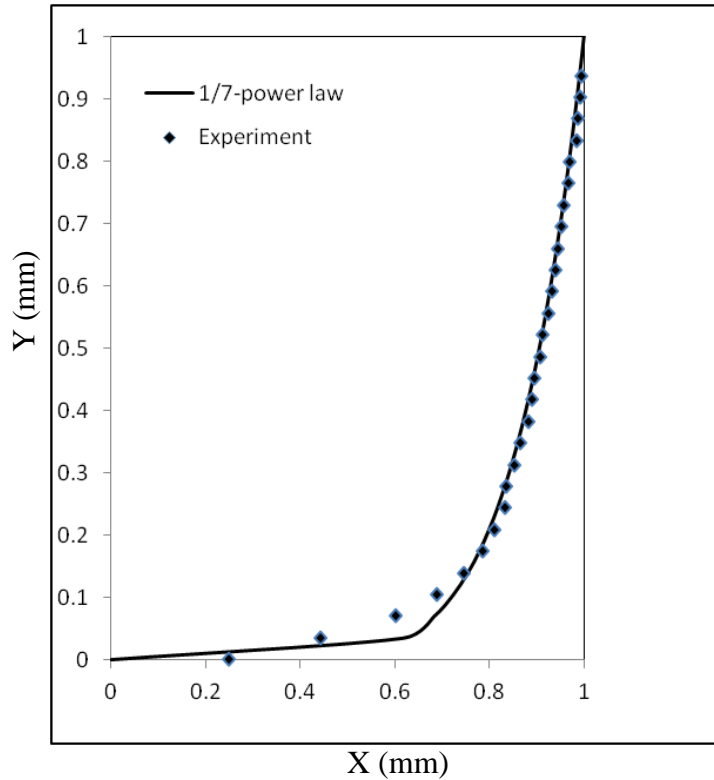
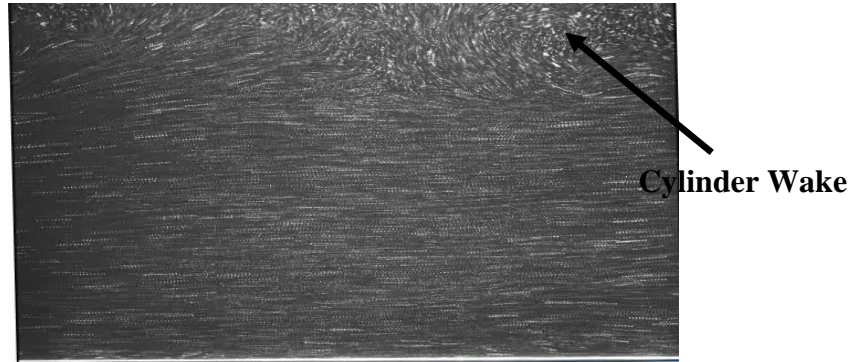
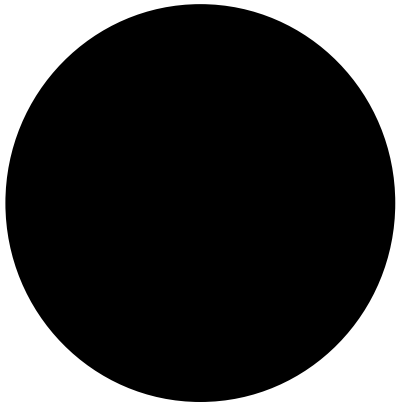


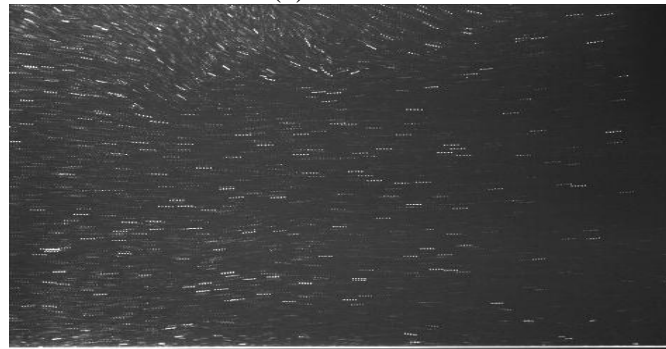
Figure 4.5: Experimental and theoretical turbulent velocity profile without any pressure gradient for  $Re_x = 2.5 \times 10^5$

#### 4.4.2 Vorticity Field in Flat Plate Boundary Layer

The unsteady cylinder wake was observed to be carried up and away from the measurement region, so it did not interfere with the flow field as shown in the instantaneous streak flow visualization in fig. 4.6. This preliminary study was carried out to visualize the flow for the whole gap between the cylinder and the plate.



(a) VR = 0



(b) VR = 1.7



(c) VR = 2.66

Figure 4.6: Streak flow visualization for different VRs

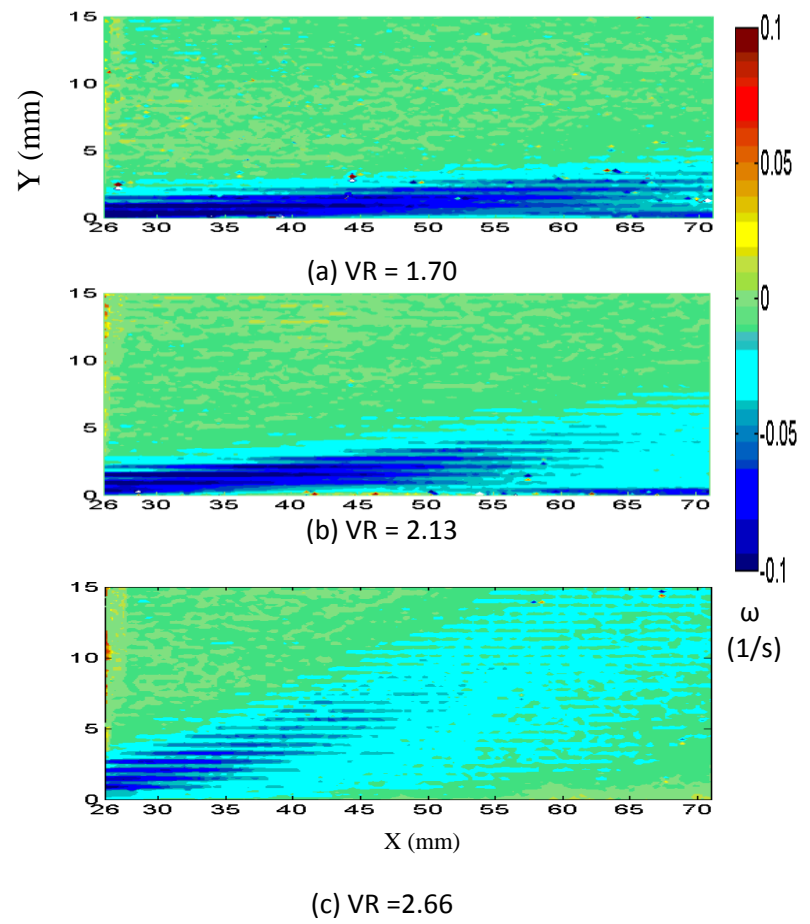
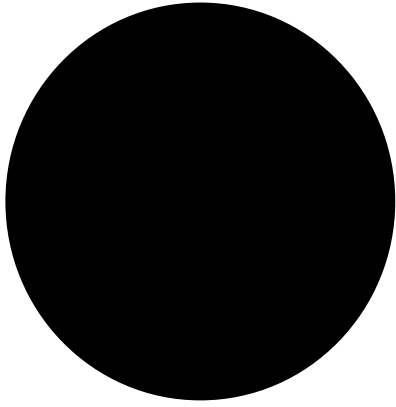


Figure 4.7: Time-averaged vorticity contour for different VRs

When not rotating ( $VR = 0$ ) in fig. 4.6a, the cylinder wake is found to be visible outside the flat plate boundary layer. The wake is found to be pushed upward ( $VR = 1.70$ ) as rotation speed increases and the wake of the cylinder vanishes from the region of interest as the rotation speed ( $VR = 2.66$ ) is further increased.

From fig. 4.7, it can also be seen that the turbulent flow is approximately inviscid outside the boundary layer. To understand the mechanism of TBL separation, the rotating cylinder can be considered a real vortex with a solid body rotational core with peak velocity at the cylinder edge. Outside the cylinder edge, the flow induced by the cylinder rotation (other than the viscous wake) acts as an irrotational vortex flow. As cylinder speed increases, the strength of the APG increases, causing earlier and stronger separation of the flat plate boundary layer. Time-averaged vorticity contours in fig. 4.7 show that the mean size of vortices found within the separated shear layer increases with an increase of APG. Again, no positive counterclockwise vorticity from the lower half of the cylinder wake was found to be present in the measurement region as the rotating cylinder pulls the wake up and away from the wall.

#### 4.4.3 Using Cylinder Speed and Location for Generating Various Amounts of APG

When a turbulent boundary layer is submitted to an APG, the flow near the wall is most prone to reversal due to the suction pressure upstream. Thus, patches of flow decelerate until some backflow occurs at the incipient detachment point. The reversed flow occurs in the low-momentum region of the boundary layer and is caused by the low-pressure region upstream.

To present the uncertain nature of separated flow in the turbulent region, backflow coefficient ( $\chi$ ) is calculated, which is the share of time the flow at a certain position runs against the free stream flow (fig. 4.8).

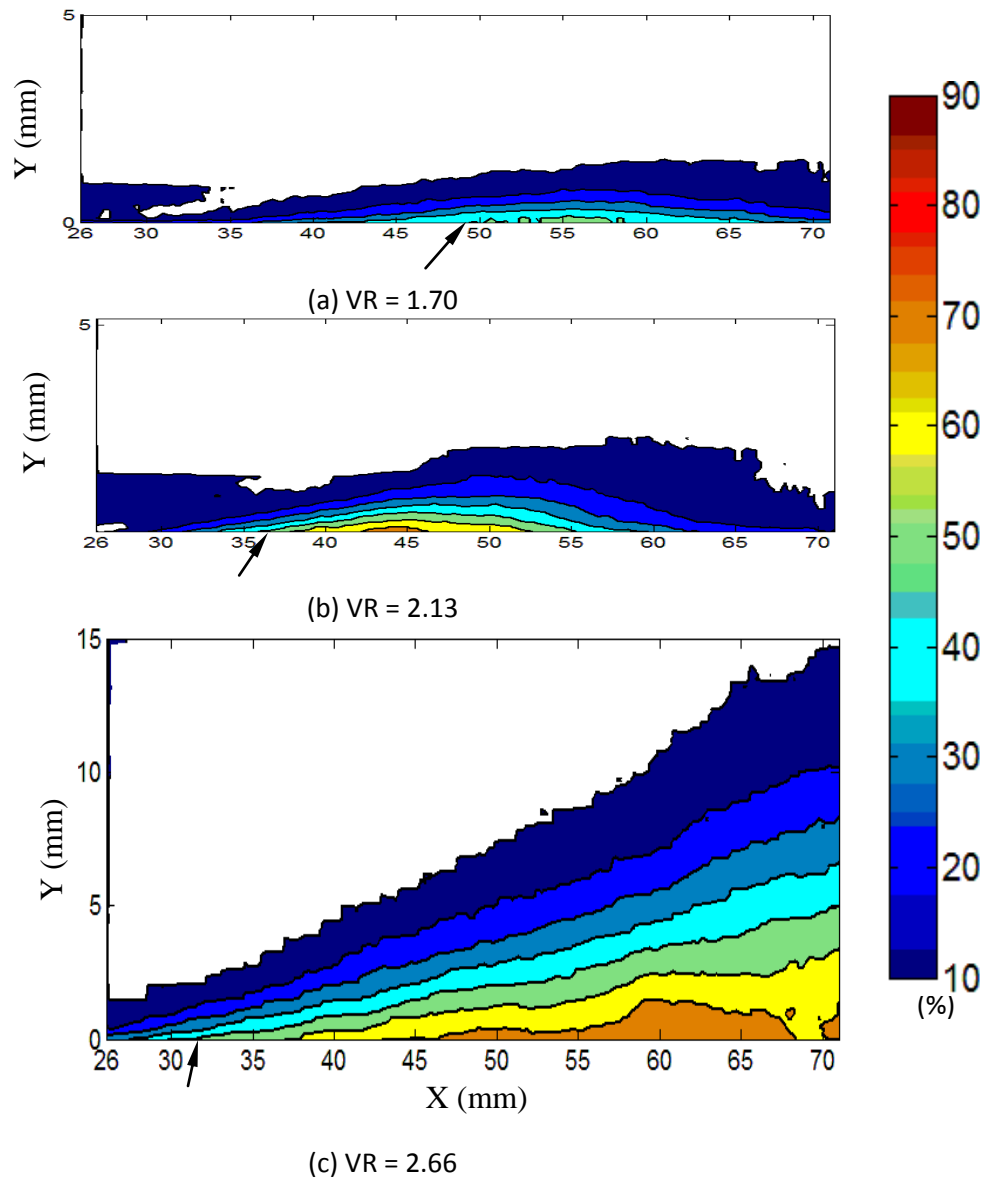
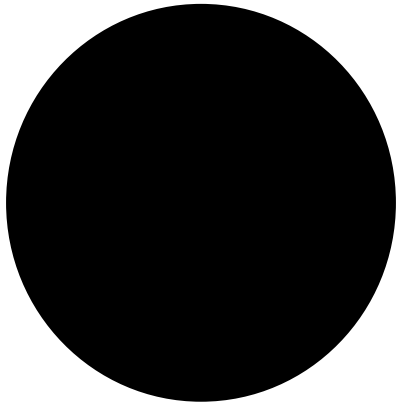


Figure 4.8: Backflow coefficient contour ( $\chi$ ) increases 10% toward the wall at each contour level for different VRs (here, the arrow indicates the separation point)

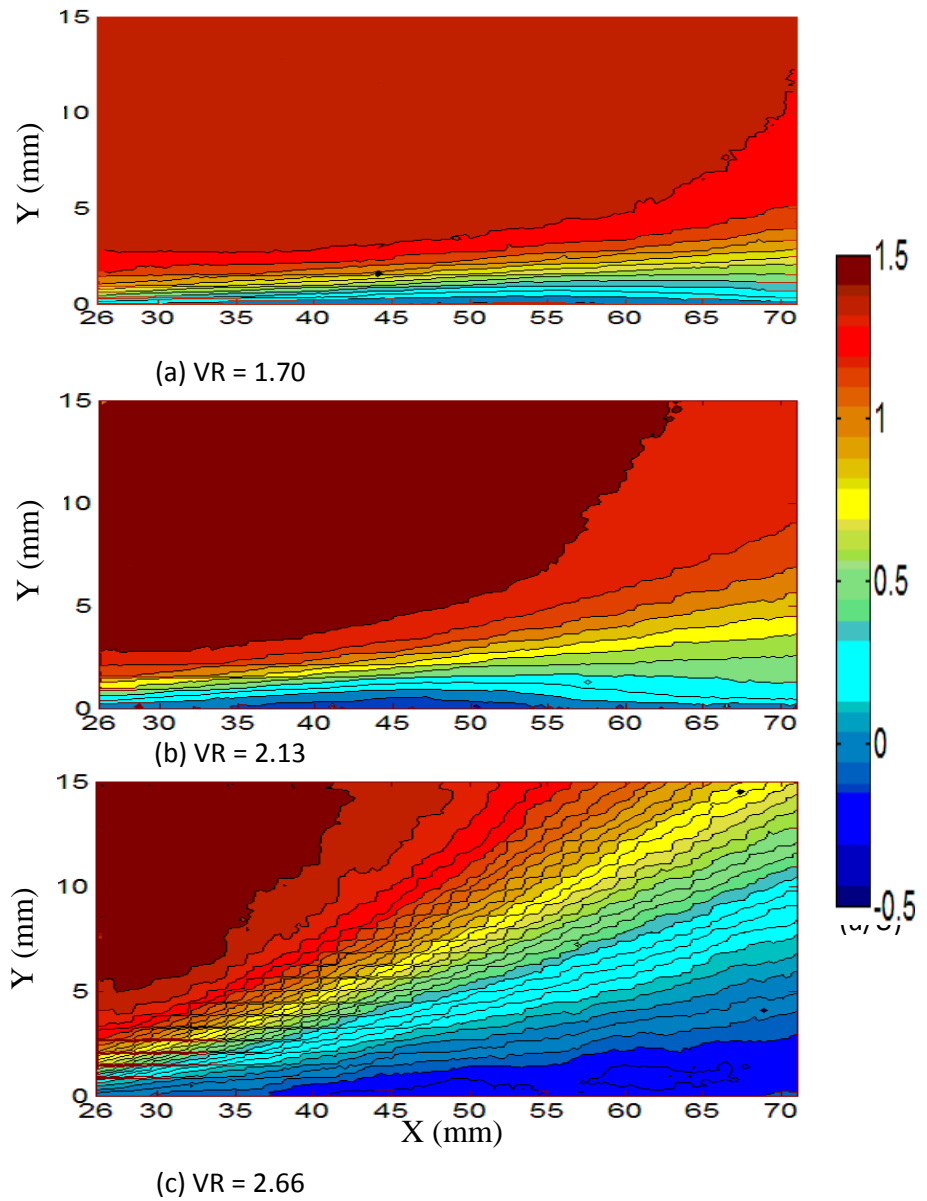
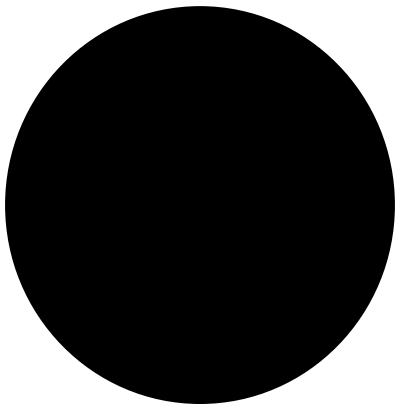


Figure 4.9: Time-averaged velocity contour for different VRs for a fixed cylinder gap ratio ( $G/D = 0.75$ )

The contours of backflow coefficient give a clear picture of instability of the TBL separation region. The height of the separation region varies greatly with time. The contour of backflow coefficient ( $\chi$ ) gives an indication of the time-averaged size and shape of the separated region.

Flow separation region where  $\chi = 50\%$  is a very important state for analysis as J. Gustavsson [13] calculated the backflow coefficient ( $\chi$ ) and showed that  $\chi = 50\%$  coincides very well with the line  $U = 0$ . According to Simpson [1, 2], backflow coefficient ( $\chi$ ) = 50% is the state where detachment of flow starts and the time-averaged wall shear stress is zero at this point. In this case, it has been observed that at low  $VR = 1.7$ , the highest amount of backflow goes up to 50%. But as the rotation speed increases for a fixed gap to height ratio ( $G/D = 0.75$ ), the contour level and also the magnitude of backflow coefficient increases. For  $VR = 2.66$ , the backflow coefficient ( $\chi$ ) increased to about 70%. Both backflow coefficient ( $\chi$ ) contour plots for  $VR = 1.7$  and  $VR = 2.13$  gave stable contour lines, indicating a systematic and organized shape for the separation bubble. At  $VR = 2.66$ , a different scenario occurred, as this case indicated a full pulling away of the shear flow from the surface (fig. 4.7). Here reversed flow occurs 70% of the time near the wall and the contours are asymmetrical, and the height of the reversed flow region is greatly increased.

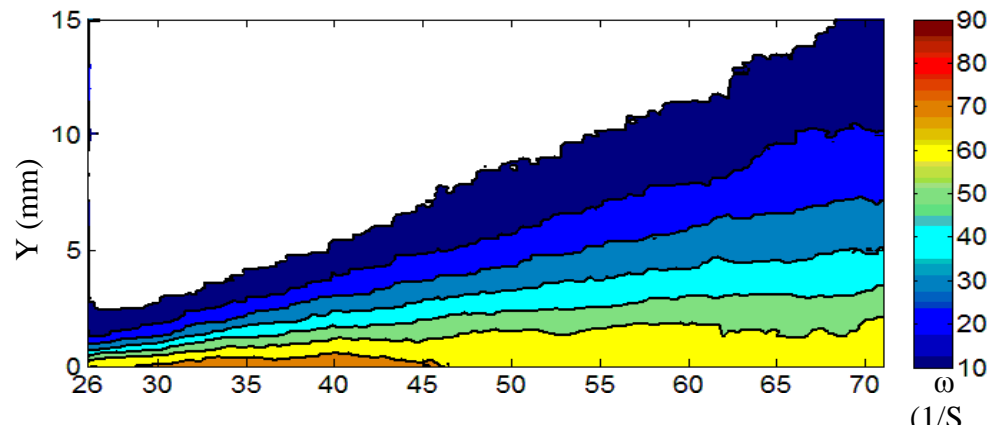
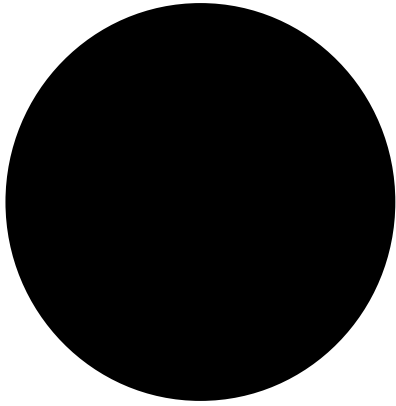
TBL separation is very unsteady in nature, and its shape changes continuously with time; thus, time averaging of the flow field is important to gain an overall picture. Fig. 4.9 presents the time-averaged contours of mean velocity fields for different cylinder rotation speeds. The height of negative stream wise velocity zone increases as rotation speed increases. The contours of negative velocities form a symmetric TBL separation bubble for lower VRs ( $VR = 1.70$  and  $2.13$ ). But if the rotation speed increases further as for  $VR = 2.66$ , the height of negative stream wise velocity magnifies largely in size and forms asymmetric boundary layer separation, as was

also indicated in the contours of backflow coefficient. Since we are interested in studying the onset of separation, a further increase of rotation speed to induce larger separation bubbles was not performed.

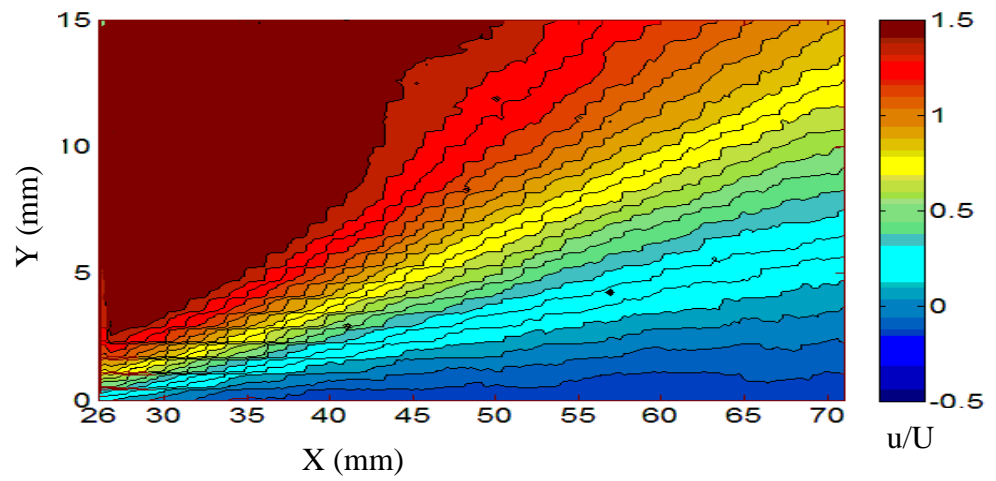
The location of the cylinder (measured as  $G/D$ ) plays a major role on the strength of the APG as predicted in the theoretical calculation. Experimental results were consistent with this prediction (fig. 4.10). The time-averaged backflow coefficient as well as velocity field contour for  $VR = 2.13$  and  $G/D = 0.5$  can be compared with those of Figures 4.8b and 4.9b. Comparison reveals that as a cylinder at a fixed  $VR = 2.16$  moves closer to wall, the TBL separation grows larger in size. So altering the gap height between the cylinder and the flat plate can also be a means of controlling the strength of the APG as long as the wake from the cylinder and the boundary layer forming over the flat plate do not come into direct contact.

Table 4.1: Comparison of experimentally measured separation point with predicted values			
G/D = 0.75			
VR	Xs (predicted) (mm)	Xs (Exp) (mm)	Xs (Mean $C_f$ ) (mm)
1.70	48	49.5	
2.13	36	37	34.8
2.66	32	32.6	29.8
G/D = 0.5			
VR = 2.13	26.8	24.7	

Table 4.1 presents a comparison of the TBL separation point as predicted using Stratford's turbulent separation criteria along with experimentally measured values. For experimental results, the separation point is defined as the point where backflow coefficient ( $\chi$ ) = 50%. It shows that Stratford's separation criteria gives good agreement with experimental results.



(a)



(b)

Figure 4.10: TBL separation for  $VR = 2.16$  and  $G/D = 0.5$  (a) backflow coefficient contour (b) mean velocity field

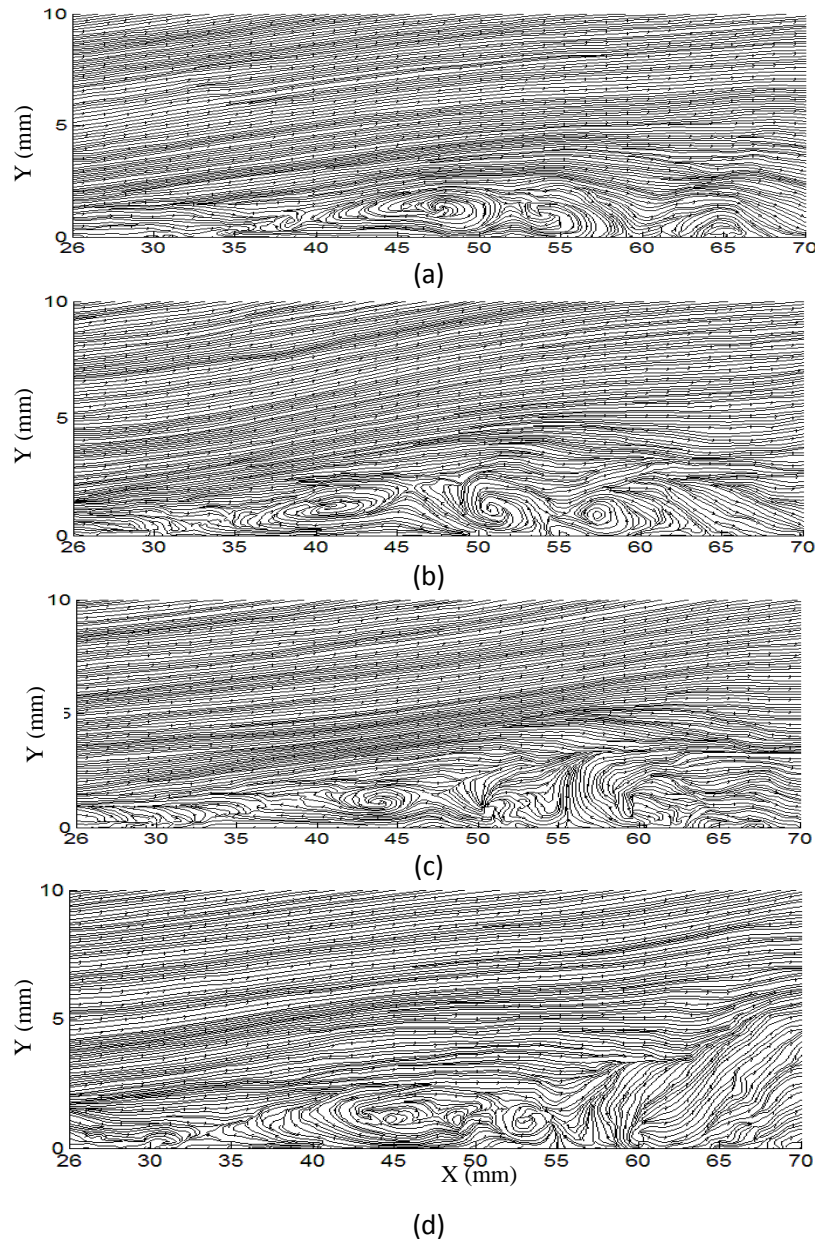


Figure 4.11. Instantaneous TBL separation and corresponding vorticity contour for  $VR = 2.66$  at a time interval of  $\Delta t = 0.2$  sec

#### 4.4.4 Instantaneous TBL Separation

Instantaneous velocity field for boundary layer separation must be examined to understand the true mechanism of how separation takes place in turbulent boundary layer flow. The measured instantaneous flow revealed a complex but organized flow structure. To understand the TBL separation over the flat plate, 4 consecutive time-averaged images (50

images or 0.05 seconds) were used to study the instantaneous shape of separation where  $VR = 2.13$  (fig. 4.11). It shows that the shape of the separation bubble is obviously changing in an interesting way with time. This sequence shows a thin detachment region that moves upstream; it erupts from the surface, and a large-scale vortex structure sheds off with a subsequent decrease in size of the separation bubble.

#### 4.4.5 Turbulent Intensities and Reynolds Stress

Contours of r.m.s profiles of turbulent intensities and Reynolds shear stress for two cylinder rotational speeds are presented in fig. 4.12. All r.m.s values are normalized by the free stream water tunnel speed. For the lower cylinder rotation speed ( $VR = 2.13$ ), the TBL separation bubble forms entirely within the measurement region; characteristics of turbulent intensities inside the detachment and recovery region are both shown. The maximum  $\left(\frac{(u'^2)^{\frac{1}{2}}}{U}\right)$  happens in the shear layer above the detachment region. It is then reduced inside the separation bubble. The contour of  $\frac{(u'^2)^{\frac{1}{2}}}{U}$  grows larger as the separated shear layer reattaches and continues to grow in size after the reattachment point ( $X = 55$  mm). The same behavior can be seen in the contour of  $\left(\frac{(v'^2)^{\frac{1}{2}}}{U}\right)$ . The peak magnitude of  $\left(\frac{(v'^2)^{\frac{1}{2}}}{U}\right)$  is found above the detachment area and then reduced significantly inside the bubble. But it rises beyond the reattachment point of the separation bubble. In the case of Reynolds shear stress, the maximum value is found downstream of the reattachment. The value of Reynolds stress starts to increase in the middle of the separation bubble and then reaches a maximum value downstream of the reattachment point. It should be noted that the same type of distribution in Reynolds stress was observed in the numerical study of Na and Moin [15].

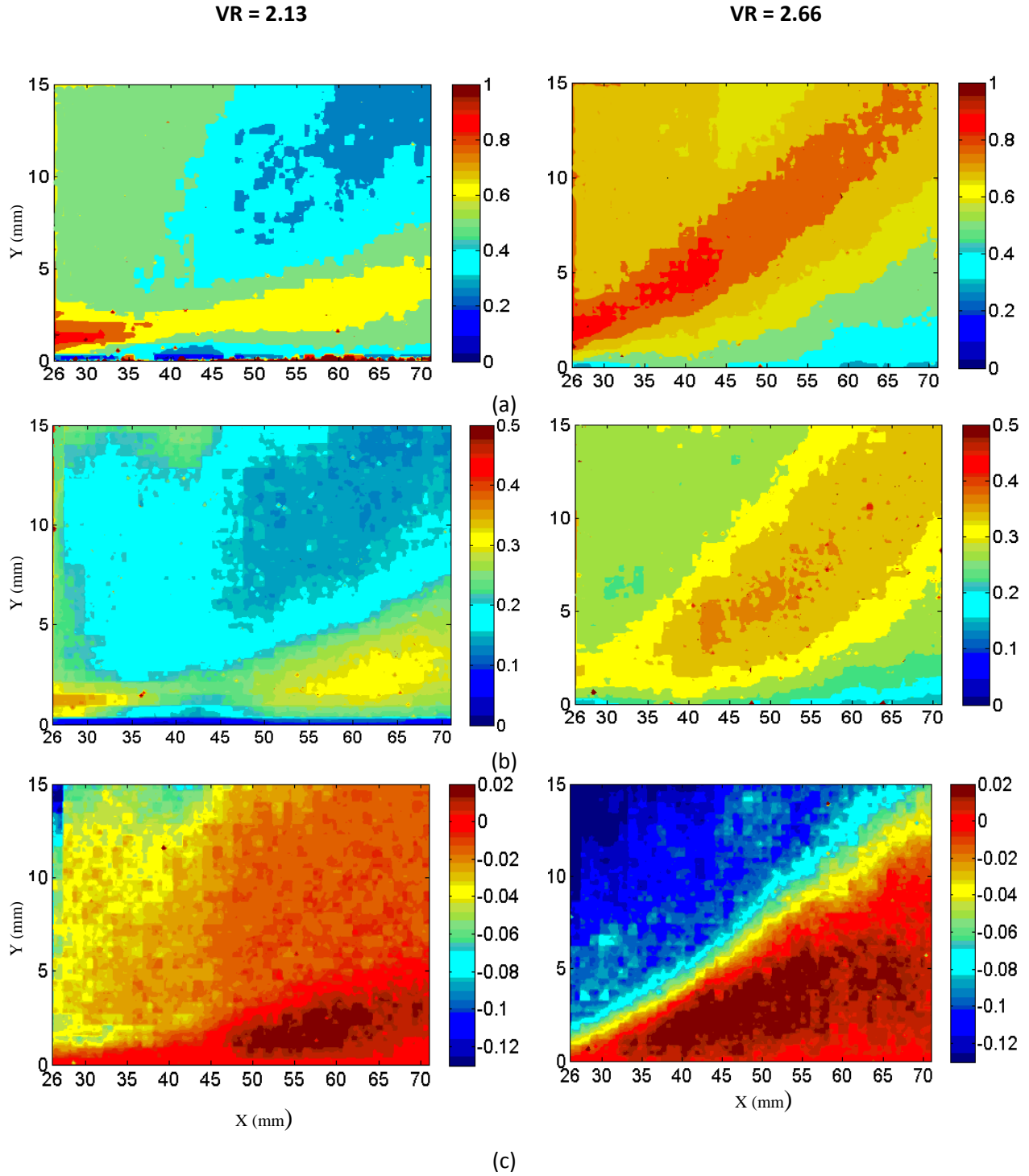


Figure 4.12: Contours of turbulence intensities (a) longitudinal component  $(\frac{(u'^2)^{\frac{1}{2}}}{U})$ , (b) wall normal component  $(\frac{(v'^2)^{\frac{1}{2}}}{U})$ , (c) Reynolds shear stress  $(-\frac{(u'v')^{\frac{1}{2}}}{U^2})$

Stronger APG (VR =2.66) gives asymmetrical TBL separation and did not reattach within the measurement region. The turbulent intensities reach a maximum above the detachment region. Reynolds shear stress starts increasing downstream of the detachment point and is found to grow larger in size with downstream from the separation point.

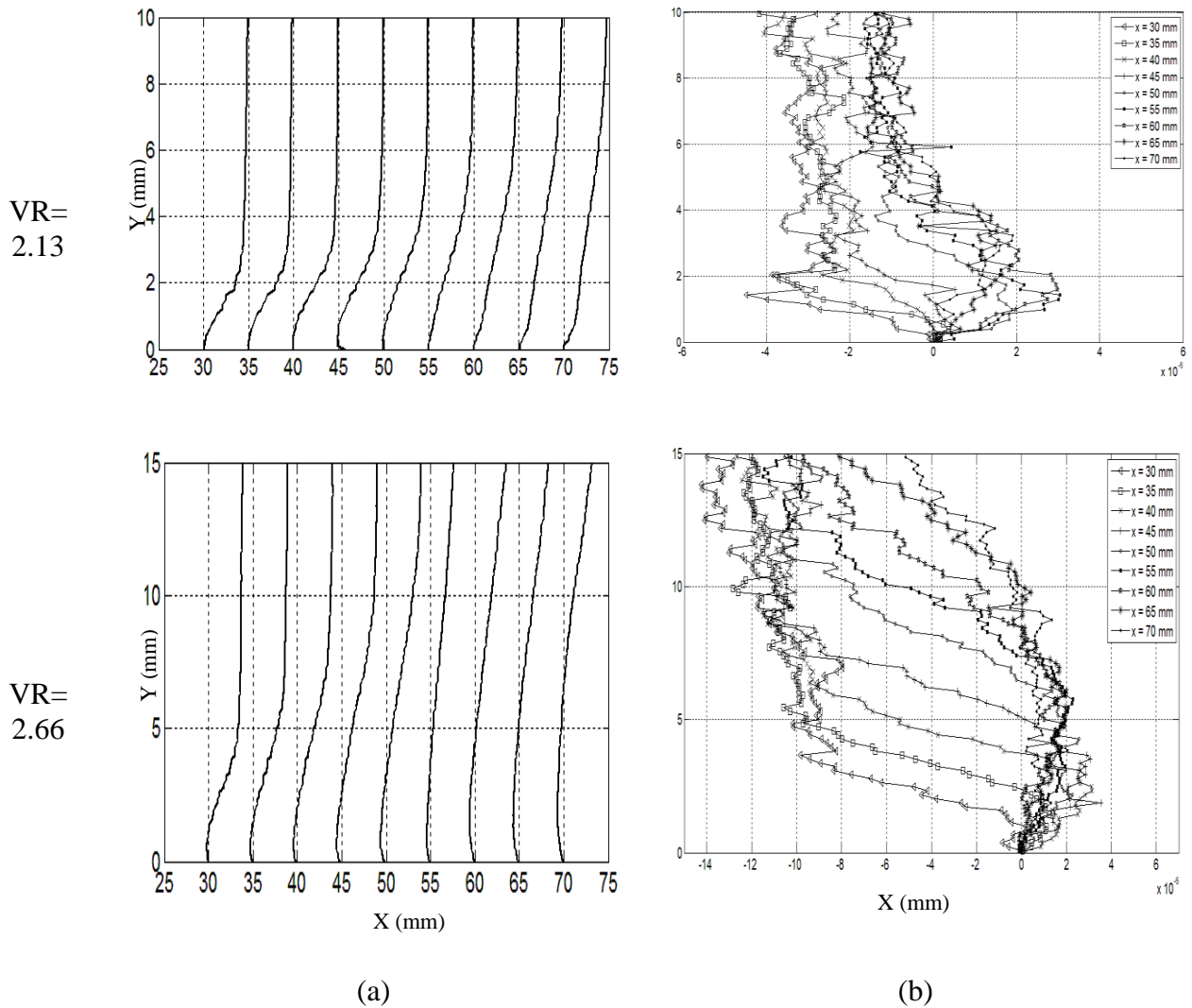


Figure 4.13: Time-resolved velocity profiles for various VR(a) u/U profiles, (b) Reynolds shear stress

$$\left(-\frac{\overline{u'v'}}{U^2}\right)^{\frac{1}{2}}$$

#### 4.4.6 Time-Averaged Velocity Profiles

Fig. 4.13 presents stream wise velocity and Reynolds stress profiles which are normalized by free stream water tunnel speed. Velocity profiles are the representative of the major flow regions: detachment region, separation zone, reattachment zone, and post-reattachment zone.

Reynolds stress profiles at a different zone reveal a steep rise in the amount of Reynolds shear stress following separation.

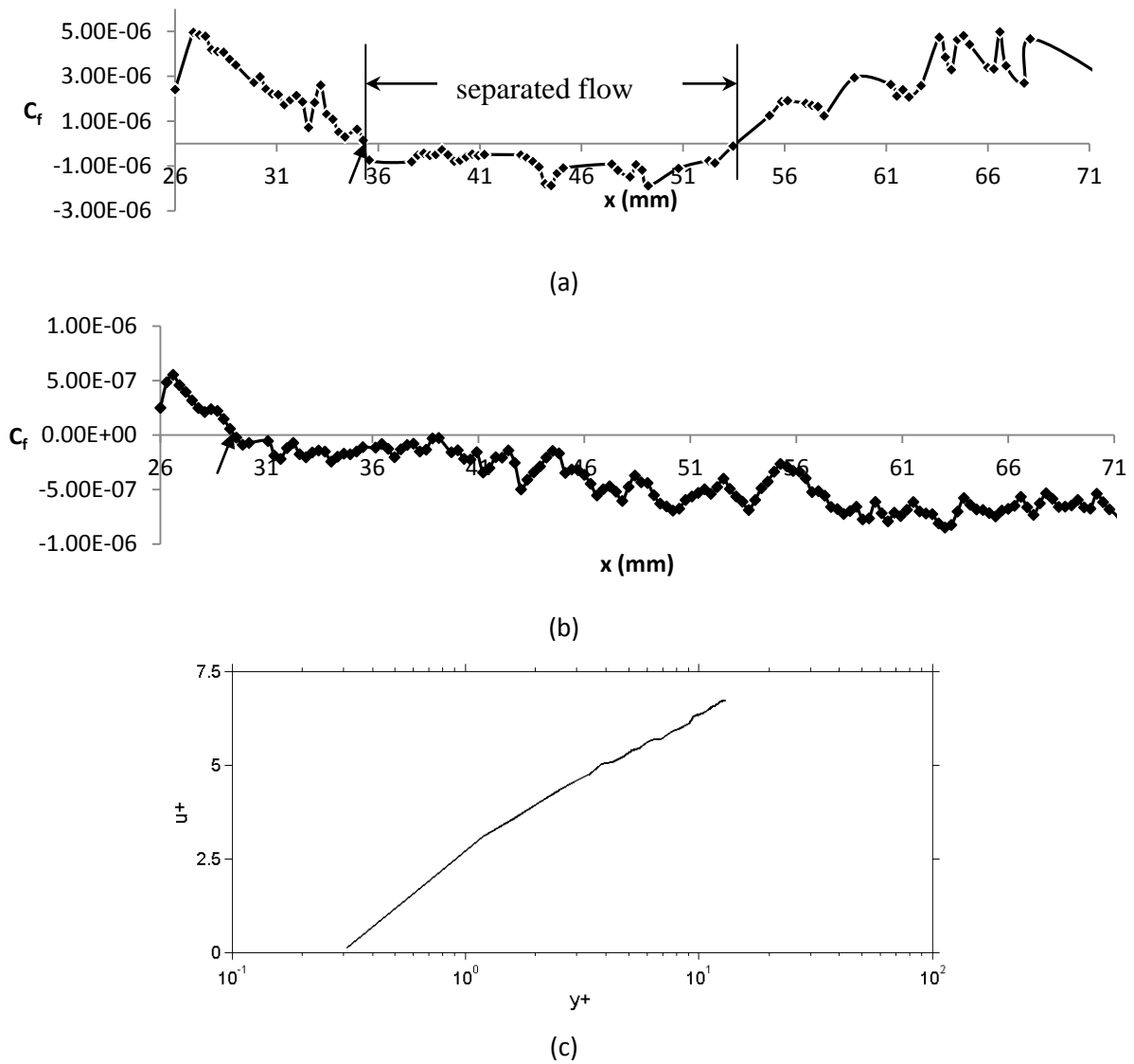


Figure 4.14: Skin friction coefficient ( $C_f$ ) profile near the wall for different VRs (a) VR = 2.13, (b) VR = 2.66 (here the arrow indicates the separation point), (c) mean velocity distribution

#### 4.4.7 Skin Friction Coefficient

Plotting the mean skin friction coefficient along the flat plate is another method of locating the detachment and reattachment point of TBL separations (fig. 4.14). In a turbulent boundary layer, viscous effects are dominant near the wall, particularly in that region closest to the wall known as the viscous sub-layer ( $y^+ < 5$ ). Fig. 4.14 (c) shows the mean velocity distribution, where the ratio of  $u^+$  to  $y^+$  is approximately 1:1 within the viscous sub-layer. Mean skin friction coefficient was calculated from the DPIV velocity data at the points close to the wall ( $y = 0.15$  mm or  $y^+ = 3.16$ ) which lies within the viscous sub-layer region. MATLAB scripts were developed to read the processed vector files generated by the DPIV software. The size of the smallest grid was  $0.283 \times 0.177$  mm, and then wall shear stress ( $\tau_w = \mu \frac{\partial U}{\partial y}$ ) was measured from two subsequent grid points. The skin friction was then calculated from these stress values and shown in fig. 4.14. The point where the skin friction coefficient falls below zero is defined as the separation point. This method results in slightly under-predicted (less than 6% deviation) points of flow separation as compared to Stratford's theoretical technique and the backflow coefficient calculation (Table 4.1).

#### 4.5 Conclusion

A study of 2-D turbulent flow separation was conducted in a water tunnel using a new technique consisting of a rotating cylinder to generate an APG. The experimental study was performed corresponding with a theoretical model for predicting the strength of the APG, and results give a good agreement between the theoretical predictions and the measured separation points. The rotating cylinder technique has proven to be a very flexible and innovative method to generate different strengths of APG to induce TBL separation. DPIV analysis revealed that the physical characteristics of flow separation are a function of the strength of the APG, which can

be altered by rotation rate and location of the cylinder. The 2-D experimental results also explored the unsteady and complex nature of TBL separation.

## Acknowledgments

Support under NSF grant 0932352 and NSF-REU grant 1062611 is gratefully acknowledged. First author Farhana Afroz was also supported by a scholarship through the Alabama EPSCoR Graduate Research Scholars Program.

## References

1. Simpson, R. L., Chew, Y. T., & Shivaprasad, B. G. (1981). The structure of a separating turbulent boundary layer. Part 1. Mean flow and Reynolds stresses. *Journal of Fluid Mechanics*, 113, 23–51.
2. Simpson, R. L., Chew, Y. T., & Shivaprasad, B. G. (1981). The structure of a separating turbulent boundary layer. Part 2. Higher-order turbulence results. *Journal of Fluid Mechanics*, 113, 53–73.
3. Simpson, R. L. (1989). Turbulent boundary-layer separation. *Ann. Rev. Fluid Mech.* 21, 205–34.
4. Song, S., DeGraaff, D. B., & Eaton J. K. 2000. Experimental study of a separating, reattaching, and redeveloping flow over a smoothly contoured ramp. *International Journal of Heat and Fluid Flow* 21, 512–519.
5. Song, S., & Eaton, J. K. 2004. Reynolds number effects on a turbulent boundary layer with separation, reattachment, and recovery. *Experiments in Fluids* 36, 246–258.
6. Radhakrishnan, S., Keating, A., Piomelli, U., & Lopes, A. S. Large-eddy simulations of high Reynolds-number flow over a contoured ramp. *44th AIAA Aerospace Sciences Meeting and Exhibit*.
7. Lamballais, E., Silvestrini, J., & Laizet, S. 2008. Direct numerical simulation of a separation bubble on a rounded finite-width leading edge. *International Journal of Heat and Fluid Flow* 29, 612–625.
8. Lamballais, E., Silvestrini, J., & Laizet, S. 2010. Direct numerical simulation of flow separation behind a rounded leading edge: Study of curvature effects. *International Journal of Heat and Fluid Flow* 31, 295–306.

9. Bandyopadhyay, P. R. & Ahmed, A. Turbulent boundary layers subjected to multiple curvatures and pressure gradients. *Journal of Fluid Mechanics*, 246, 503–527.
10. Webster, D. R., DeGraaff, D. B., & Eaton, J. K. (1996). Turbulence characteristics of a boundary layer over a two-dimensional bump. *Journal of Fluid Mechanics*, 320(1), 53-69.
11. Wu, X., & Squires, K. D. (1998). Numerical investigation of the turbulent boundary layer over a bump. *Journal of Fluid Mechanics*, 362(1), 229-271.
12. Patrick, W. P. 1987. Flow field measurements in a separated and reattached flat plate turbulent boundary layer. *NASA Contractor Rep.* 4052.
13. Gustavsson, J. 1999. Turbulent flow separation, Master's thesis, Dept. Mechanics, Royal Institute of Technology, Stockholm.
14. Coleman, G. N. & Spalart, P. R. 1993. Direct numerical simulation of a small separation bubble. *In near-wall turbulence flows* (ed. C. G. Speziale & B. E. Launder) 286 (Elsevier), 277.
15. Na, Y. & Moin, P. 1998. Direct numerical simulation of a separated turbulent boundary layer. *Journal of Fluid Mechanics*, 370, 175–201.
16. Manhart, M. & Friedrich, R. 2002. DNS of a turbulent boundary layer with separation. *Int. J. Heat and Fluid Flow* 23(5), 572–581.
17. Skote, M. & Henningson, D. S. 2002. Direct numerical simulation of a separated turbulent boundary layer. *Journal of Fluid Mechanics*, 471, 107–136.
18. Afroz, F., Lang, A., & Jones, E. Using a rotating cylinder to induce a laminar separation bubble over a flat plate. *European Journal of Mechanics B/Fluids* (under review).
19. Kundu, P. 1990. *Fluid mechanics*. San Diego, CA: Academic Press, 272–273.
20. Stratford, B. S. January 1959. The prediction of separation of the turbulent boundary layer. *Journal of Fluid Mechanics* 5(1), 1–16.
21. Hart D. P. July 13–16, 1998. PIV Error Correction, *9th International Symposium on Applications of Laser Techniques to Fluid Mechanics*. Lisbon, Portugal.
22. Willert, C. E., & Gharib, M. (1991). Digital particle image velocimetry. *Experiments in fluids*, 10(4), 181-193.

23. Huang, H., Dabiri, D., & Gharib, M. (1997). On errors of digital particle image velocimetry. *Measurement Science and Technology*, 8(12), 1427.
24. Schlichting, H. (1968). *Boundary-layer theory* (Vol. 539). New York: McGraw-Hill.
25. Prandtl, L. (1963). *The essentials of fluid dynamics*. Blackie & Son Limited.

## CHAPTER FIVE

### EXPERIMENTAL STUDY OF LAMINAR AND TURBULENT BOUNDARY LAYER

#### SEPARATION CONTROL OF SHARK SKIN\*

Farhana Afroz<sup>1</sup>, Amy Lang<sup>1</sup>, Philip Motta<sup>2</sup>, Maria Habegger<sup>2</sup>

<sup>1</sup>Department of Aerospace Engineering and Mechanics, The University of Alabama

<sup>2</sup>Department of Integrative Biology, University of South Florida

#### Abstract

The Shortfin Mako shark (*Isurus oxyrinchus*) is a fast swimmer and has incredible turning agility. Shark skin is covered with flexible scales and has the ability to bristle up to 50° in flank regions. This bristling capability may result in a unique Boundary Layer Control (BLC) method to reduce drag. It is hypothesized in previous work that scales bristle when the flow above it is reversed, and between the bristled scales embedded micro-vortices form in the cavities which induce boundary layer mixing and assist in delaying flow separation. To substantiate the hypothesis that shark skin can control flow separation, samples of skin from the flank region have been tested in a water tunnel facility under various strengths of adverse pressure gradient (APG). Laminar and turbulent separation over the skin was studied experimentally using Time-Resolved Digital Particle Image Velocimetry (TR-DPIV), where the APG was generated and varied using a rotating cylinder. Shark skin results were compared with that of a smooth plate data for a given amount of APG. Both the instantaneous and time-averaged results reveal that shark skin is capable of controlling laminar as well as turbulent separation. The shark skin under APG causes an early transition to turbulence and reduces the degree of laminar separation. For turbulent separation, the presence of the shark skin reduces the amount of backflow and size of the separation region. Shark skin is also responsible for delaying the laminar and turbulent separation as compared to a smooth wall.

\*To be submitted to *Bioinspiration & Biomimetics*

## 5.1 Introduction

Drag reduction inspired by nature has special interest in the field of fluid mechanics. In nature, the skin of sharks is covered by minute placoid scales, also called dermal denticles; these primarily serve the purpose as a protecting armor to the animal [1] The base of a single tooth-like scale is embedded in the external collagenous layer of the skin (dermis), termed the stratum laxum, and the crown of each scale is exposed to the water. Because of the unique features of shark denticles, they have been considered since the 1980's for their drag reduction potential [9-11, 14, 15].

Early research focused on the hydrodynamic effects of the ridges on the crowns of the scales, acting as riblets to reduce the turbulent skin friction drag over the shark's body. Man-made riblets showed a turbulent shear stress reduction of 9.9% over that of a smooth surface [2]. In previous work, the model scales were made to lie flat on the surface, and the bristling of the scales was not investigated. Bechert et al. [3, 4] built a shark skin replica consisting of an array of shark scales with compliant anchoring and then tested the model in a fully turbulent oil channel for measuring the skin friction drag. This experimental study showed that when the scales were not bristled but were laid flat so that the scales rested on each other, the drag reduction was found to be only about 3%. The performance with respect to man-made riblets decreases possibly because of the tiny residual gaps between the scales. However as the shark scales were bristled up to  $12^\circ$ , with variation in spring stiffness and damping for each scale, an increase in skin friction drag resulted. Other research also showed shark scale riblet models to be capable of reducing skin friction drag [5, 6].

It should be noted here that it has been theorized by others that bristled shark scales could act as vortex generators to control the flow separation [3, 4, and 7]. Vortex generators are a

passive mechanism for controlling flow separation. These are small, vertical v-shaped structures at the surface that protrude into the boundary layer. As the flow encounters the vortex generators, stream wise vortices are created downstream and mix high momentum turbulent energy in the boundary layer [8]. Scales over shark skin are hypothesized to bristle passively in the reversed flow region near or downstream of the point of separation, and thus our hypothesis offers new and different mechanism for controlling flow separation from that of traditional vortex generators.

The present study focuses on investigating flow over skin samples from the Shortfin Mako (*Isurus oxyrinchus*) as it is one of the fastest swimming marine creatures. These scales are 0.2 mm in average size and are uniformly oriented from nose-to-tail and anchored to the shark's skin in such a way that they are able to pivot about their anchor when flow is reversed in the stream wise direction. Previous research work was carried out to determine the maximum bristling angle of scales that can be maintained with structural integrity within the skin (Fig. 5.1). Among the bristling angle for 16 different regions it can be found that the highest scale flexibility occurs on the flank and trailing edges of the pectoral fin, with bristling angles up to a range of approximately  $50^\circ$  on the flank as reported by Motta et al. [9]. It is very interesting that the regions where maximum bristling occurs correspond to the regions with one would predict the presence of an adverse pressure gradient due to the shark's body shape.

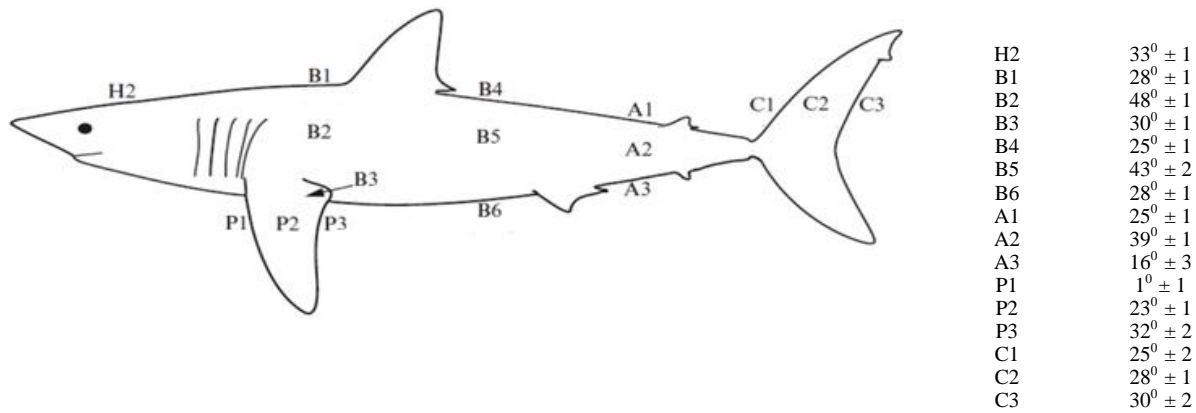


Figure 5.1: Outline of measured scale bristling angles at various locations on the Mako Shark, (Motta *et al.* 2012 [9])

It is hypothesized by Lang [10] that for a flow experiencing an APG; it is the region closest to wall with lowest momentum where reverse flow is initiated. This reversed flow actuates the scales thereby disrupting the process leading to flow separation. It is theorized by Lang [10, 11] that scales of Shortfin Mako shark act as a passive flow-actuated mechanism as means of separation control.

Moreover, SEM images of individual scales showed that the geometry of the structural base differs by body location. More firmly anchored scales (lower bristling capability) have a more symmetrical base and flank region scales have bases that are wider than deep, facilitating pivoting during erection. Thus, it has been hypothesized by Lang [10, 11] that these scales which are loosely embedded in the shark's skin, are able to erect in the presence of reversing flow due to an adverse pressure gradient, trapping the reversing flow and forming transverse grooves with embedded vortices between them.

The idea that two-dimensional transverse grooves could be a possible means of drag reduction was proposed by Bushnell [12]. As flow passes over a single groove, a partial-slip condition results from embedded vortices of trapped fluid in each groove. The embedded vortices in the cavities imposes a shear stress at the bottom of cavity which results a small thrust

adding to the net reduction in drag for the surface. This was termed a 'micro-air bearing effect' by Bushnell [12]. However, the mixing induced into and out of the cavities increased the overall skin friction drag. Howard and Goodman [13] observed the effect of transverse embedded grooves on the drag characteristics of axisymmetric bluff bodies; they predicted the grooves would help to control flow separation and reduce pressure drag. It was theorized that grooves were responsible for vortices shedding into the boundary layer and thus acted as trip in the laminar flow. A drag decrease and corresponding reduction in the size of the separation region was found in this study.

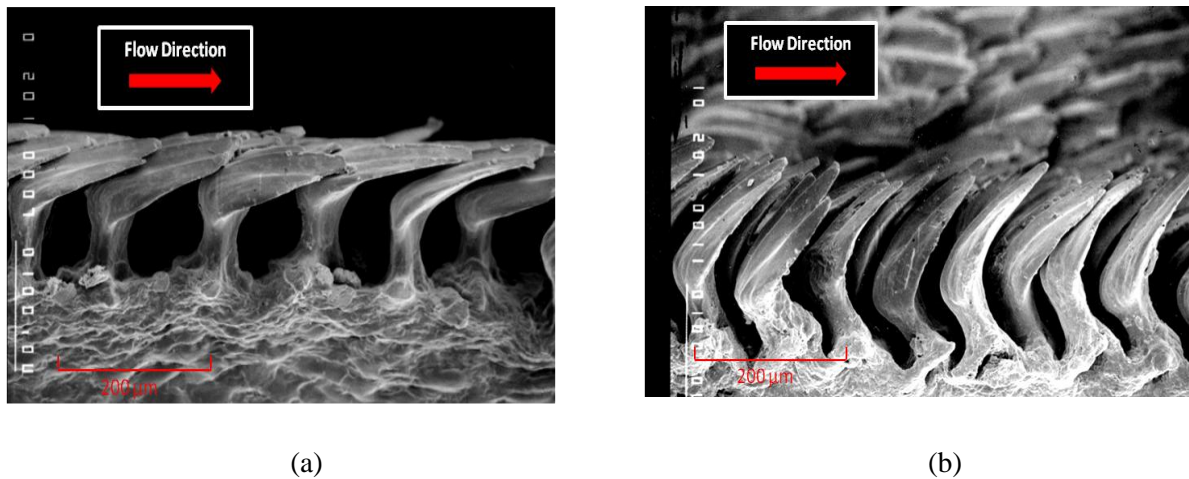


Figure 5.2: (a) SEM of non-bristled Mako scales. (b) SEM of manually bristled scales and the formation of cavities between the scales. The angle of erection is only approximate.

Previous experiments conducted by Lang et al [14] over a bristled shark skin model revealed the formation of embedded vortices between replicas of the scales. As the scales bristle the formation of embedded vortices would allow the flow to pass over the skin with a partial slip condition, thereby leading to higher momentum adjacent to the surface, while also increasing mixing and thus momentum exchange within the boundary layer. Thus the bristled shark skin may have more than one technique of controlling the boundary layer to decrease overall pressure

drag. Fig. 5.2 shows the formation of cavities (about 200  $\mu\text{m}$  in size) between the scales of real shark skin in a bristled orientation. The scales are oriented in staggered rows with overlap between the tips of the scales on one row and the bases of the scales on the following row.

A study conducted on a flapping robotic foil determined the self-propelled swimming speed as a measure of locomotive performance of both Mako shark skin covered foils vs. sanded skin surface [15]. It has been hypothesized that the shark skin scales give a preferred flow direction so that when flow reversal occurs close to the surface during the onset of separation, the scales are passively bristled and the process leading to global flow separation is disrupted [16]. Shark skin with the intact surface denticles showed a mean 12.3% increase in swimming speed compared with the same sanded skin foils. This study also suggested that shark skin denticles may alter vortex location which could increase thrust. But questions still remained as to how shark skin denticles modify the boundary layer flow. The present study may provide insight as to the method by which shark scales control the boundary layer flow.

Real shark skin samples from the flank region with most flexible scales of a Shortfin Mako (*Isurus oxyrinchus*) were tested under various amounts of adverse pressure gradient (APG). The variation of APG was performed with the use of a rotating cylinder which was proven to be an innovative and easy technique to induce both laminar and turbulent boundary layer separation [17, 18]. Time-Resolved Digital Particle Image Velocimetry (TR-DPIV) was used to compare the laminar and turbulent boundary layer separation over shark skin with that of a smooth plate data for a given amount of APG. The shark skin was tested for one free stream tunnel speed (0.132 m/s) at laminar flow condition with a local Reynolds number ( $Re_x$ ) of  $Re_x \approx 1.3 \times 10^5$  in the measurement region based on the distance from leading edge of the flat plate. But for the turbulent flow, studies were done for two free stream tunnel speeds (0.25 m/s)

and (0.3 m/s) which gave Reynolds number values of  $Re_x \approx 2.5 \times 10^5$  and  $Re_x \approx 3 \times 10^5$  in the measurement region based on the distance from leading edge.

## 5.2 Experimental Procedure

### 5.2.1 Experimental setup

The experimental studies were carried out in a water tunnel facility at the University of Alabama. The water tunnel has a test section size of 38 cm wide by 76 cm tall by 275 cm long. The model used in the experiment is a flat plate interchangeable model, made out of black Plexiglas, which has the dimensions of 45.72 cm long and 60.96 cm in height and was mounted vertically in the test section. Attached to the front of this plate there is a leading plate with elliptical nose (91.44 cm in length) and then the flat plate model which is followed by a trailing edge flap. This flap was adjusted based on flow speed and blockage to prevent the formation of a separation bubble at the nose of the flat plate. The shark skin samples from the flank region were glued on another flat plate surface (fig 5.4). This sample consisted of 3 pieces each measuring 14 cm W X 17.78 cm L. These pieces were placed in the middle of another interchangeable black Plexiglas flat plate (same dimension of 45.72 cm long and 60.96 cm height). Thus, the shark skin sample measured a height of 53.34 cm (about 87.5% of total plate height).

To induce the presence of an APG, a rotating cylinder (diameter of 5.1 cm) was placed at a distance of  $L = 101.6$  cm ( $\approx 20D$ ) downstream from the leading edge of the flat plate and spanned the total width (45.72 cm) of the plate (fig 5.3). By adjusting the gap height from the plate as well as the rotation speed, the strength of the APG was varied. This system induces separation over a flat plate at a point just downstream of the cylinder. For these experiments the cylinder center was placed at the beginning edge of shark skin to ensure the formation of separation occurs over the shark skin sample. First, the shark skin model was tested by placing

the cylinder at certain gap height ( $G/D$ ) and rotation speed ( $VR$ ) for inducing a known amount of APG [17, 18]. Then keeping the cylinder at same gap height ( $G/D$ ) and rotation speed ( $VR$ ), the shark skin plate was replaced by a smooth plate model. This procedure insured testing was performed for the shark skin and smooth surfaces under the exact same amount of APG for direct comparison. Experiments were carried out for both laminar and turbulent boundary layer conditions. As shown in fig. 5.3, the flow was tripped to be turbulent at a distance,  $L_T = 50$  cm ( $\approx 10D$ ) for the latter case.

It should be mentioned that special care was taken to cut the exact dimensions of shark skin as mentioned above. The muscles and tissues under the skin were removed with help of a surgical blade as much as possible without damaging the skin structure. However, even with this care there was some minor waviness to the skin after being mounted to the flat plate (fig. 5.4).

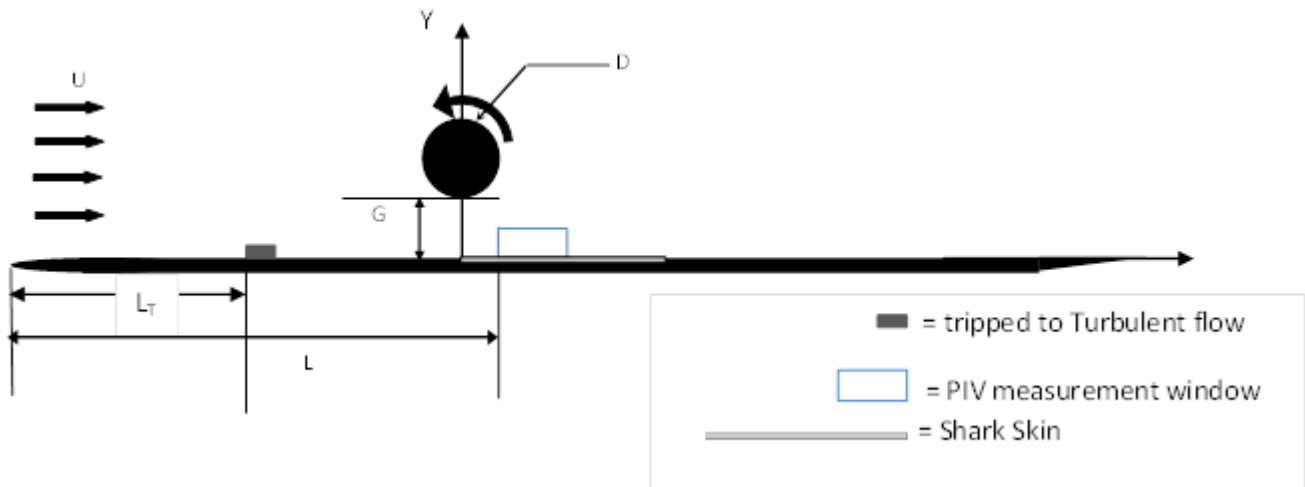


Figure 5.3: Use of a rotating cylinder to induce flow separation over a flat plate and shark skin at downstream position of cylinder.

Due to the fact that biological materials deteriorate at room temperature, the shark skin sample was kept frozen when not in use. Thawing and then refreezing causes eventual deterioration, thus this process was only performed twice to insure soundness of the skin sample

during testing. Care has also been taken so that shark skin did not come in direct contact with other objects or surfaces to avoid any contamination or damage to the scales.

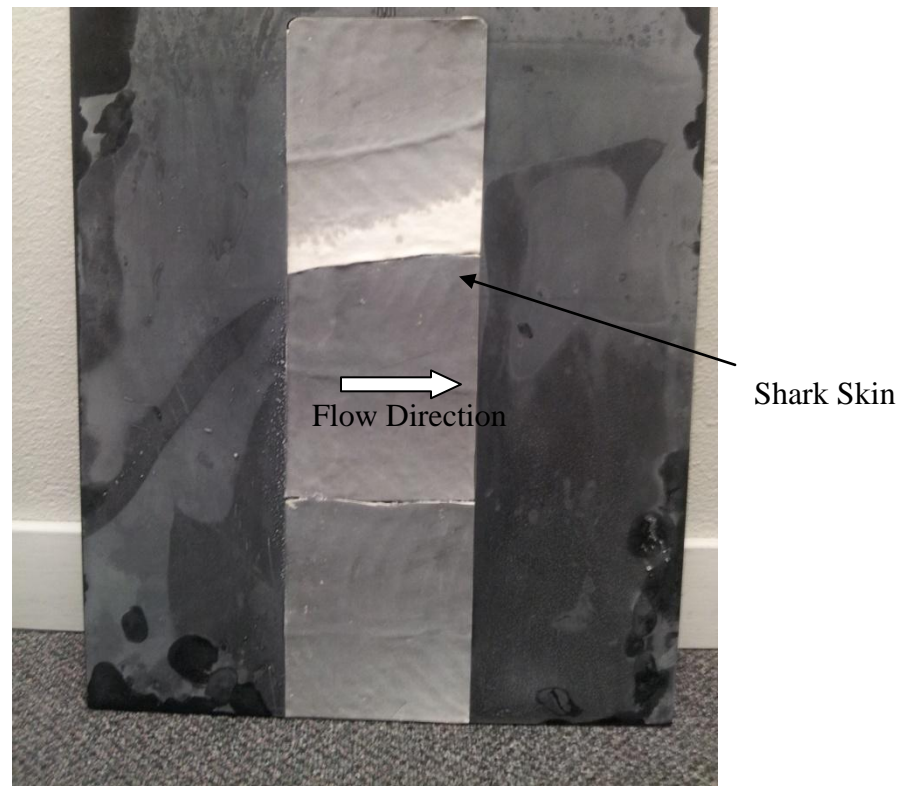


Figure 5.4: Flat plate with affixed shark skin samples, frozen

### 5.2.2 Data Acquisition and Analysis Technique

To measure the flow field with a Digital Particle Image Velocimetry (DPIV) system, the flow was seeded with  $14\ \mu\text{m}$  silver-coated hollow glass spheres and then illuminated by a laser sheet generated by a Quantronix Falcon 20 m J Nd:YLF laser. The maximum power output of this laser is 20 watts and it has a beam wavelength of 532 nm, 7 to 30 amps current output range, and .1 to 1.0 kHz frequency range. LabVIEW software here was used for image acquisition. Then Insight3G DPIV software was used to analyze the acquired images and obtain the velocity

vector field for laminar and turbulent separation. The size of each measurement window for image acquisition was 4.5 cm x 2.25 cm and images were captured by a Basler A504K high-speed camera at a rate of 1000 frames per second for turbulent flow and 500 frames per second for laminar flow.

A total of 9600 images (9.6 sec) for each rotation speed were captured at 1280 x 512 pixels and then analyzed to obtain both instantaneous and averaged statistics of the flow field. The images were captured 2.5 cm downstream of the cylinder center as identified in Fig.3. The measurement area was divided into small interrogation windows. The size of the interrogation window started with 64x32 pixels and then was reduced to 16 x 8 pixels for increased data resolution. A minimum intensity image generator was used to determine the background noise common to all of the images, and this noise was subtracted from each image to increase the accuracy of the vector calculations. During processing, Insight 3G software utilized a Recursive Nyquist Grid, FFT Correlation Engine, and Gaussian Peak Engine while post-processing filtering was performed to eliminate any bad vectors due to localized insufficient seeding. The DPIV processing software gave an estimation of the average percentage of valid vectors in each processing window, and the least measurement of good vectors was about 97%. The error associated with the DPIV technique is primarily due to insufficient data (poor seeding density or poor image quality) [19, 20] and it is very hard to calculate. In this experimental study, adequate seeding density was maintained as much as was possible during data acquisition. In literature, an acceptable estimate of error is 5% in velocity measurements and 10% in vorticity [20, 21]. The pixel/cm calibration for these data sets was 37.8 microns/pixel. Combining the error for tilting of the ruler for calibration process and processing grid error, the total error for each velocity vector was kept below 5 %.

### 5.3 Results and Discussion

An inviscid model was used to quantify the strength of the pressure gradient induced along the wall for different cylinder rotation speed,  $VR$ , and cylinder location,  $G/D$ . This inviscid theoretical model for flow about a rotating cylinder located near a wall consists of the superposition of a free stream flow, doublet and vortices. Fig. 5.5 shows how velocity ratio ( $VR$ ), Reynolds number ( $Re_x$ ) and cylinder gap height ( $G/D$ ) impact the strength of the adverse pressure gradient  $\left(\frac{\partial C_p}{\partial x}\right)$ . In this case, the value of cylinder gap to diameter ratio ( $G/D$ ) was fixed at 0.75 for all the experimental conditions. The velocity and pressure calculations along the flat plate by this theoretical model was also used for predicting the theoretical separation points in both laminar and turbulent separation [17,18] and gave good agreement with experimental observations. The measurement location for the experiments was also chosen based on these calculations and the starting point of each measurement region was chosen as  $x = 25$  mm. Beyond this point, the boundary layer is subjected to an extreme adverse pressure gradient (APG) and separation is induced on a flat surface. Fig. 5.5 (a) shows the pressure gradient plots that are used for the laminar flow separation study. Fig. 5.5(b, c) show the pressure gradient measurements which are used for the turbulent flow separation study. It should be mentioned that all the pressure gradient values were non-dimensionalized by cylinder diameter.

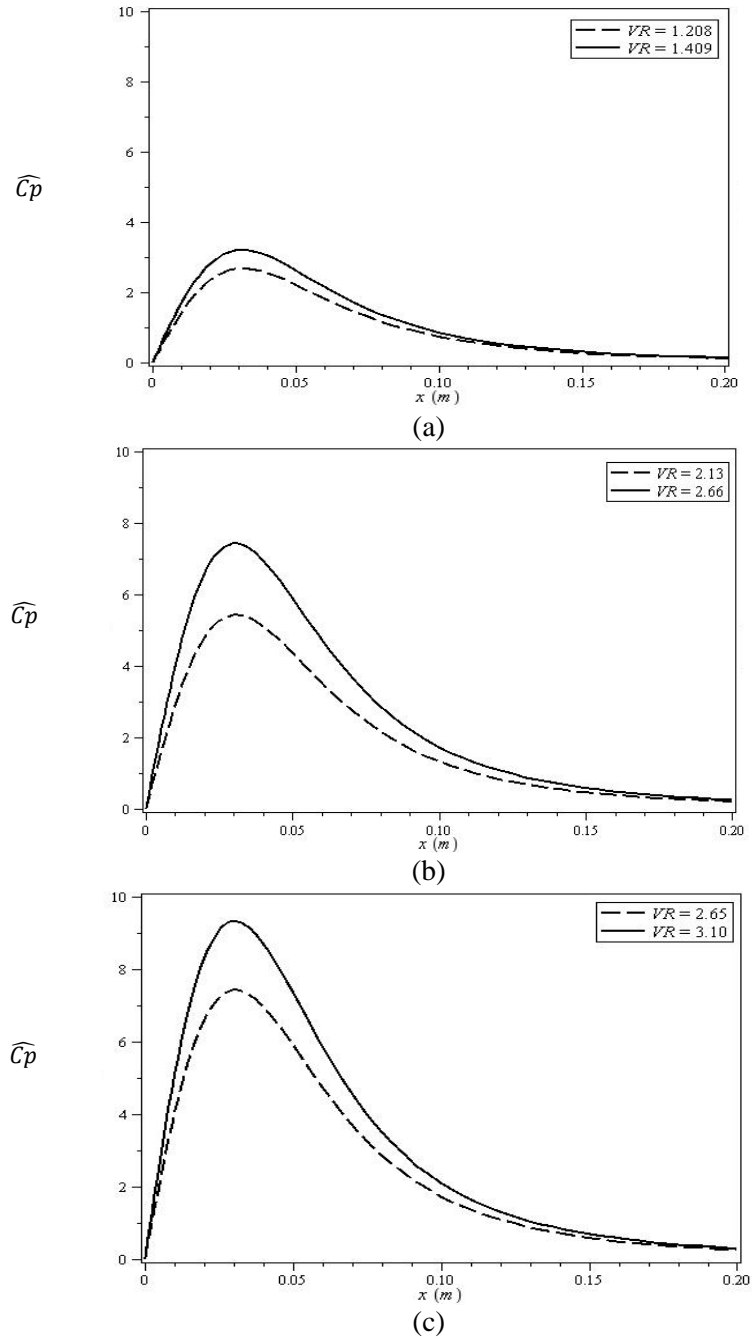


Figure 5.5: Therotical gradient of pressure coefficient for cylinder gap height,  $G/D = 0.75$  and different cylinder rotation speeds (VR), (a)  $Re_x \approx 1.3 \times 10^5$ , (b)  $Re_x \approx 2.5 \times 10^5$  and, (c)  $Re_x \approx 3 \times 10^5$

### 5.3.1 Base Flow

The flow was first studied to document the base flow without the presence of the cylinder for both laminar and turbulent flow. After confirming a clean laminar base flow in the measurement region, the flow was then subjected to an APG to induce a laminar separation

bubble. In Fig. 6 (a), the velocity profile for  $U = 0.132$  m/s at a Reynolds number,  $Re_x \approx 1.3 \times 10^5$  is compared with the theoretical Blasius profile. The theoretical Blasius profile was calculated using L. Howarth's solution [22] with zero pressure gradients and it gives close agreement with the experimental velocity profile for laminar flow. The theoretical boundary layer thickness,  $\delta$ , based on Blasius calculation is found to be 13.5 mm in comparison with the experimental value of 13 mm (fig. 5.6(a)).

Likewise, a clean base flow turbulent boundary layer over the flat plate was ensured before testing under the presence of an adverse pressure gradient. According to Prandtl [23], the one-seventh power law is a good approximation for the velocity profile up to  $Re_x = 10^7$ . In Fig. 5.6 (b), the experimental velocity profile for  $U = 0.25$  m/s at  $Re_x \approx 2.5 \times 10^5$  is compared with the theoretical one-seventh power law and also one-sixth power law. As flow is tripped to turbulent and the Reynolds number is relatively low, the experimentally measured profile shows a better match with a one-sixth law.

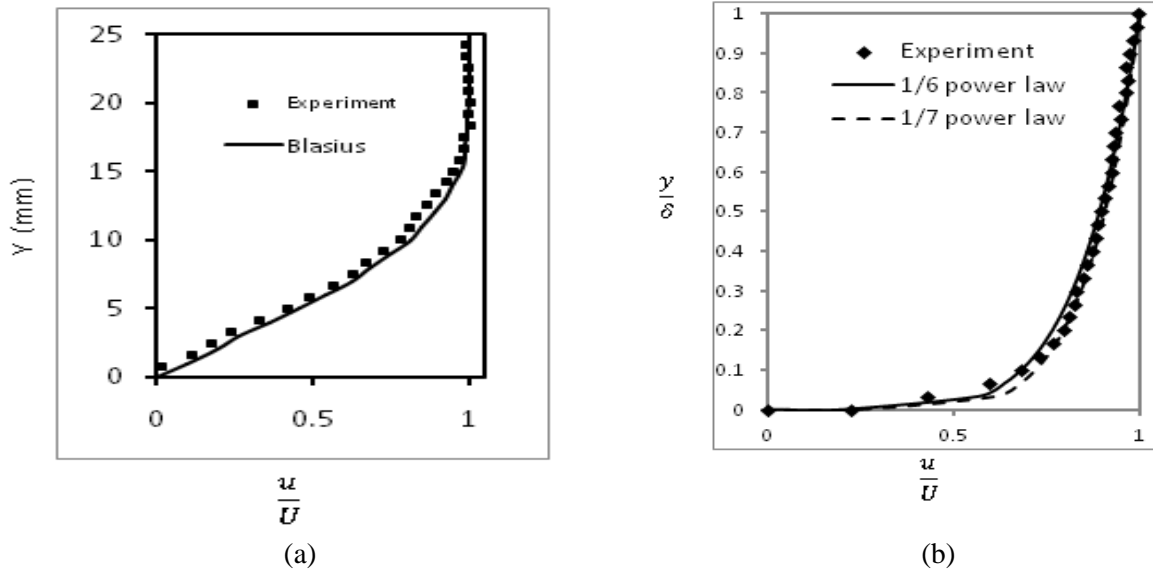


Figure 5.6: Experimental and theoretical velocity profile, (a) laminar flow ( $Re_x \approx 1.3 \times 10^5$ ), (b) turbulent flow ( $Re_x \approx 2.5 \times 10^5$ )

### 5.3.2 Pressure Gradient along Shark Body

A typical shortfin Mako shark *I. oxyrinchus* (female TL 192 cm, fork length [FL] 171.5 cm) has been considered with a body height of approximately 26 cm [9]. Discarding the tail, the shark body was assumed to be a symmetrical shape (length 155 cm, height 26 cm), and the numerical shape of the shark body (fig. 5.7 (a)) matches with the shape (fig. 5.1) of a real shark. The pressure gradient along the body was calculated to obtain a rough approximation of the pressure gradient over a shark assuming straight swimming without any body movement. This analysis was performed using commercial CFD software Ansys Fluent 13. Fig. 5.7 (a) shows the sample mesh around the numerical model of the body and the shaded region indicates the flank region. Fig. 5.7 (b) shows a plot of the inviscid non-dimensional pressure gradient along different regions of the body and fig. 5.7 (c) zooms in closer to show the pressure gradient along the flank region. It is observed from fig. 5.7 (b) that the shark body first experiences a favorable pressure gradient but near the flank region an APG after the point of maximum girth is formed. The maximum adverse pressure gradient ( $\underline{C_p}$ ) is observed to exceed 10 for an inviscid flow ( $U = 5 \text{ m/s}$ ) in the flank region. Our current experimental study (fig. 5.5) considers a maximum adverse pressure gradient ( $\widehat{C_p}$ ) of less than 4 in the laminar case of ( $Re_L = 1.3 \times 10^5$ ) separation study, and close to 10 in the turbulent case ( $Re_L \leq 3 \times 10^5$ ). So, the various magnitudes of APG ( $\widehat{C_p}$ ) induced over shark skin samples in our experiment for turbulent case is approximately equal to the APG ( $\underline{C_p}$ ) that a shark body experiences while swimming.

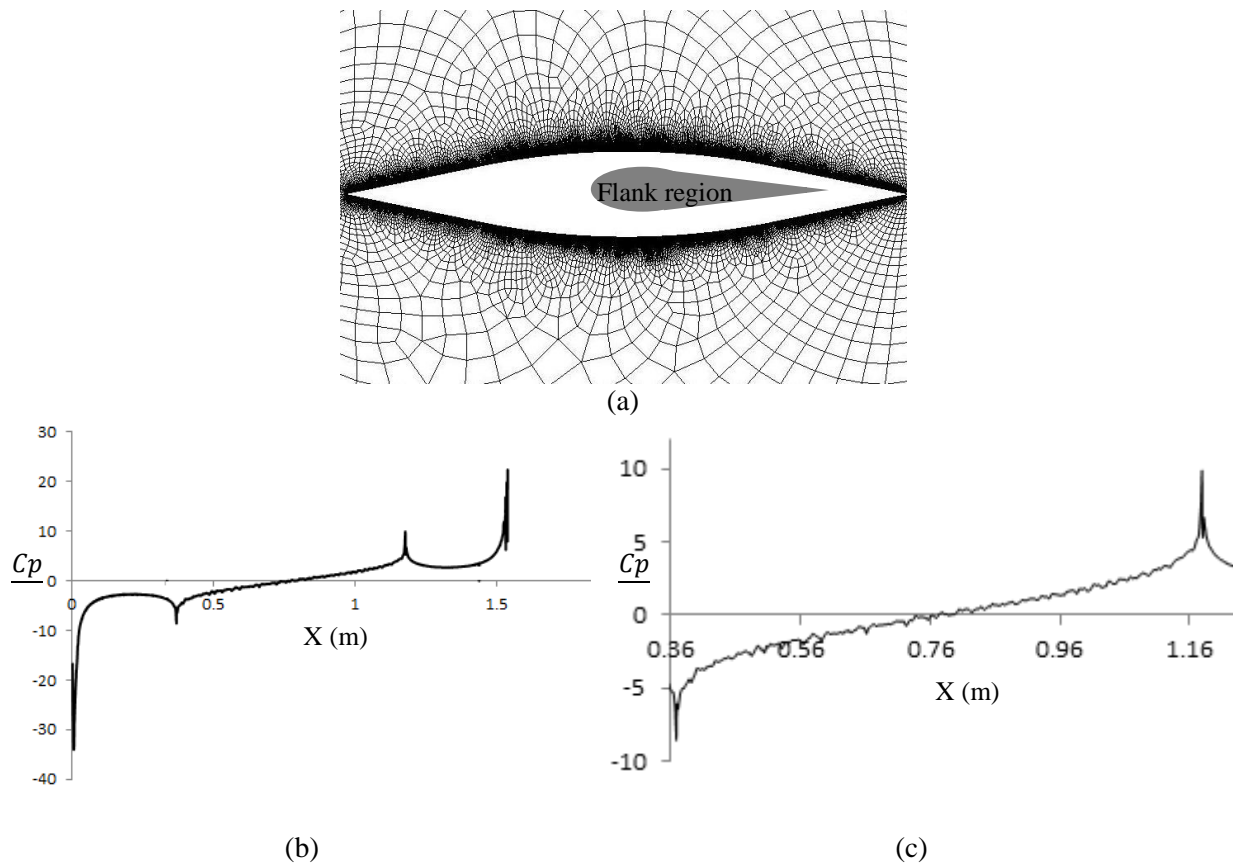


Figure 5.7: (a) Numerical model of shark body (shaded region is flank region), (b) pressure gradient along shark body, (c) pressure gradient along the flank region of shark body

### 5.3.3 Laminar Separation Control

#### 5.3.3.1 Time-averaged Velocity Field

The time-averaged velocity contours showed that for laminar flow ( $Re_{x=1.3 \times 10^5}$ ), the shark skin resulted in a reduction in size of the separation bubble as compared to a smooth plate under the same amount of APG (fig. 5.8 (a, b)). At a higher strength of APG, the separation bubble on the shark skin is again reduced in size (fig. 5.8 (b), fig 5.9 (b)). Fig. 5.9 shows the LSB region bounded by mean dividing streamline passing through the separation point. Then the separation point and transition point are identified on this velocity line. From table 5.1 it can be

seen that shark skin minimally delays the separation point, but induces earlier transition to reattach the flow thereby reducing the height and extent of the LSB.

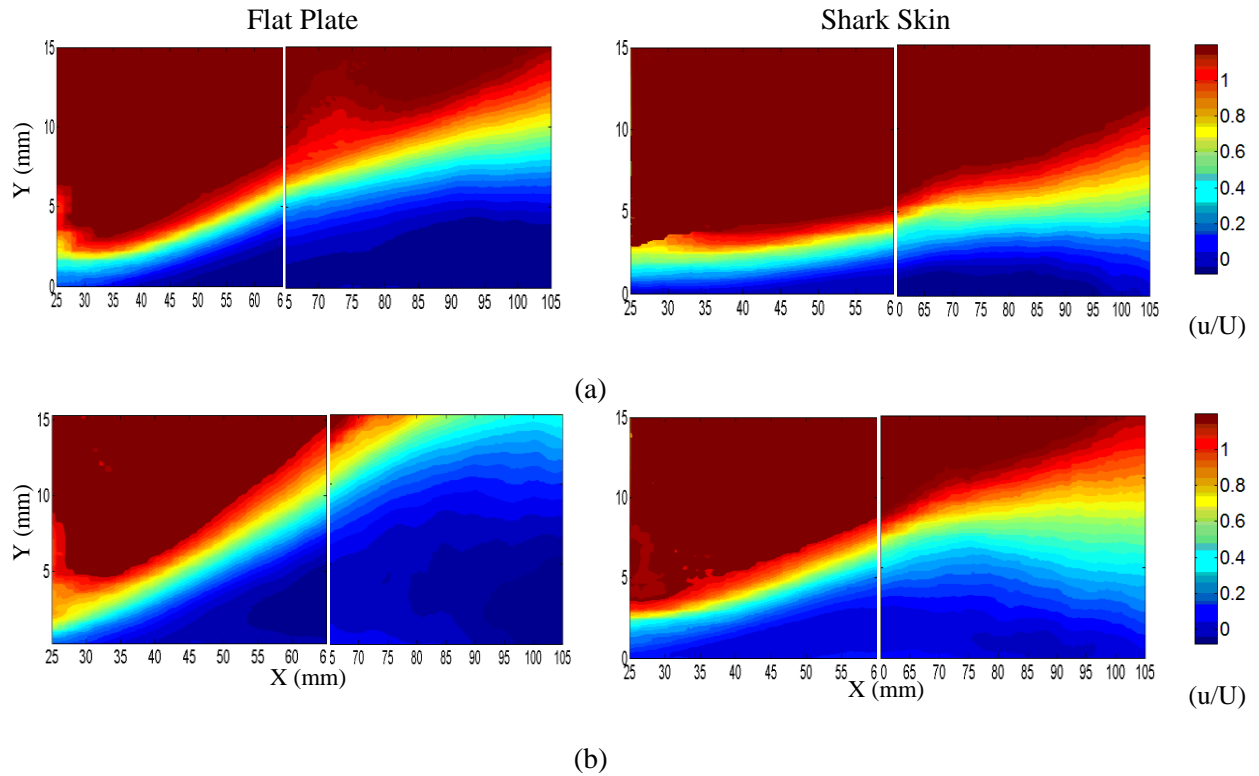


Figure 5.8: Time-averaged velocity contour for laminar flow separation at  $Re_x \approx 1.3 \times 10^5$  and at different amount of APG (a)  $VR = 1.208$ . (b)  $VR = 1.409$

It should be noted that LSB height ( $h$ ) is measured at the point of transition,  $T$ , after which height decreases due to turbulent mixing and eventual reattachment.

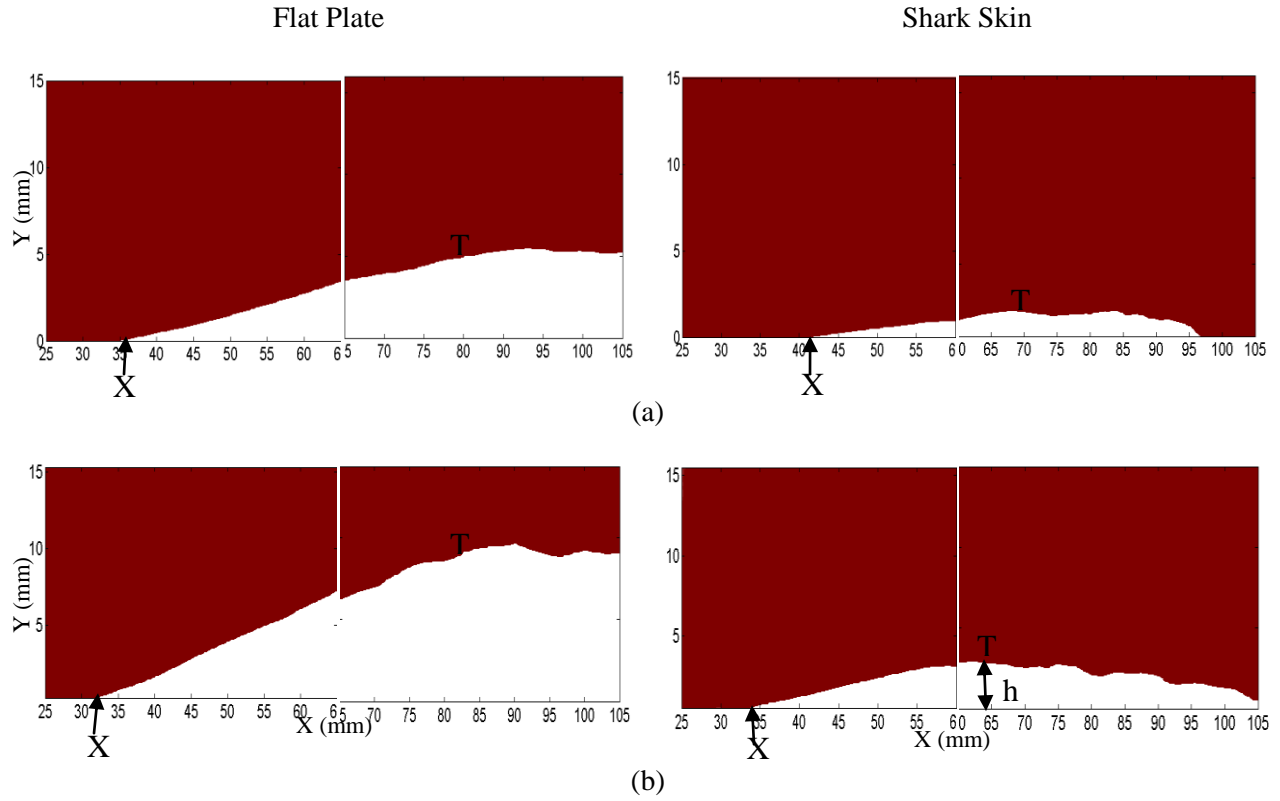


Figure 5.9: Comparison of separation point, transition point and LSB size between flat plate and shark skin at  $Re_x \approx 1.3 \times 10^5$  and at different amount of APG (a) VR = 1.208, (b) VR = 1.409

VR	Smooth Plate			Shark Skin		
	$X_S$	$X_T$	h	$X_S$	$X_T$	h
1.208	35	80	5.1	42	69	1.65
1.409	32	82	8.8	34	65	3.2

### 5.3.3.2 Time-averaged Vorticity Field

Fig. 5.10 shows the comparison of time-averaged vorticity field between the smooth plate and shark skin under same amount of APG. The separated laminar boundary layer forms a free shear layer outside the  $U = 0$  velocity line and contains the clockwise, negative vorticity from the original boundary layer flow. At this higher strength of APG, the shark skin lowers the extent to which the vorticity layer is pulled away from the wall as compared to that of smooth plate.

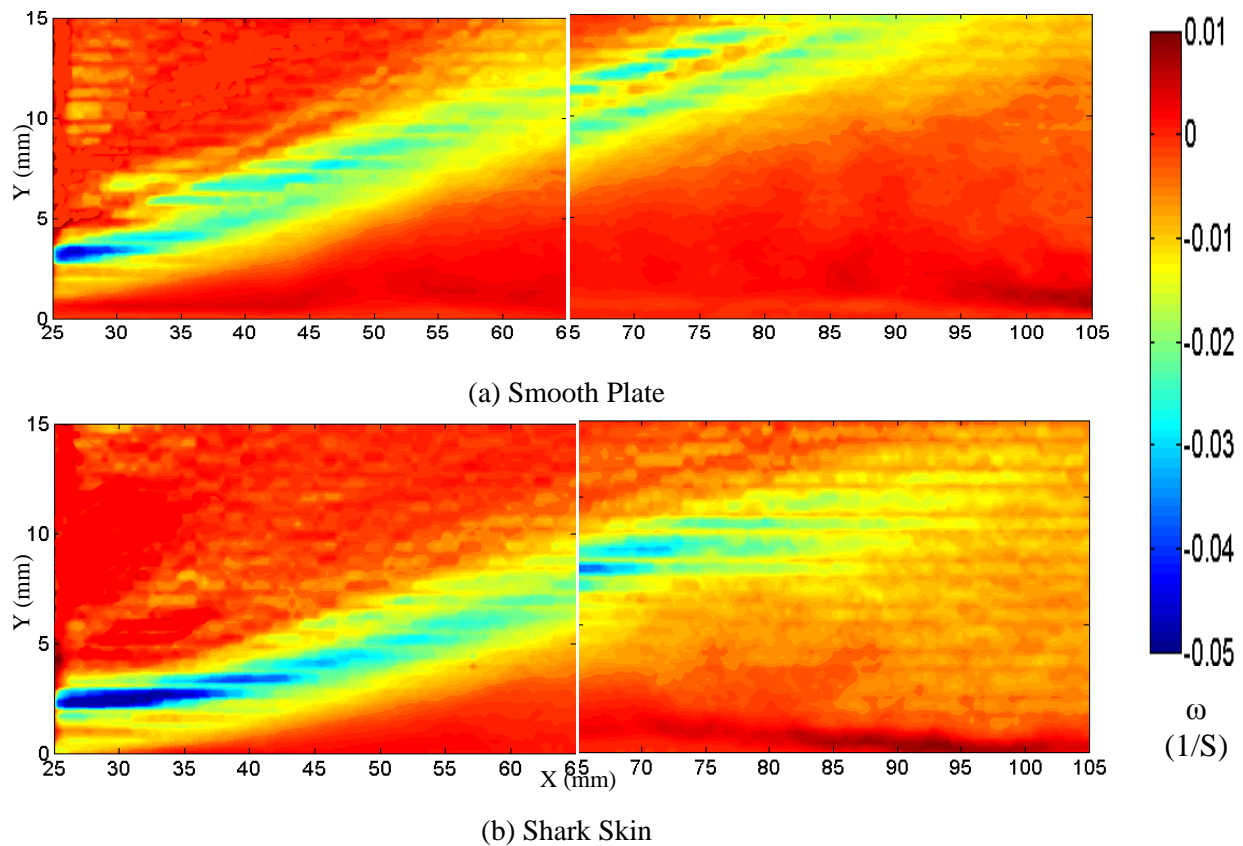


Figure 5.10: Time-averaged vorticity under same amount of APG,  $Re_x \approx 1.3 \times 10^5$  at  $VR = 1.409$

### 5.3.3.3 Reynolds Stress

One method to locate the turbulent transition point for a separation bubble is to measure the normalized Reynolds stress  $(-\frac{\overline{u'v'}}{U^2})$  where the starting point of turbulent transition, T in separated shear layers, is defined as the point where the normalized Reynolds stress  $(-\frac{\overline{u'v'}}{U^2})$  is more than 0.001 [24-27]. As such the contour levels of Reynolds stress above 0.001 are only shown in Fig. 5.11 (a, b). As seen in fig. 5.11, early transition takes place and higher Reynolds stress occurs for the shark skin cases. For a strong APG as presented in fig. 5.11 (b), shark skin results in comparatively higher Reynolds stress. As also seen in fig. 5.8 and fig. 5.9, shark skin controls the separation better for the stronger APG case. We thus hypothesize that there might be a threshold value of reverse flow for which shark skin bristling is actuated to better control flow separation; this threshold would be achieved more regularly for the higher APG case.

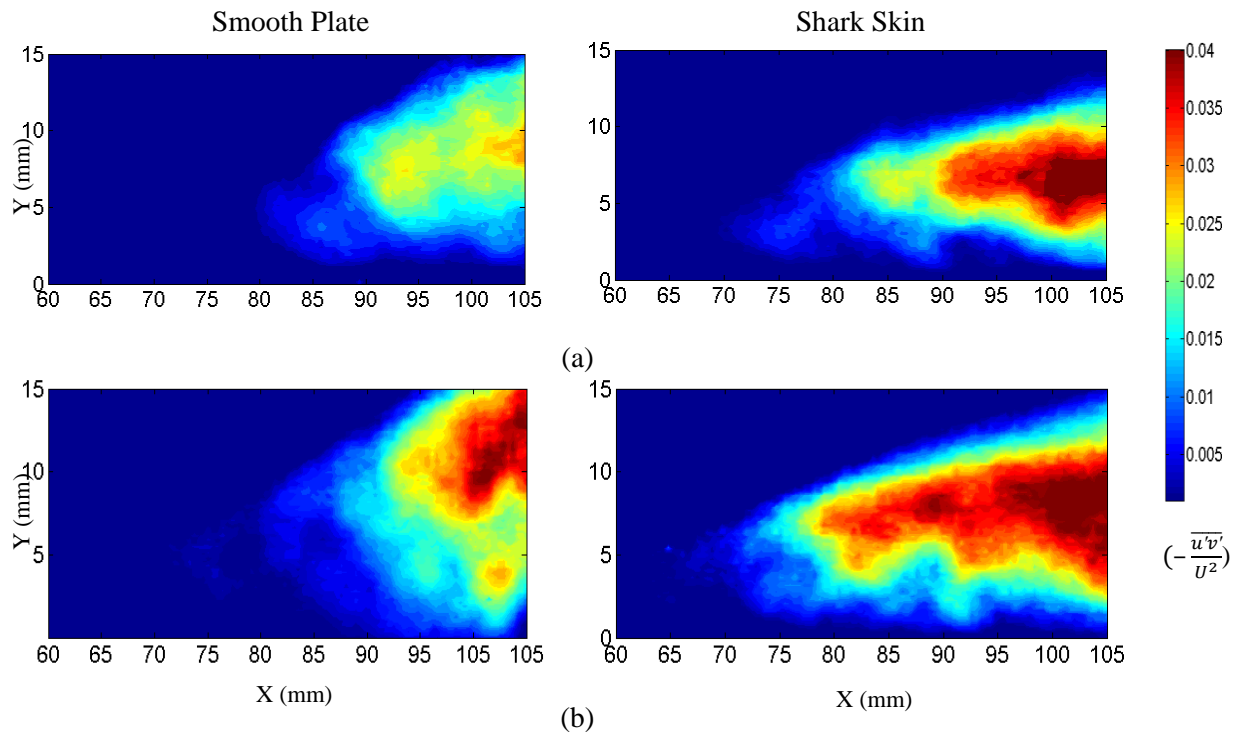


Figure 5.11: Time-averaged normalized Reynolds Stress  $(-\frac{\overline{u'v'}}{U^2})$  field for laminar flow at  $Re_x \approx 1.3 \times 10^5$  and at different amount of APG, (a)  $VR = 1.208$ , (b)  $VR = 1.409$

### 5.3.3.4 Instantaneous Velocity Field

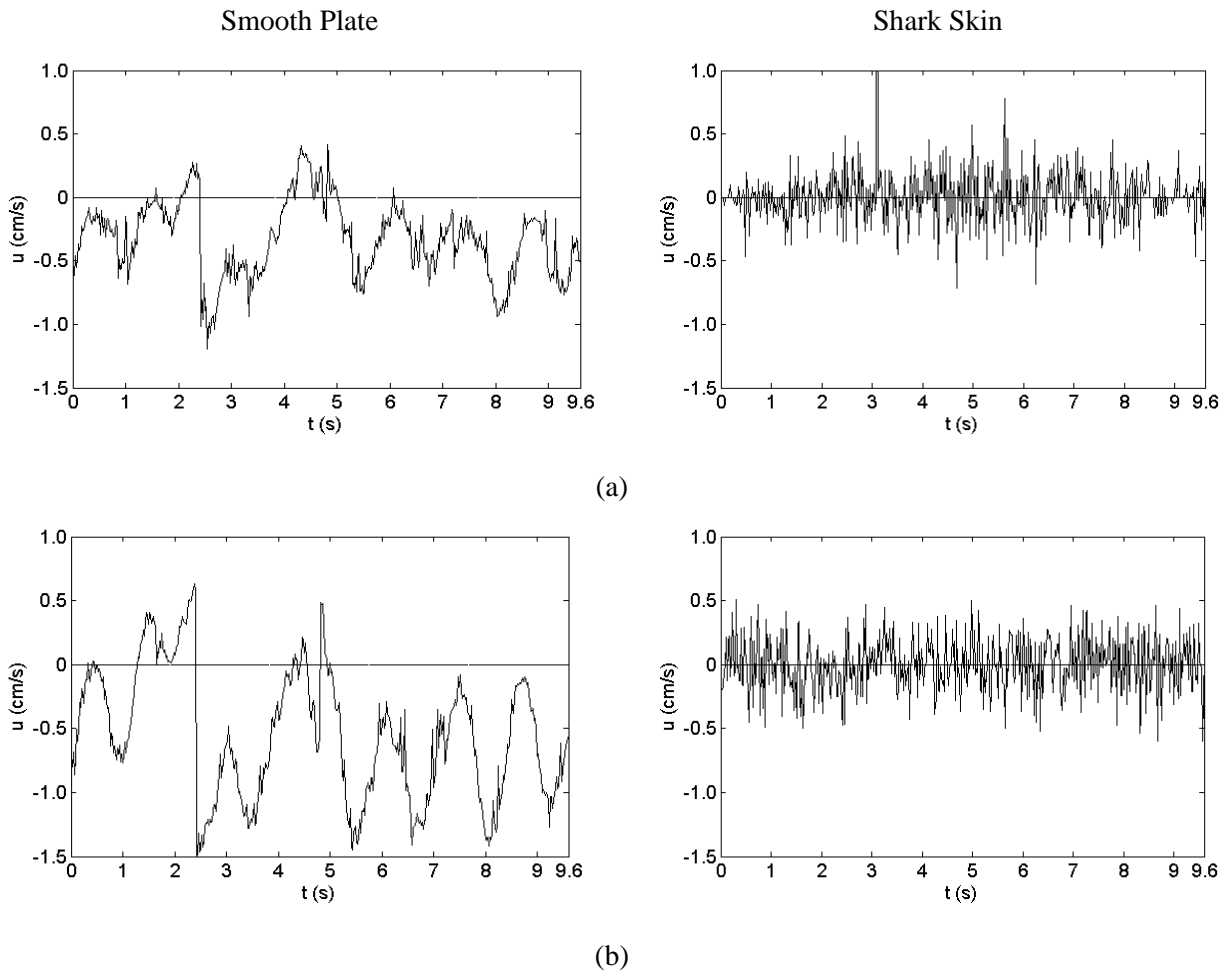


Figure 5.12: Instantaneous velocity history flat plate Vs shark skin for  $VR = 1.208$  at  $y = 2$  mm and at different X-positions (a)  $x = 45$  mm, (b)  $x = 70$  mm

The instantaneous velocity history gives more insight as to the laminar flow separation control of shark skin. The  $u$ -velocity history (for  $t = 9.6$  second) very near the wall ( $y = 2$  mm) at different  $x$  positions for two different magnitudes of APG are presented in figure 5.12 and figure 5.15. Here two  $x$ -locations are chosen: one just after the beginning of separation ( $x = 45$  mm) and the other near the transition zone of separation ( $x = 70$  mm). Fig. 5.12 (a) shows that the peak magnitudes of reverse flow velocity vary within  $-0.5$  cm/s to  $-1.2$  cm/s for the flat plate case, whereas for the shark skin cases, most of the peak reverse flow values are less than  $-0.5$

cm/s. In fig. 5.12 (b), the peak of reverse flow velocity varies within -0.5 to -1.5 cm/s for smooth plate cases. Here also the peak reverse flow value for shark skin surface does not exceed -0.5 cm/s.

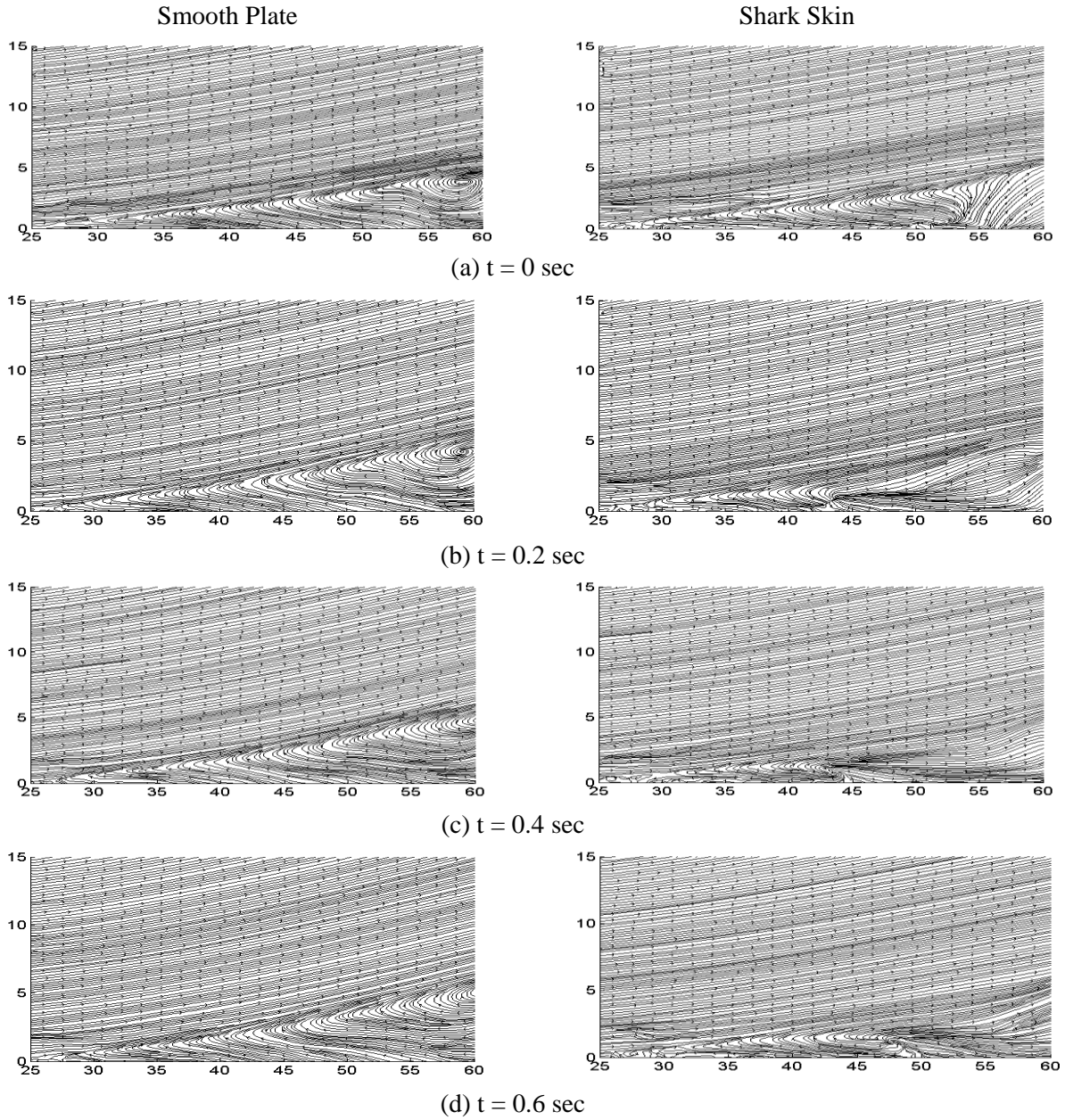


Figure 5.13. Instantaneous Flow Field for laminar flow under same amount of APG at  $VR = 1.409$  at upstream location of separation

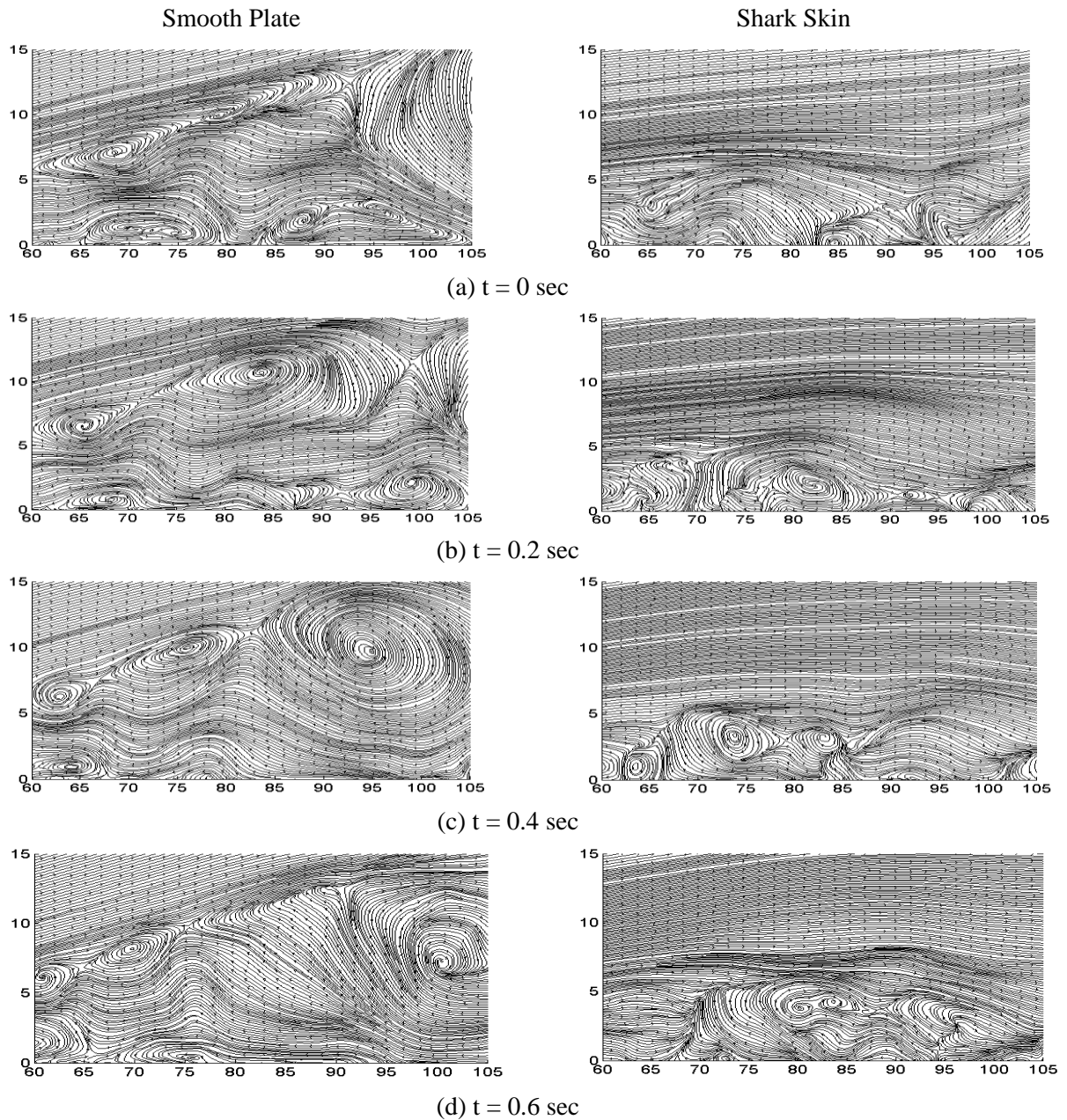


Figure 5.14. Instantaneous Flow Field for laminar flow under same amount of APG at  $VR = 1.409$  inside the separation region

For the smooth plate case, the instantaneous flow velocity shows that velocity is negative for most of the time. However, the shark skin causes a higher frequency of flow direction change and a lower peak value of backflow.

Fig. 5.13, 5.14 presents the instantaneous flow field for an interval of 0.2 seconds over a smooth and shark skin surface at a higher strength of APG. For the smooth plate, the instantaneous shape and size of the bubble does not change much with time. But for the shark skin surface, the instantaneous shape of the bubble is obviously changing with time. It starts with a large scale vortex structure that sheds off with a decrease in size of the separated region, and then the bubble starts growing in size.

Instantaneous flow velocity of shark skin under that higher strength of APG is also observed in fig. 5.15(a, b). At  $x = 45$  mm, the peak reverse flow goes up to  $-3$  cm/s for the smooth case. The amount of positive velocity increases for shark skin surface compare to the cases in fig. 5.12. But at  $x = 70$  mm, the reverse velocity peak goes as high as  $-5$  cm/s and it shows more control of separation. At this point, the velocity is remains positive for most of the time and the positive velocity peaks are higher in magnitude.

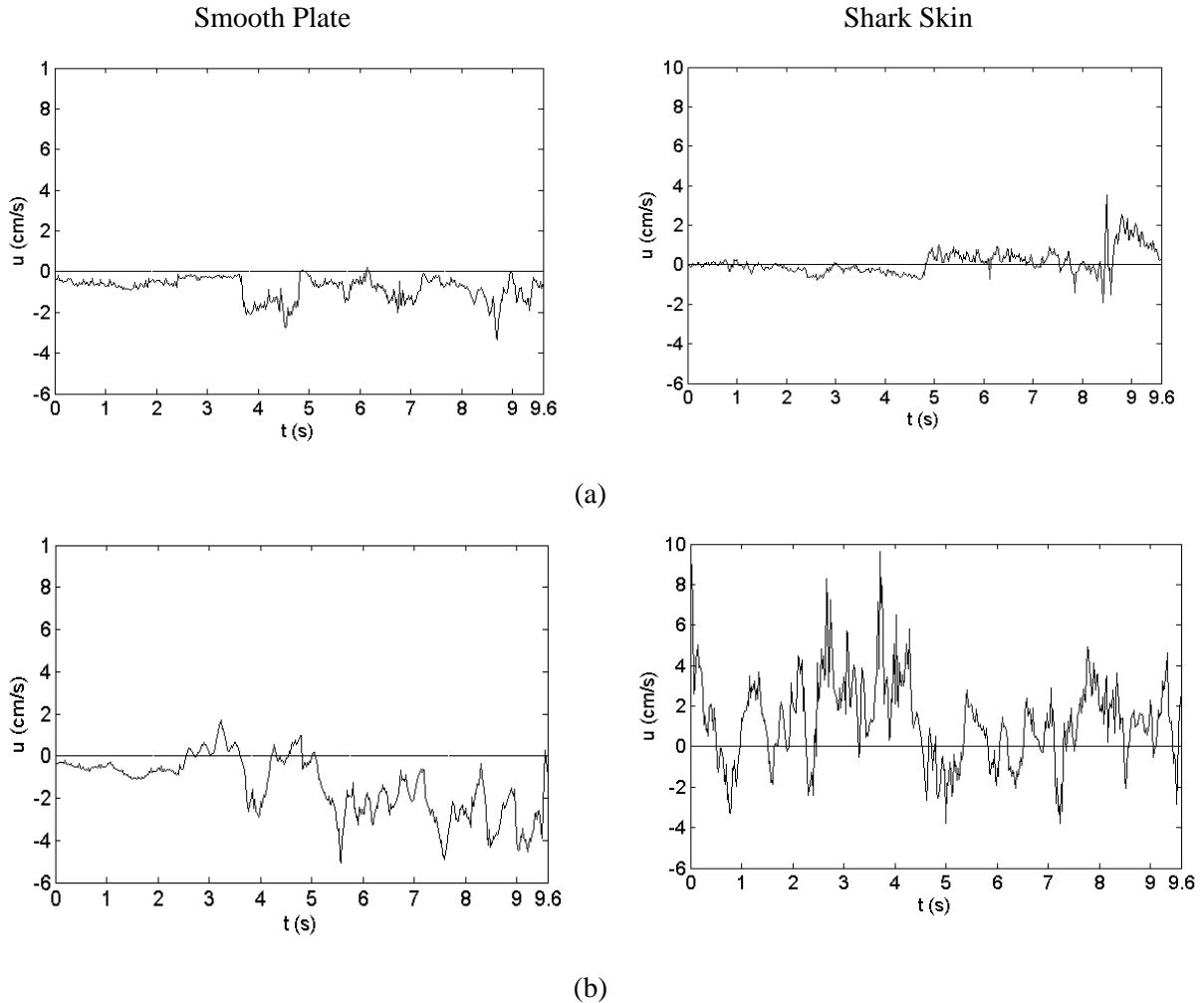


Figure 5.15: Instantaneous velocity history flat plate Vs shark skin for  $VR = 1.409$  at  $y = 2$  mm and at different X-positions (a)  $x = 45$  mm, (b)  $x = 70$  mm

The backflow coefficient ( $\gamma$ ) is a measurement of the percentage of time the flow is reversed. Figure 5.16 shows a reduction in the size of the backflow coefficient region on shark skin as compared to the smooth plate under the same amount of APG. Contours of backflow coefficient show that in the  $y$ -direction upwards from the wall, the amount of backflow increases to its maximum value and then start decreasing again. Also in the  $x$ -direction after a certain distance, the amount of backflow reaches a maximum value and then starts decreasing. Backflow contours also agree with the fact that the smooth wall case is steady laminar flow separation reaching 100% backflow in the front of the separation bubble, while the shark skin case is

unsteady. For the cases of shark skin, the maximum amount of backflow is lower than the smooth plate under the same APG. Also in the x-direction, the amount of backflow reaches to a maximum value earlier for shark skin cases and after that starts decreasing.

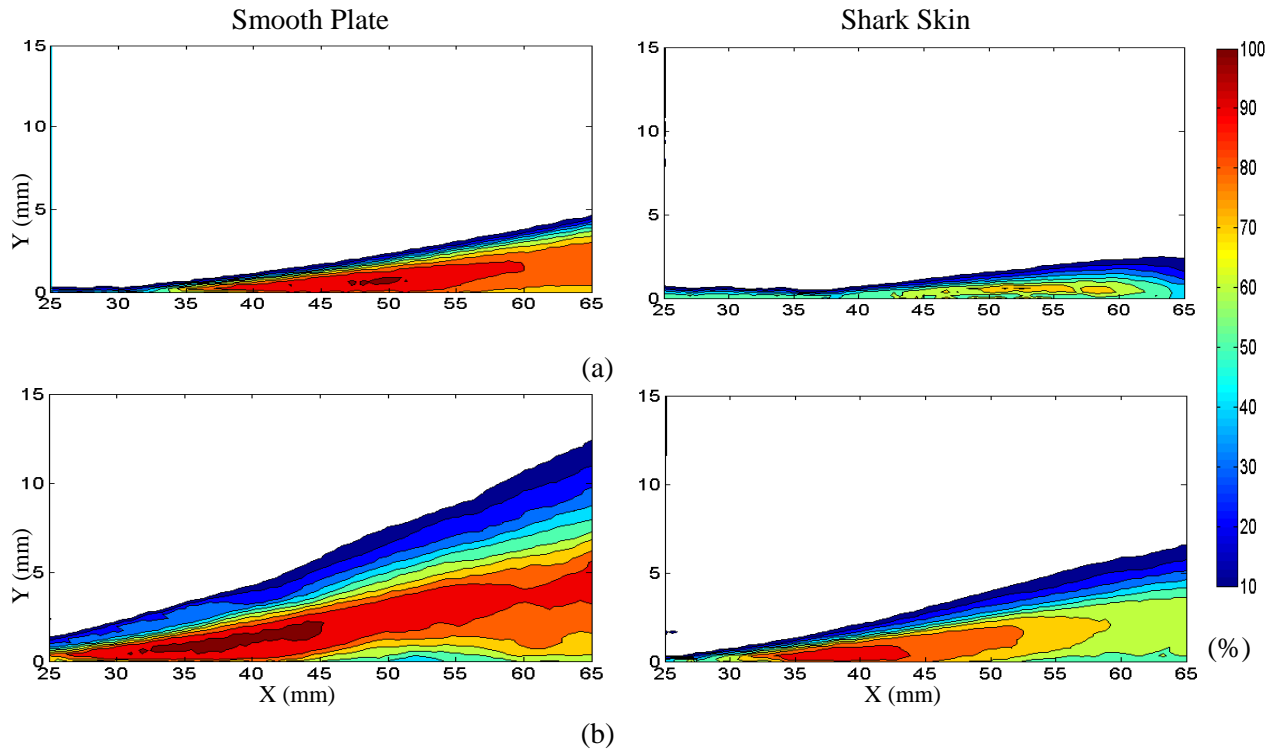


Figure 5.16: Contour of backflow coefficient of laminar flow under at  $Re_x \approx 1.3 \times 10^5$  and at different amount of APG, (a),  $VR = 1.209$ , (b)  $VR = 1.409$

### 5.3.4 Turbulent Separation Control

#### 5.3.4.1 Contour of Backflow Coefficient

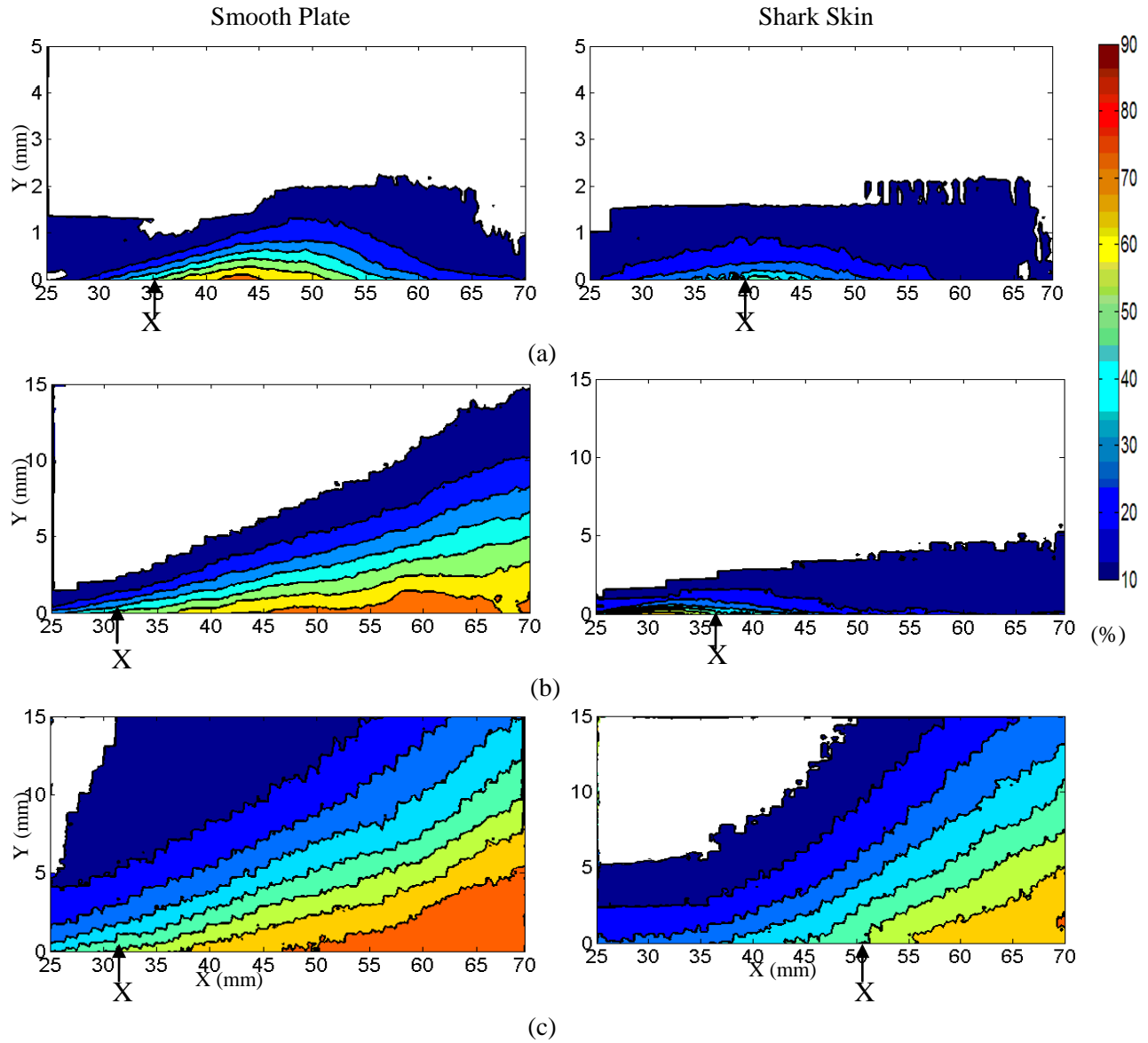


Figure 5.17: Contour of backflow coefficient of turbulent flow under at different amount of APG, (a)  $Re_x \approx 2.5 \times 10^5$ ,  $VR = 2.13$ , (b)  $Re_x \approx 2.5 \times 10^5$ ,  $VR = 2.66$ , and (c)  $Re_x \approx 3.0 \times 10^5$ , (b)  $VR = 3.10$

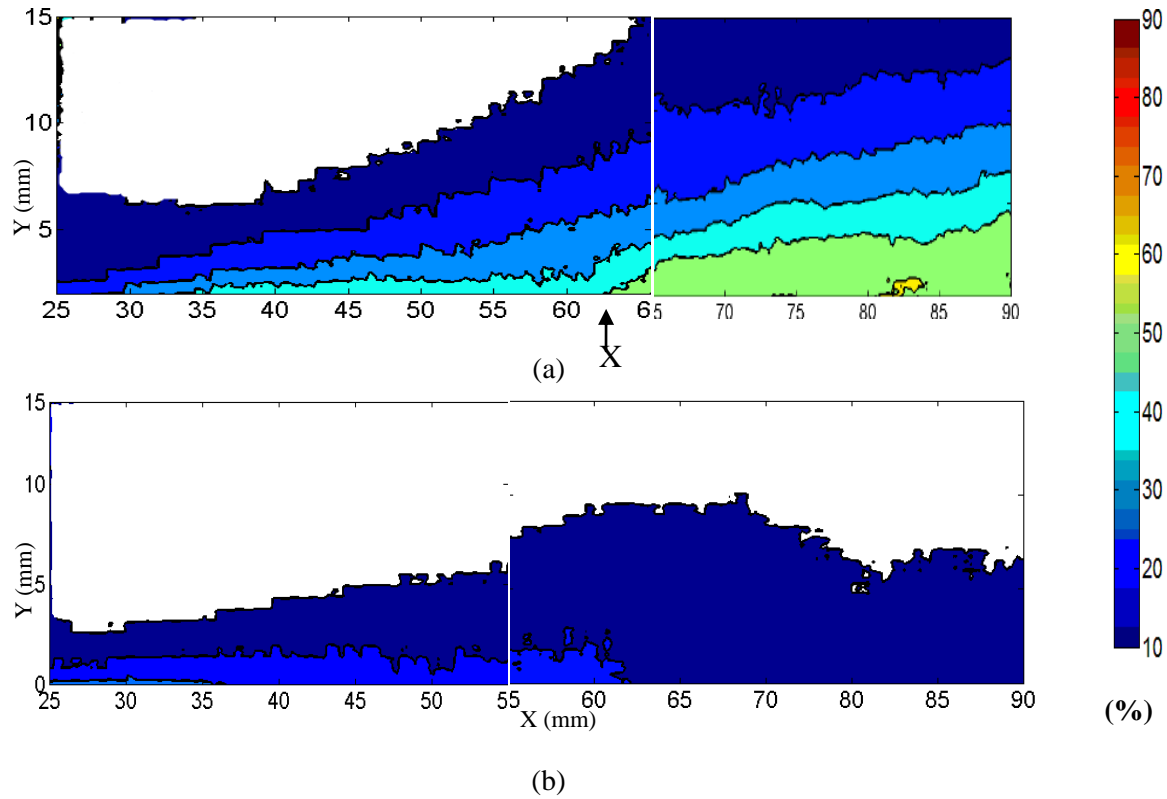


Figure 5.18: Contour of backflow coefficient of turbulent flow under at  $Re_x \approx 3.0 \times 10^5$  and at  $VR = 2.65$ , (a) smooth plate, (b) shark skin

Turbulent boundary layer separation is unsteady in nature and does not have a single stationary separation point like the smooth wall laminar separation bubble. The unsteady nature of separated flow forming in a turbulent boundary layer is evident by the contours of back-flow coefficient ( $\chi$ ) (fig. 5.17, 5.18). Quantitative definitions as to the detachment state near the wall can be defined based on this backflow [28-30]. The separation points defined are: incipient detachment (ID) which occurs where an instantaneous backflow 1% of the time ( $\chi = 0.01$ ) is measured; intermittent transitory detachment (ITD) occurs for an instantaneous backflow 20% of the time ( $\chi = 0.20$ ); finally detachment (D) occurs for an instantaneous backflow 50% of the time ( $\chi = 0.50$ ). The backflow coefficient contour shows that shark skin is capable of controlling turbulent separation. Shark skin reduces the size of the backflow coefficient region and results in

delayed separation as compared to a smooth plate under the same amount of APG. Detachment points ( $X_S$ ) for smooth plate and shark skins under different amounts of APG are listed in table 5.

2.

For the lower strength of APG (fig 5.17 (a)), the amount of backflow reaches as high as 70% on the smooth plate, whereas this value reduces to 50% for shark skin. At higher APG values (fig. 5.17 (b),(c), fig. 5.16 (b)) the shark skin gave better control of separation as the height of the backflow contour and the maximum percentage of backflow reduces significantly. Perhaps at a higher strength of APG, the boundary layer is induced to pull further away from the wall, but the higher magnitude of flow reversal may cause greater bristling of the shark scales thereby inducing greater separation control.

Table 5.2: Comparison of Turbulent Separation over flat plate and shark skin under different amount of APG			
		Smooth plate	Shark Skin
$Re_x$	VR	$X_S$	$X_S$
$2.5 \times 10^5$	2.13	35	40
	2.66	30	36
$3.0 \times 10^5$	2.65	62.5	
	3.1	31	51

### 5.3.4.2 Time-averaged Vorticity Field

The time-averaged vorticity field shows that shark skin gives better control under higher APG as shown in fig. 5.19 (b). For lower APG, there is less difference between the pulling of the boundary layer from shark skin as compared to the smooth plate. But at higher APG, the shark skin definitely controls the pulling away of the boundary layer from the wall.

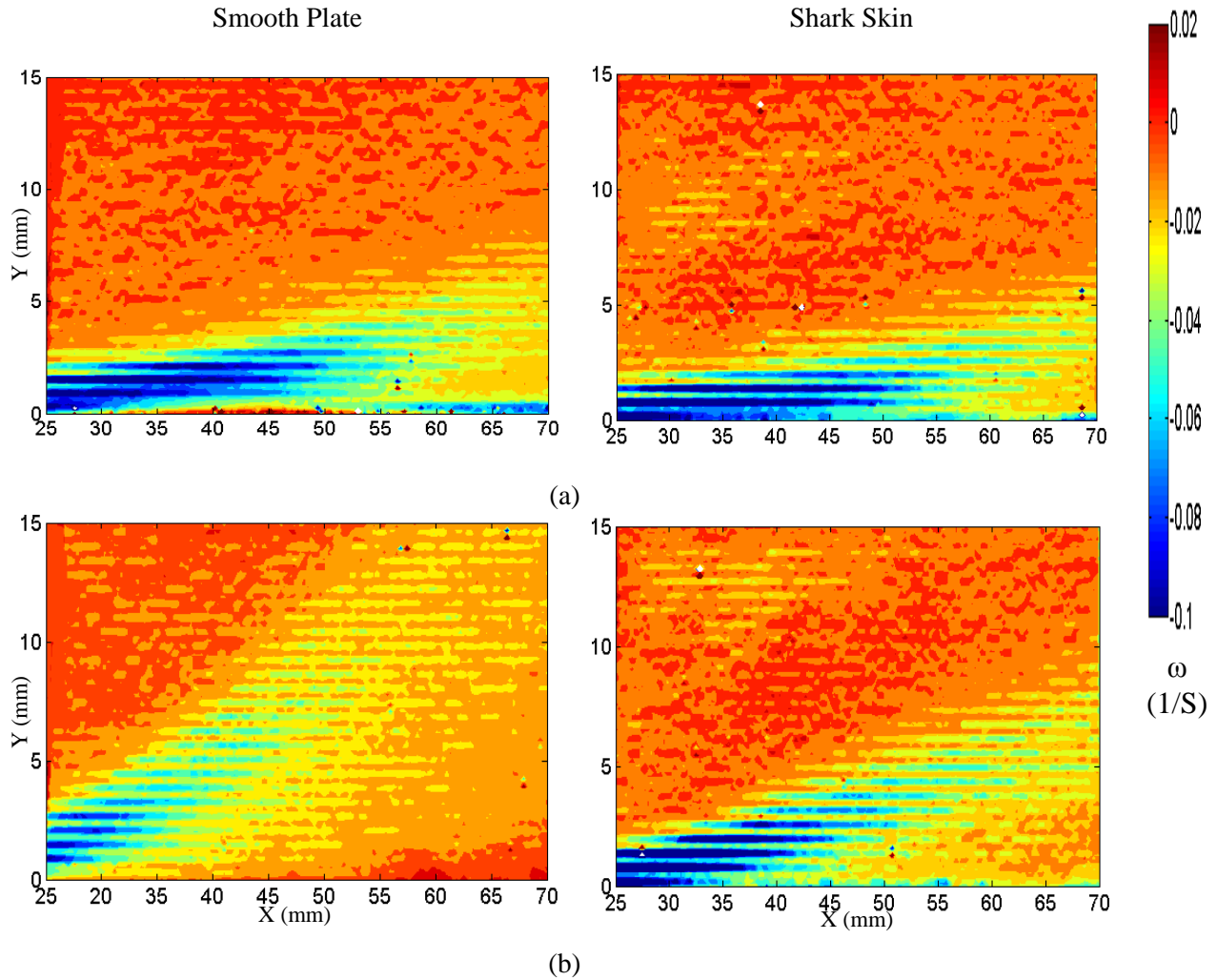


Figure 5.19: Time-averaged vorticity field under at different amount of APG, (a)  $Re_x \approx 2.5 \times 10^5$ ,  $VR = 2.13$ , (b)  $Re_x \approx 2.5 \times 10^5$ ,  $VR = 2.66$

### 5.3.4.3 Time-averaged Velocity Field

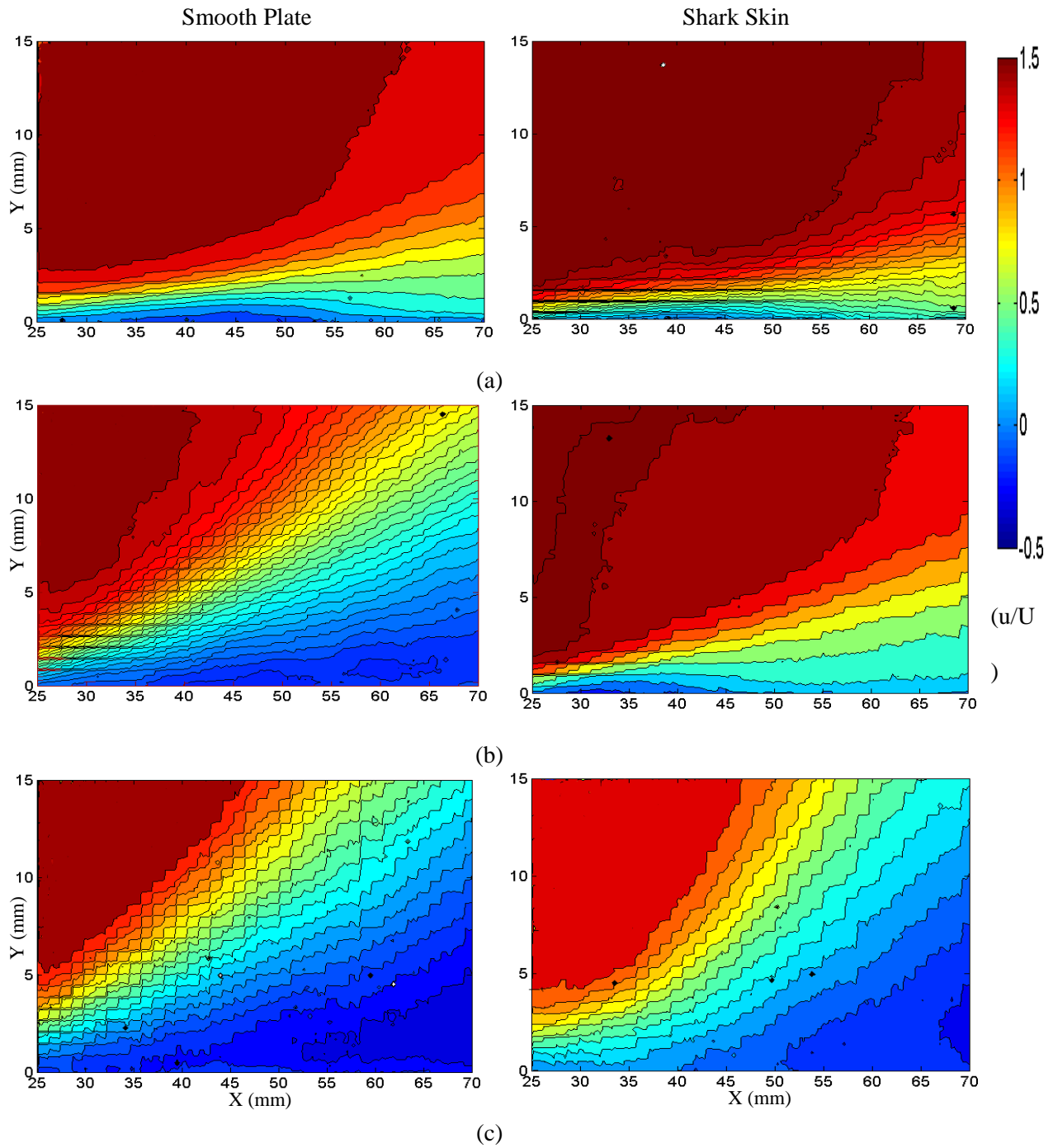


Figure 5.20: Time-averaged velocity ( $u/U$ ) contour for turbulent flow separation at different amount of APG (a)  $Re_x \approx 2.5 \times 10^5$ ,  $VR = 2.13$ , (b)  $Re_x \approx 2.5 \times 10^5$ ,  $VR = 2.66$ , and (c)  $Re_x \approx 3.0 \times 10^5$ ,  $VR = 3.10$

Turbulent separation is very unsteady in nature and a time-averaged mean flow analysis will not reveal the unsteady, instantaneous flow behavior of the separation bubble [31]. But if the velocity fields can be accurately averaged then it can give a steady separation bubble. From TR-DPIV analysis the time-averaged velocity are shown in Fig. 5.20. The height of the negative stream wise velocity zone of turbulent separation over the shark skin is smaller than that of the smooth plate for different amounts of APG. For higher strength of APG (fig. 5.20 (b), 5.20 (c)), a significant reduction in the size of the negative velocity region was observed.

#### 5.3.4.4 Instantaneous Velocity Field

Figure 5.21 show the instantaneous velocity history of a point very close to the wall under different strengths of APG. As the APG increases, the peak of negative flow velocity increase from -0.1 m/s to -0.35 m/s for the smooth case. And as the magnitude of APG increases, shark skin results in better control of turbulent boundary layer separation. It can be also seen for the shark skin surface under various amount of APG in fig. 5.21 that the periods of backflow are much shorter in duration with lower peak magnitudes, resulting in a significantly smaller total time of reversal. As the shark skin is subjected to an increased strength of APG, the reversed flow region is further reduced from reaching a higher magnitude thereby controlling flow separation.

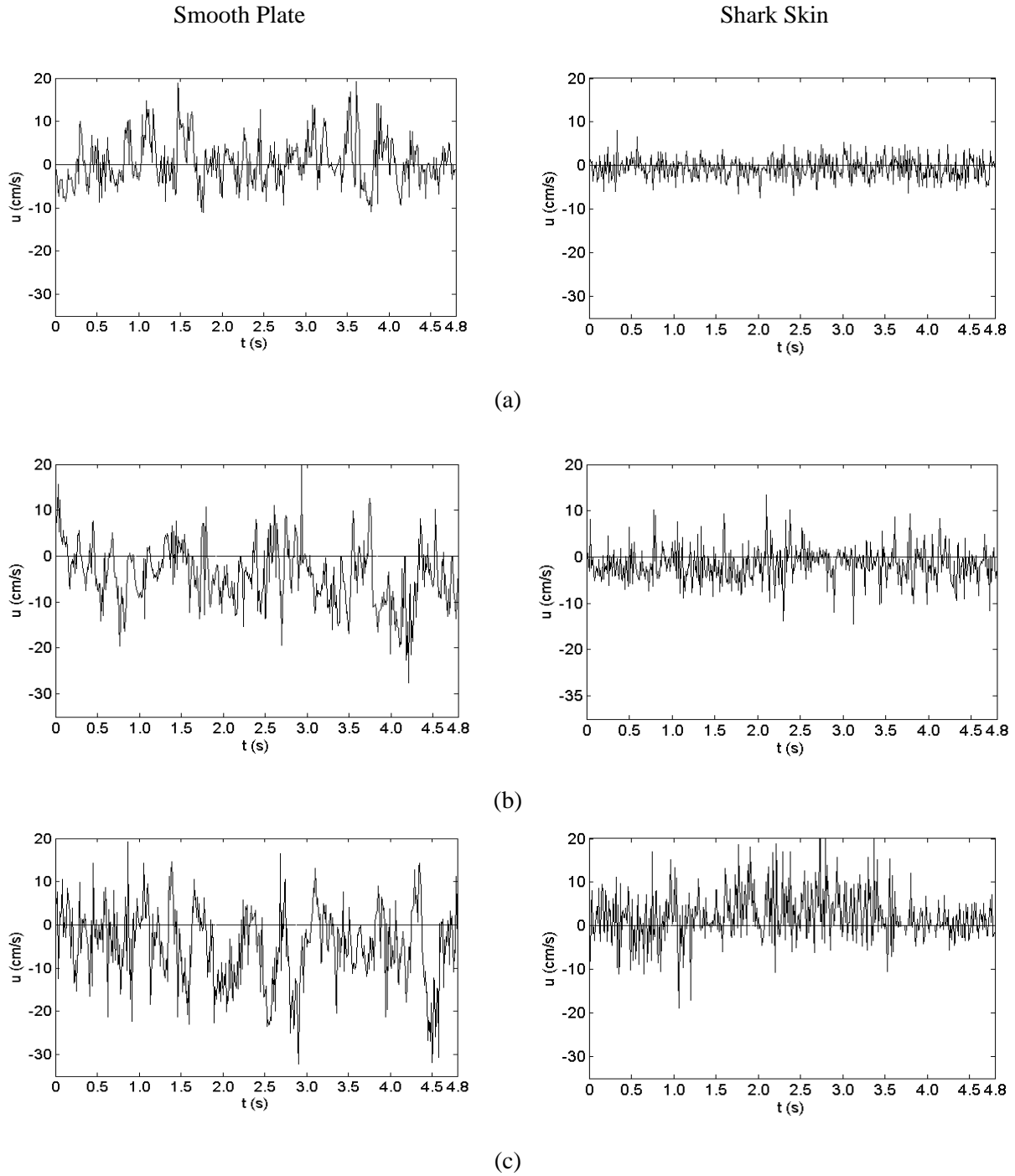


Figure 5.21: Instantaneous velocity history inside the turbulent separation region flat plate Vs shark skin for  $y = 2$  mm and  $x = 45$  mm, (a)  $Re_x \approx 2.5 \times 10^5$ ,  $VR = 2.13$  (b)  $Re_x \approx 2.5 \times 10^5$ ,  $VR = 2.66$  (c)  $Re_x \approx 3.0 \times 10^5$ ,  $VR = 3.10$

### 5.3.4.5 Time-averaged Reynolds Stress Profiles

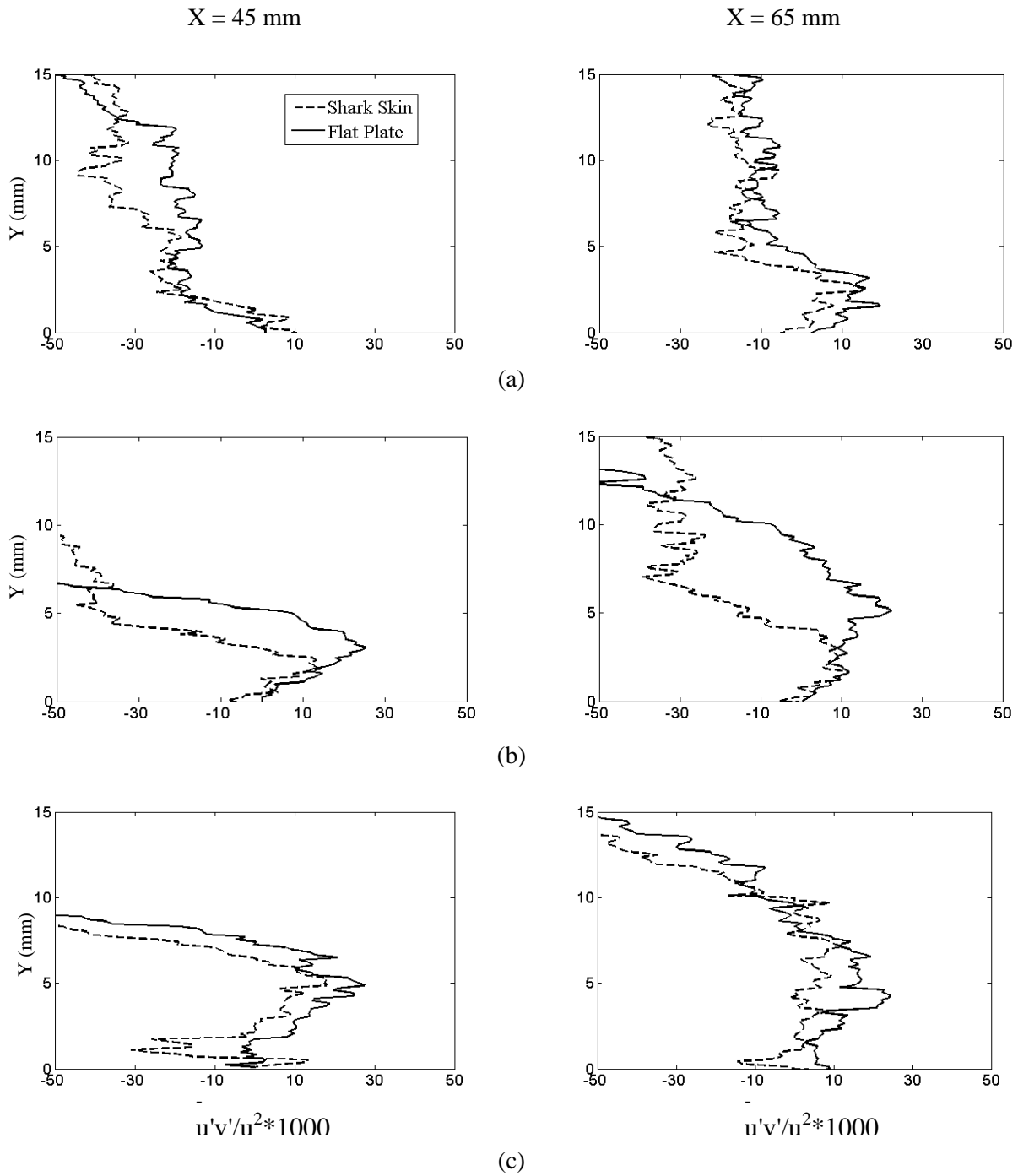


Figure 5.22: Time-averaged Reynolds stress profile under at different amount of APG, (a)  $Re_x \approx 2.5 \times 10^5$ ,  $VR = 2.13$ , (b)  $Re_x \approx 2.5 \times 10^5$ ,  $VR = 2.66$ , and (c)  $Re_x \approx 3.0 \times 10^5$ ,  $VR = 3.10$

Time-averaged Reynolds stress profiles for two different x-positions under three different strengths of APG are presented in fig. 5.22. At the beginning of the separation bubble (fig. 5.22 (a)), the peak of Reynolds stress close to wall is slightly higher for the shark skin as compared to the smooth plate. But inside the separation bubble (fig. 5.22 (b)), the peak of Reynolds stress close to the wall for the smooth plate is always higher than that of shark skin.

#### 5.4 Summary

As the cavity Reynolds number is very low in the present experimental studies, turbulent mixing in and out of the cavities formed between the bristled scales may not be induced. Thus the primary mechanism of flow control is hypothesized to be the scale bristling inhibiting flow reversal. The shark skin also caused earlier transition to turbulence in the laminar separation bubble. The instantaneous flow velocity shows that for the shark skin case, the laminar point of flow separation is unsteady. This unsteady behavior may be because of the shark skin inhibiting the flow reversal near the wall. In the cases of the turbulent boundary layer separation, the reverse shear is hypothesized to erect the scales and the bristled scales obstruct the reversing flow reducing the overall backflow coefficient while Re stress levels remains similar for both cases. Thus even for turbulent flow, turbulent mixing induced by the presence of the scales may not be present in this experiment as a key mechanism to control the flow separation. Rather the reversed flow bristles the shark scales, inhibits backflow and thus prevents the reverse flow from reaching higher magnitudes.

## 5.5 Ecological Ramifications of Separation Control

This section describes some of the biological and morphological characteristics of Mako shark that support faster swimming capability in addition to the separation control mechanisms of the bristling skin.

The Shortfin Mako (*Isurus oxyrinchus*) is a slow-growing and late-maturing oceanic species with fusiform body shape. Mako sharks have a birth size ranging from 60 to 70 cm and are estimated to have a maximum total length of 408 cm [32]. Male specimens can reach about 298 cm long whereas the mature female specimens can exceed a length of 390 cm [32].

The Shortfin Mako is an extremely active epipelagic species, found circumglobally in all warm-temperate and tropical seas from about 50° N to 50° S [32, 33, 34, 35]. It generally inhabits offshore waters, far from land and as deep as 500 m. Typically it is found in regions where water temperature lies between 17° to 22° C [32, 36]. They are regularly seen in the western Atlantic, spanning from Northern Argentina to the Gulf of Maine including the Caribbean, Gulf of Mexico and Bermuda. In the eastern Atlantic they are found in the Mediterranean and to the west of Sahara and even close to South Africa [32, 37].

Makos' are the fastest swimming species of shark with an estimated maximum burst speed of 4000 cm/s or 144 km/h for a 400 cm long specimen [9]. Assuming an advancement of ten body lengths per second [38], a 200 cm long shark can achieve a burst speed of about 2000 cm/s or 72 km/h. They are also capable of jumping as high as 9 m from the water surface with an estimated escape velocity of 9.8 m/s. [9]. Experiments inside a large water tunnel have revealed that a 180 cm long Mako shark can swim with an average speed of 90 cm/s over a 24 hour period [39].

Most sharks and fishes are ectothermic, matching their body temperature with the surrounding water temperature. The Shortfin Mako (*Isurus oxyrinchus*) is endothermic, capable of elevating its body temperature 7-10°C above ambient temperatures by conserving metabolic heat. This elevated temperature helps the Shortfin Mako obtain the extra power needed for high-speed swimming [40, 41-45]. Another important difference between the Shortfin Mako shark and ectothermic fishes is the internalized location of red muscle (known as RM), helping the shark sustain a higher aerobic swimming metabolism as well as increased burst swimming capability [41]. Research on the physiological properties of the Shortfin Mako's swimming muscles have shown that the RM has shorter activation and relaxation times, allowing the muscles to produce more net positive work at a greater cycle frequency [45]. The endothermic property of this shark also allows them to dive into colder water and feed, thereby expanding their feeding niche [46].

Apart from the muscular physiology, Mako sharks have morphological adaptations for high speed swimming. For instance, they possess a conical snout, large gills for efficient gas exchange, streamlined body and a lunate shaped, high aspect ratio caudal fin [43]. The high aspect ratio tail produces maximum thrust with minimum drag to provide most of the propulsion needed for their thunniform locomotion [47]. This form of locomotion is one of the fastest swimming patterns where less than one-third of the rear body-length is subject to oscillation [48]. These adaptations for speed allow the Mako shark to feed on other fast moving species such as tunas, swordfish, porpoise and other sharks [32, 49]. In addition, they also feed upon cephalopods, bony fishes (like mackerels), and occasionally sea turtles and seabirds [32].

In brief, the unique endothermic and morphological characteristics, coupled with the separation control mechanisms aided by the flexible flank scales, facilitate drag reduction and faster swimming speeds for Mako sharks.

## 5.6 Conclusions

Shortfin Mako shark skin from the flank region with highly flexible scales was tested under various amounts of APG for its separation control capability. The time-averaged DPIV results showed that shark skin is capable of controlling both laminar and turbulent separation. Shark skin results in a smaller separation region and a delay in the separation point under different magnitudes of APG. Instantaneous velocity history also reveals that for a higher strength of APG, shark skin results in better separation control in both laminar and turbulent flow cases.

## Acknowledgement

Support under NSF grant 0932352 is gratefully acknowledged. First author Farhana Afroz was also supported by a scholarship through the Alabama EPSCoR Graduate Research Scholars Program.

## References

1. Raschi, W., & Tabit, C. (1992). Functional aspects of placoid scales: a review and update. *Marine and Freshwater Research*, 43(1), 123-147.
2. Bechert, D. W., Bruse, M., Hage, W., Van der Hoeven, J. T., & Hoppe, G. (1997). Experiments on drag-reducing surfaces and their optimization with an adjustable geometry. *Journal of Fluid Mechanics*, 338(1), 59-87.
3. Bechert, D. W., Bruse, M., Hage, W., & Meyer, R. (2000). Fluid mechanics of biological surfaces and their technological application. *Naturwissenschaften*, 87(4), 157-171.
4. Bechert, D. W., Bruse, M., & Hage, W. (2000). Experiments with three-dimensional riblets as an idealized model of shark skin. *Experiments in fluids*, 28(5), 403-412.
5. Zhao, D. Y., Huang, Z. P., Wang, M. J., Wang, T., & Jin, Y. (2012). Vacuum casting replication of micro-riblets on shark skin for drag-reducing applications. *Journal of Materials Processing Technology*, 212(1), 198-202.
6. Bixler, G. D., & Bhushan, B. (2012). Shark skin inspired low-drag microstructured surfaces in closed channel flow. *Journal of colloid and interface science*.
7. Bechert, D. W., Hoppe, G., & Reif, W. E. (1985). On the drag reduction of the shark skin. In *1985 AIAA Shear Flow Control Conference*.
8. Lin, J. C. (2002). Review of research on low-profile vortex generators to control boundary-layer separation. *Progress in Aerospace Sciences*, 38(4), 389-420.
9. Motta, P., Habegger, M. L., Lang, A., Hueter, R., & Davis, J. (2012). Scale morphology and flexibility in the Shortfin Mako *Isurus oxyrinchus* and the blacktip shark *Carcharhinus limbatus*. *Journal of morphology*, 273(10), 1096-1110.
10. Lang, A., Motta, P., Habegger, M. L., Hueter, R., & Afroz, F. (2011). Shark skin separation control mechanisms. *Marine Technology Society Journal*, 45(4), 208-215.
11. Lang, A., Motta, P., Habegger, M. L., & Hueter, R. (2012). Shark Skin Boundary Layer Control. In *Natural Locomotion in Fluids and on Surfaces* (pp. 139-150). Springer New York.

12. Bushnell, D. M. (1983). Turbulent drag reduction for external flows. *AIAA paper*, 227, 1983.
13. Howard, F. G., & Goodman, W. L. (1985). Axisymmetric bluff-body drag reduction through geometrical modification. *Journal of aircraft*, 22(6), 516-522.
14. Lang, A. W., Motta, P., Hidalgo, P., & Westcott, M. (2008). Bristled shark skin: a microgeometry for boundary layer control?. *Bioinspiration & biomimetics*, 3(4), 046005.
15. Oeffner, J., & Lauder, G. V. (2012). The hydrodynamic function of shark skin and two biomimetic applications. *The Journal of Experimental Biology*, 215(5), 785-795.
16. Lang, A. W., Bradshaw, M. T., Smith, J. A., & Motta, P. J., Habegger, L. & Hueter, R. E., Shark skin as a passive flow-actuated mechanism for controlling flow separation and reducing pressure drag, PNAS (under review)
17. Afroz, F., Lang, A., & Jones, E., Using a Rotating Cylinder to Induce a Laminar Separation Bubble over a Flat Plate, *European Journal of Mechanics B/Fluids* (under review)
18. Afroz, F., Lang, A., & Jones, E., Experimental Study of Turbulent Boundary Layer Separation over a Flat Plate Induced by a Rotating Cylinder, *European Journal of Mechanics B/Fluids* (under review)
19. Hart, D. P. (2000). PIV error correction. *Experiments in fluids*, 29(1), 13-22.
20. Willert, C. E., & Gharib, M. (1991). Digital particle image velocimetry. *Experiments in fluids*, 10(4), 181-193.
21. Huang, H., Dabiri, D., & Gharib, M. (1997). On errors of digital particle image velocimetry. *Measurement Science and Technology*, 8(12), 1427.
22. Howarth, L. (1938). On the solution of the laminar boundary layer equations. *Proceedings of the Royal Society of London. Series A, Mathematical and Physical Sciences*, 164(919), 547-579.
23. Prandtl, L. (1963). *The essentials of fluid dynamics*. Blackie & Son Limited.
24. Hu, H., & Yang, Z. (2008). An experimental study of the laminar flow separation on a low-Reynolds-number airfoil. *Journal of Fluids Engineering*, 130(5), 51101.

25. Volino, R. J., & Hultgren, L. S. (2001). Measurements in separated and transitional boundary layers under low-pressure turbine airfoil conditions. *Journal of Turbo machinery*, 123(2), 189-197.
26. Ol, M. V., McAuliffe, B. R., Hanff, E. S., Scholz, U., & Kähler, C. (2005). Comparison of laminar separation bubble measurements on a low Reynolds number airfoil in three facilities. *AIAA paper*, 5149(1), 2005.
27. Burgmann, S., Brücker, C., & Schröder, W. (2006). Scanning PIV measurements of a laminar separation bubble. *Experiments in Fluids*, 41(2), 319-326.
28. Simpson, R. L. (1996). Aspects of turbulent boundary-layer separation. *Progress in Aerospace Sciences*, 32(5), 457-521.
29. Simpson, R. L., Chew, Y. T., & Shivaprasad, B. G. (1981). The Structure of a Separating Turbulent Boundary Layer. Part 1. Mean Flow and Reynolds Stresses. *Journal of Fluid Mechanics*, 113, 23-51.
30. Simpson, R. L., Chew, Y. T., & Shivaprasad, B. G. (1981). The structure of a separating turbulent boundary layer. Part 2. Higher-order turbulence results. *Journal of Fluid Mechanics*, 113(1), 53-73.
31. Na, Y., & Moin, P. (1998). Direct numerical simulation of a separated turbulent boundary layer. *Journal of Fluid Mechanics*, 374(1), 379-405.
32. Compagno, L. J. (1984). *Sharks Of The World Vol 4 Part 2*.
33. Campana, S. E., Joyce, W., Marks, L., Natanson, L. J., Kohler, N. E., Jensen, C. F., ... & Myklevoll, S. (2002). Population dynamics of the porbeagle in the northwest Atlantic Ocean. *North American Journal of Fisheries Management*, 22(1), 106-121.
34. Natanson, L. J., Kohler, N. E., Ardizzone, D., Cailliet, G. M., Wintner, S. P., & Mollet, H. F. (2006). Validated age and growth estimates for the Shortfin Mako, *Isurus oxyrinchus*, in the North Atlantic Ocean. In *Special Issue: Age and Growth of Chondrichthyan Fishes: New Methods, Techniques and Analysis* (pp. 367-383). Springer Netherlands.
35. Bishop, S. D. H., Francis, M. P., Duffy, C., & Montgomery, J. C. (2006). Age, growth, maturity, longevity and natural mortality of the Shortfin Mako shark (*Isurus oxyrinchus*) in New Zealand waters. *Marine and Freshwater Research*, 57(2), 143-154.

36. Campana, S. E., Marks, L., & Joyce, W. (2005). The biology and fishery of Shortfin Mako sharks (*Isurus oxyrinchus*) in Atlantic Canadian waters. *Fisheries Research*, 73(3), 341-352.
37. Fowler, G. M. and Campana, S. E. (2009). Commercial by-catch rates of Shortfin Mako (*Isurus oxyrinchus*) from longline fisheries in the Canadian Atlantic. *ICCAT* 64:1650-1667.
38. Blake RW. (1983). *Fish Locomotion*. Cambridge: Cambridge University Press. 208 p.
39. Block, B. A., Booth, D., & Carey, F. G. (1992). Direct measurement of swimming speeds and depth of blue marlin. *Journal of Experimental Biology*, 166(1), 267-284.
40. Carey, F. G., & Teal, J. M. (1969). Mako and porbeagle: warm-bodied sharks. *Comparative biochemistry and physiology*, 28(1), 199-204.
41. Bernal, D., Donley, J. M., Shadwick, R. E., & Syme, D. A. (2005). Mammal-like muscles power swimming in a cold-water shark. *Nature*, 437(7063), 1349-1352.
42. Bernal, D., Sepulveda, C., & Graham, J. B. (2001). Water-tunnel studies of heat balance in swimming Mako sharks. *Journal of Experimental Biology*, 204(23), 4043-4054.
43. Bernal, D., Sepulveda, C., Mathieu-Costello, O., & Graham, J. B. (2003). Comparative studies of high performance swimming in sharks I. Red muscle morphometrics, vascularization and ultrastructure. *Journal of experimental biology*, 206(16), 2831-2843.
44. Donley, J. M., Shadwick, R. E., Sepulveda, C. A., Konstantinidis, P., & Gemballa, S. (2005). Patterns of red muscle strain/activation and body kinematics during steady swimming in a lamnid shark, the Shortfin Mako (*Isurus oxyrinchus*). *Journal of experimental biology*, 208(12), 2377-2387.
45. Donley, J. M., Shadwick, R. E., Sepulveda, C. A., & Syme, D. A. (2007). Thermal dependence of contractile properties of the aerobic locomotor muscle in the leopard shark and Shortfin Mako shark. *Journal of Experimental Biology*, 210(7), 1194-1203.
46. Bernal, D., Carlson, J. K., Goldman, K. J., & Lowe, C. G. (2012). Energetics, Metabolism, and Endothermy in Sharks and Rays. *Biology of Sharks and Their Relatives*, 13, 211.

47. Maia, A. M., Wilga, C. A., & Lauder, G. V. (2012). Biomechanics of locomotion in sharks, rays, and chimaeras. *Biology of sharks and their relatives, 2nd ed.* Boca Raton, Florida: CRC Press. p, 125-151.
48. Heiser, J. B., Janis, C., & Pough, F. H. (1979). *Vertebrate life*. New.
49. Maia, A., Queiroz, N., Correia, J. P., & Cabral, H. (2006). Food habits of the Shortfin Mako, *Isurus oxyrinchus*, off the southwest coast of Portugal. *Environmental biology of fishes*, 77(2), 157-167.

## CHAPTER SIX

### CONCLUSION

The first objective of this study was to establish a controllable technique to create flow separation by generating different magnitudes of APG over a flat plate through the use of a rotating cylinder. The numerical and experimental studies show that the amount of APG is a function of rotation speed and gap-to-diameter ratio. Both the numerical and experimental studies demonstrated good agreement as to the formation of laminar separation induced by the presence of the cylinder. The studies reveal that, due to the rotation of the cylinder in a direction with flow near the wall, the unsteady wake deflects away from the wall and the boundary layer separation happens only because of the circulation induced by the rotating cylinder. As the cylinder gap to diameter ratio ( $\frac{G}{D}$ ) decreases or the cylinder rotation speed ( $\Omega$ ) increases, the gap flow accelerates and causes earlier and larger separation of the flat plate boundary layer. This system of generating various amounts of APG was proven to be an effective method for inducing both laminar and turbulent boundary layer separation.

This system was then used to investigate the flow separation control potential of shark skin. Shark skin was exposed to various strengths of APGs controlled by the rotating cylinder. Experimental results show that shark skin is capable of controlling both laminar and turbulent separation, in the Reynolds number range tested, by delaying the separation point and reducing the size of separation region. For laminar boundary layer separation, the presence of the shark skin inhibits the backflow and causes unsteadiness in separation. Thus early transition to turbulence reduces the size of the laminar separation bubble. In the case of turbulent boundary layer separation the size of the separated region is also reduced as the shark skin inhibits backflow near the surface and thus prevents the backflow from reaching higher magnitudes.

Due to limitations imposed by water tunnel speeds, Reynolds-number dependency on separation control of shark skin could not be tested. Future work should investigate the flow separation control mechanism for effectiveness of the shark skin at higher Reynolds numbers. Shark skin denticles are very small in size, and the resolution of the DPIV study did not permit the visualization of the scales being actuated by the flow. A significantly magnified view would be necessary to observe the actual motion of the scales by the flow; however, this is difficult to achieve optically and should also be the focus of a future study.

## References

1. Lang, A., Motta, P., Habegger, M. L., Hueter, R., & Afroz, F. (2011). Shark skin separation control mechanisms. *Marine Technology Society Journal*, 45(4), pp. 208-215.
2. Lang, M., Rist, U., Wagner, S., (2004). Investigations on controlled transition development in a laminar separation bubble by means of LDA and PIV, *Experiments in Fluids*, 36, pp. 43–52.
3. Simpson, R. L., Chew, Y. T. & Shivaprasad, B. G., (1981).The structure of a separating turbulent boundary layer. Part 1. Mean flow and Reynolds stresses. *J. Fluid Mech.* 113, pp. 23-51.
4. Simpson, R. L., Chew, Y. T. & Shivaprasad, B. G. (1981).The structure of a separating turbulent boundary layer. Part 2. Higher-order turbulence results. *J. Fluid Mech.* 113, pp. 53-73.
5. Griffin, J., Oyarzun, M., Cattafesta, L.N., Tu, J.H., Rowley, C.W., Mittal, R., (2013). Control of a canonical separated flow, *43rd Fluid Dynamics Conference*.
6. Rampi, R.M., (2012). Design and characterization of a separation system for a flat plate model in a low-speed wind tunnel , undergraduate thesis, university of Florida.